Spatially resolved probing of diffusion and reaction in porous catalyst pellets

Vom Promotionsausschuss
der Technischen Universität Hamburg

zur Erlangung des akademischen Grades

Doktor-Ingenieur (Dr.-Ing.)

genehmigte Dissertation

von

Bahne Sosna

aus

Husum

2020

1. Gutachter: Prof. Dr. rer. nat. Raimund Horn
2. Gutachter: Prof. Dr.-Ing. Michael Schlüter

Tag der mündlichen Prüfung: 27. Oktober 2020

https://doi.org/10.15480/882.3179

Abstract

In the (petro)chemical industry, catalytic fixed-bed reactors packed with porous catalyst pellets are amongst the most widely employed types of reactors. The performance of these reactors in terms of product yield at the reactor outlet is determined by the interplay between diffusion and reaction inside each individual catalyst pellet. For decades, researchers in industry and academia alike have strived to optimize - through analytical and numerical simulation results and integral measurements - pellet size, shape, pore network, and orientation to the flow; and spatial distribution of the active component. To this date, operando measurements of concentration profiles inside porous catalyst pellets were not available. Industrial catalyst pellets are generally non-transparent and thus inaccessible by optical methods; gas spin densities are too low for magnetic resonance imaging, and traditional sampling methods are inadequate when considering the minute diffusional fluxes. In this work, a method was developed to directly measure spatially resolved concentration profiles inside a single catalyst pellet under reaction conditions, by employing a capillary sampling method. CO oxidation on a platinum-coated, porous alumina cylinder was chosen as a test reaction system. CFD simulations were conducted to ascertain the invasiveness of the proposed method; it was hence deemed acceptable for practical applications. Spatially resolved mole fraction profiles of products and educts, inside and in the boundary layer of the particle, are presented for different reaction conditions. Furthermore, phenomena that result from the interplay between diffusion and reaction such as boundary layers, bifurcation, multiple steady states, and kinetic oscillations are shown. Additionally, the possibility of coupling this method with Raman microscopy to gain spatial concentration and temperature profiles from the gas phase was explored. Overall, the developed method could allow the knowledge-based optimization of many industrial fixed-bed processes, without requiring major changes to the process layout.

Kurzfassung

In der (petro)chemischen Industrie gehören katalytische Festbettreaktoren, die mit porösen Katalysatorpellets gefüllt sind, zu den am häufigsten verwendeten Reaktortypen. Die Leistung dieser Reaktoren in Bezug auf die Produktausbeute am Reaktorausgang wird durch das Zusammenspiel von Diffusion und Reaktion in jedem einzelnen Katalysatorpellet im Inneren bestimmt. Forscher aus Industrie und Wissenschaft sind seit Jahrzehnten bestrebt, durch analytische und numerische Simulationsergebnisse sowie integrale Messungen, die Pelletgröße, dessen Form und Orientierung in Bezug auf die Strömung, die Porenvernetzung und räumliche Verteilung der aktiven Komponente zu optimieren. Soweit es bekannt ist, gibt es vor dieser Arbeit keine Operandomessungen von Konzentrationsprofilen in porösen Katalysatorpellets. Industrielle Katalysatorpellets sind im Allgemeinen nicht transparent und daher mit optischen Methoden nicht zugänglich. Die Gas-Spin-Dichten sind für die Magnetresonanztomographie zu niedrig und traditionelle Probenahmeverfahren sind unangemessen, da die winzigen Diffusionsflüsse berücksichtigt werden müssen. In dieser Arbeit wurde eine Methode entwickelt, um räumlich aufgelöste Konzentrationsprofile in einem einzelnen Katalysatorpellet unter Reaktionsbedingungen unter Verwendung einer Kapillarprobenahmemethode direkt zu messen. Als Testreaktionssystem wurde die CO-Oxidation auf einem platinbeschichteten porösen Aluminiumoxidzylinder gewählt. CFD-Simulationen wurden durchgeführt, um die Invasivität der entwickelten Methode zu bestimmen, welche für die praktische Anwendung als akzeptabel angesehen wurde. Ortsaufgelöste Molenbruchprofile von Produkten und Edukten innerhalb und in der Grenzschicht des Partikels werden für verschiedene Reaktionsbedingungen dargestellt. Weiterhin werden Phänomene gezeigt, die sich aus dem Zusammenspiel von Diffusion und Reaktion ergeben, wie Grenzschichten, Bifurkation, mehrfache stationäre Zustände und kinetische Oszillationen. Darüber hinaus wurde die Möglichkeit der Kopplung dieser Methode mit der Raman-Mikroskopie untersucht, um räumliche Konzentrations- und Temperaturprofile aus der Gasphase zu erhalten.

Insgesamt könnte die entwickelte Methode die wissensbasierte Optimierung vieler industrieller Festbettprozesse ermöglichen, ohne dass wesentliche Änderungen am Prozesslayout erforderlich wären.

Acknowledgments

I express my gratitude to

Prof. Dr. Raimund Horn who gave me the opportunity to work in his group as a PhD student, provided the funding for the project, and contributed a lot of his time for guidance, advice, and support in many different forms that allowed me to finish this thesis

Prof. Dr.-Ing. Michael Schlüter for the second opinion of this thesis

Prof. Dr. Andreas Liese for taking the chair of the examination board

Dr. Oliver Korup for the technical and scientific guidance during the making of this work which has proven to be irreplaceable

my current and former research colleagues from the Institute of Chemical Reaction Engineering for good times, many interesting discussions, for proofreading of scripts (including this) and for solving various challenges: Andres Aquino, Birte Wollak, Jan Pottbacker, Ludwig Scharfenberg, Sebastian Sichert, Stephan Bendt, Viktor Berg and Ying Dong

the permanent Institute team: Klaus Mandel for helping with electric and electronic tasks, Christina Laarmann for her lab assistance, Hermine Oppelaar, Eleni Poultoutzidou, and Maike Lerdon for organizational help as well as Prof. Dr. Dr. h. c. Frerich Keil and Dr. Achim Bartsch for their scientific input

the students Lukas Chromow, Navai Mehdiyev and Filip Vrljic who assisted with experiments and simulations

Stefanie Meyer-Storckmann for answering various university related questions with her warm manner.

Dirk Manning and his team for helping with the construction of the set-up

Martin Ritter and Tobias Krekeler for introducing me to the focused ion beam

Camilla Catarci Carteny for proofreading

my parents, family, and friends for their support and motivation

Contents

1 Introduction

Catalysts are fundamental to our modern way of living: about 80% of all products are made with the help of catalysis [1]. Out of all the chemical products - in particular fuels and bulk chemicals – the vast majority is created by heterogeneously catalyzed reactions using solid catalysts [2]. The industry typically employs fixed-bed reactors with random packings of catalyst pellets: their design is simple, the catalyst experiences little mechanical stress, and because fixed-bed reactors have no moving parts running through the reactor shell, they can be operated at high temperatures and pressures. To achieve a maximum surface area of catalyst per unit reactor volume, catalyst pellets in fixed-bed reactors are often porous, ranging in size from a few millimeters to a few centimeters. To minimize pressure drop on one side, and maximize rates of mass and heat transport on the other, a multitude of geometrical shapes for catalyst pellets are in use; such as spheres, cylinders, hollow cylinders, multi-bore cylinders, or multi-lobe extrudates [3]. Porous catalyst pellets are used most efficiently if reactant molecules can reach the active site in the interior of the pellet, and if the desired product molecules can diffuse out of the pellet quickly enough to avoid reacting into undesired side products. How efficiently a porous catalyst pellet is used depends on i) the dimensions of the pellet, ii) the pore size distribution and connectivity, iii) the diffusive properties of the molecules undergoing reaction, iv) the rate of the catalytic reaction, and v) the boundary conditions at the pellet surface - such as temperature, concentration, and velocity field. In random catalyst packings, every single pellet is exposed to different boundary conditions, because of the different orientation in the flow as well as concentration and temperature gradients present in the catalyst bed. If the spatial concentration profiles inside a porous catalyst pellet could be measured, the geometric dimensions of the pellet, its pore network, the spatial distribution of the active component, and the orientation of the pellet with respect to the local flow in the reactor could be optimized, based on the acquired knowledge. Many catalytic

fixed-bed processes would benefit from such a knowledge-based optimization since major changes to the process layout would not be required.

To this day, concentration profiles in porous catalyst pellets are almost exclusively obtained by simulation. Before the widespread application of computers in reaction engineering, the problem of diffusion and reaction in porous catalyst pellets was tackled analytically. Landmark papers and books were published by Jüttner [4], Zeldovich [5], Damköhler [6], Thiele [7], Frank-Kamenetzki [8], Amundson [9,10] and Aris [11] to name a few. The stability and the dynamic behavior of porous catalyst pellets were investigated and reviewed by Aris [12] and Luss [13] among others. To allow for analytical solutions, in these studies, the investigated reaction systems were mainly restricted to rather simple reaction networks, essentially first-order reactions in isothermal and non-isothermal pellets. Moreover, the pore network had to be treated as a continuum. With the advent of computers and the implementation of numerical solution algorithms, more complex catalytic reaction schemes could be analyzed, and the pore structure of the pellet could be implemented in the model: an account of this process was made by Keil [14]. In recent years, the modeling of catalytic fixed-bed reactors by particle-resolved CFD simulations gained popularity [15,16]. This type of methodology allows, among many other applications, to study how the orientation and the position of the porous catalyst pellet in the reactor influences the processes inside the pellet. For example, Dixon et al. [17] studied the effect of the inclination angle of a single hollow cylinder on methanol synthesis, whilst Wehinger et al. [18] focused on the pore processes for CO oxidation in a single sphere with a 100 μm washcoat. Furthermore, computationally high-demanding simulations of randomly packed beds of arbitrarily-shaped particles have now become possible [19]. Furthermore, intra-pellet diffusion coupled with (simplified) micro kinetics inside the pellets accounting for elementary reaction steps is starting to be implemented in these simulations [20–23].

In comparison to the high degree of sophistication that has been reached in modeling the diffusion-reaction interplay in porous catalysts, there are few experimental data to validate such simulations. The development of high-resolution spatial reactor profiling techniques by Horn et al. [24] and Partridge et al. [25,26] allows measuring concentration profiles under operando conditions inside reactors. Both methods use a sampling capillary that can be moved through the reactor parallel to the reaction coordinate and analyze the samples taken with a mass spectrometer. Horn's method also allows the measurement of the gas phase temperature with a thermocouple, of

the catalyst temperature with a pyrometer [27], and measurement of Raman spectra of the catalyst surface at the spot of the sampling [28]. These helped to understand chemical reactors on a more fundamental level since usually only inlet and outlet conditions of the reactor are known. For single particles, Küster et al. [29] developed a reactor to investigate single-particle gasification in which Raman spectroscopy provided information about gas phase temperature and concentrations around the particle. With the single pellet reactor from Hegedus et al. [30], measurements of an averaged concentration in a (pseudo) center plane of catalyst pellets were successfully demonstrated. Nonetheless, this reactor is far from operando conditions, since diffusion through the circular planes is not possible, orientation to the flow cannot be changed, and only limited shapes can be investigated. Overall, none of the experimental methods reported above provide information about concentrations inside a catalyst particle. Recently, Chmelik et al. [31] measured concentration profiles inside platinum-coated glass beads during benzene hydrogenation by IR-microimaging. While this method is very elegant and provides true intra-particle profiles, it is restricted to optically-accessible carriers – such as glass – and rather small particles, in the order of a few hundred micrometers. Industrial catalyst pellets are generally non-transparent, and one to two orders of magnitude larger, making this method not suitable for catalysts in industrial applications

This work aims to develop a method that allows the measurement of spatially resolved concentration profiles inside and in the boundary layer of industrially relevant catalyst particles. The herein developed method is based on the spatial sampling technique developed by Horn et al. [24]. In contrast to the previous method, the sampling volume needs to be drastically decreased to not disturb the sensitive processes inside the catalyst pellet. Therefore, a sampling capillary with an inner diameter of 10 μm or less is introduced. CFD simulations are used to investigate the invasiveness of the method. CO oxidation on platinum-coated, porous alumina cylinders has been chosen as a model reaction system for the following reasons: no side reactions, the stability of catalysts towards the oxidation reaction, easy preparation of the catalyst by impregnation, and the vast amount of information available in literature for a wide range of conditions [32]. Reaction kinetics were implemented using a literature kinetic model for CO oxidation on platinum [33].

The measurements presented in this work demonstrate the practical applicability of the developed method. An array of typical diffusion-induced phenomena, such as concentration profiles in and around a porous catalyst pellet, mass and heat

transport limitations, bifurcation, multiple steady states, and even catalytic oscillations can be observed. Furthermore, the feasibility of coupling Raman microscopy with the newly developed set-up, to measure spatial temperature and concentration profiles around the catalyst particle, is demonstrated.

2 Theoretical background

In this chapter, the theoretical chemical background for reactions on a single catalyst pellet as well as the physical background of the analysis methods are explained. Chapter 2.1 provides a general introduction about heterogeneous catalysis and then goes into detail about external mass and heat transfer limitations (2.1.1) and multiplicities (2.1.2) in catalyst pellets. Furthermore, a short summary of the CO oxidation is given (2.1.4); the latter was selected as a model reaction throughout this study. Chapter 2.2 explains the equations for the CFD simulations afterward used to demonstrate the invasiveness of the method developed in this work. Chapter 2.3 introduces the working principle of the instrument employed to drill the side orifice in the quartz sampling capillary: the focused ion beam. Moreover, Chapter 2.4 describes the physical background of mass spectrometry, fundamental for the analysis of the samples taken inside the catalyst pellets. The possibility of measuring concentration and temperature profiles with Raman spectroscopy in the gas phase around the particle has been investigated; the theory and calculation methods are given in Chapter 2.5.

2.1 Heterogeneous catalysis

Educts in chemical reactions are not in their thermodynamically preferred state: an energy barrier is preventing their transformation. Here catalysts come into the game, allowing the creation of a product through a more favorable reaction path (i. e. by lowering the energy barrier). Thus increasing the rate of reaction and making reactions possible at reachable temperatures without affecting the overall equilibrium. A very common example of the effect of catalysts upon a reaction (or lack thereof) is gaseous H_2 and O_2: both are virtually inert at room temperature, but, when platinum is introduced, they rapidly react to H_2O.

A heterogeneously-catalyzed reaction involves more than one phase; reactants are usually in the gas or liquid phase and the catalyst is a solid. Inorganic solids such as metals, oxides, sulfides, and metal salts are common heterogeneous catalysts, but they may also be organic materials such as organic hydroperoxides, ion exchangers, and enzymes. A variety of catalyst families exist, the most important related to this work are bulk (unsupported), supported, and coated catalyst [34]. Bulk catalysts contain only the catalytic active component: examples are Raney-Nickel catalysts in hydrogenation reactions [34] or platinum gauzes in ammonia oxidation [35]. In supported catalysts, the dispersion of active material is stabilized by a material that provides high surface areas. These support materials may or may not actively interfere with the catalytic process. They are often porous materials with a high thermostability such as alumina, silica, or magnesia. For example, silver supported on alumina is used for the epoxidation of ethylene [34]. Coated catalysts contain a catalytically active layer, which can be a bulk or a supported catalyst, applied on an inert structured surface [34].

In general, a heterogeneously catalyzed reaction can be broken down into seven steps [36]:

1. Mass transfer from the bulk fluid to the external surface of the catalyst pellet
2. Diffusion of the reactant(s) through the catalyst pores
3. Adsorption of the reactant(s) onto the catalyst surface
4. Reaction on the surface of the catalyst
5. Desorption of the product(s)
6. Diffusion of the product(s) through the catalyst pores to the external surface
7. Mass transfer from the external surface of the catalyst pellet to the bulk fluid

The rate of the slowest of these steps determines the overall reaction rate. If the reaction steps (3, 4, and 5) are consistently faster than the diffusion processes, the educts will react on the surface of the catalyst, without penetrating its pores which results in poor catalyst efficiency. In the opposite case, where the diffusional steps (1, 2, 7, and 8) are faster, reactant concentrations in the catalyst and in the bulk will be equal, and thus, diffusion will not affect the rate [36].

Steps 3, 4, and 5 occur on the active sites of the catalyst, which Fogler [36] describes as "*a point on the catalyst surface that can form strong chemical bonds with an adsorbed atom or molecule*". Various electron transfer steps are involved in the formation of these complex bonds, forming an unstable intermediate compound between the

surface of the catalyst and at least one of the reactants. This intermediate must be labile enough to decompose to yield the final product(s) and stable enough to be formed in sufficient quantities. Furthermore, the geometrical surface structure of the metal is important, it can contain terraces, edges, kinks, and vacancies with sites having different coordination numbers [1]. Surface defects potentially increase the adsorption of intermediates, as shown for the methanol synthesis on a CuZnO catalyst [37]. When surface structures change periodically during the reaction, kinetic oscillations might occur: an example is CO oxidation [38,39].

The external diffusion processes (1 and 7), often referred to as film diffusion, can be influenced by the flow conditions around the catalyst. High velocities in the proximity of the catalyst (through the reactor) and small particle diameters will increase the mass transport. This phenomenon can be accompanied by an unwanted pressure drop inside the reactor, which can be minimized by aptly selecting catalyst shape. For example, hollow cylinders and multi-bore cylinders are common shapes employed to decrease the pressure drop**.** These rather complicated shapes have an intricate flow pattern around them, which changes with the inclination angle to the flow, and, in turn, influences the external mass transport [17].

The internal diffusion (2 and 6) is controlled by the pore structure of the catalyst. High internal surface areas are desired since the reaction rate is proportional to the number of active sites present in the pores when the process is reaction rate-limited. These can be achieved with micropores (< 2 nm): in these pores, Knudsen diffusion prevails, slowing down the internal mass transport. In this case, the mean free path of the molecule is greater than the diameter of the catalyst pore. Therefore, the molecules collide more often with the pore wall than with each other [36]. Since the active sites are spread all over the pore walls, educts might completely react before they reach the inside of the catalyst; on the other hand, in macropores (> 50 nm) the transport will be faster, but the surface area is limited. A bimodal pore distribution, allowing for both high diffusional fluxes through macro-sized transport pores, and reaction in micro-sized reaction pores accounting for high specific surface areas, was proven to be advantageous [40]. Nonetheless, not only size but also pore shape and pore connectivity have major influences on the diffusion processes [29].

Even though a catalyst theoretically is not consumed during the reaction, the activity decreases after time. The etiology of this deactivation of the active sites can be divided into three categories: sintering or aging, fouling or coking, and poisoning.

Sintering commonly happens after a catalyst is exposed to high gas phase temperatures for a prolonged time. The active sites on the surface agglomerate, and therefore lose surface area, or block pores, making them not accessible anymore; additionally, sintering of the support could also block the pores. Coking commonly happens with reactions involving hydrocarbons. A carbonaceous (coke) species gets deposited on the surface and blocks the active sites. Finally, a catalyst gets poisoned when molecules become irreversibly chemisorbed to active sites and thus blocking them [36].

To improve the performance of industrial catalysts often modifiers (promoters) are added [1]. They can simply increase the reaction rate per site by changing the binding energy (electronic promoter) or by stabilizing more active sites on the support (structural promoter). In reactions yielding more than one product in parallel or consecutive reactions, they can increase the activity by poisoning unwanted reactions. In exothermic reactions, they can act as a catalyst poison to avoid high temperature increases, especially hot spots (high local temperature gradients), undesirable products (e.g. CO_2 and CO in selective catalytic oxidation), or sintering and aging [1].

2.1.1 External heat and mass transport

The flow velocity in the vicinity of the pellet will vary according to the exact considered position. A hydrodynamic boundary layer builds up around the particle. It is usually defined as the distance from a solid object to where the fluid velocity is 99% of the bulk velocity u_0. The mass transfer boundary layer δ can be defined similarly: it is the distance from a solid object to where diffusing species reaches 99% of the bulk concentration $c_{i,B}$ [36]. A representation of the reactant i can be found in Figure 2-1.

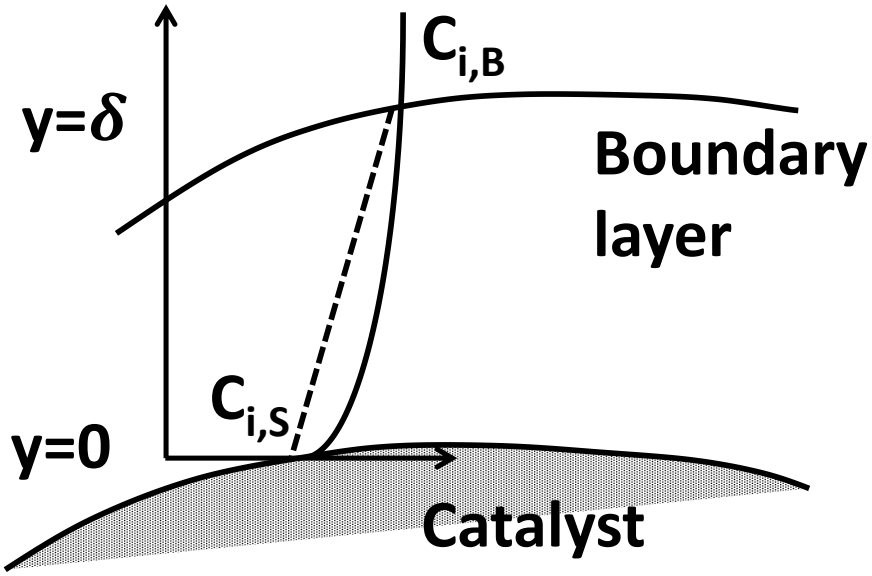

Figure 2-1: Boundary layer around the surface of a catalyst pellet, adapted from [36].

The flux between the surface s and the bulk can be calculated as:

$$N = \frac{D_{i,m}}{\delta}\ \left(c_{i,B} - c_{i,s}\right) = k_c\left(c_{i,B} - c_{i,s}\right) \qquad (2.1)$$

where $c_{i,s}$ is the surface concentration of component i. The ratio of the diffusivity of species i in a mixture m $D_{i,m}$ and δ is defined as the mass transfer coefficient k_c. δ is usually not directly accessible; therefore, for forced convection, the mass transfer is correlated to the Sherwood number (Sh), the Reynolds (Re) number, and the Schmidt number (Sc), to calculate k_c [36].

$$Sh = \frac{k_c d}{D_{i,m}}, \qquad (2.2)$$

$$Sc = \frac{\eta}{\rho_f D_m}, \qquad (2.3)$$

$$Re = \frac{u_0 d \rho_f}{\eta}, \qquad (2.4)$$

where d is the characteristic length of the pellet, ρ_f the fluid density, and η the dynamic viscosity. Sh is based on experimentally-determined correlations: a wide variety of them exists in literature. A summary can be found in [42]. For cylinders in laminar flow, Sh can be calculated as [43]:

$$Sh = 0.664 \sqrt{Re} \sqrt[3]{Sc} \quad (2.5)$$

By combining Equation 2.2 and 2.5, the following relation for k_c results:

$$k_c = 0.664 \frac{D_m^{\frac{2}{3}} u_0^{\frac{1}{2}}}{v^{\frac{1}{6}} d^{\frac{1}{6}}}, \quad (2.6)$$

Where v is the kinematic viscosity. Consequently, it becomes obvious that the boundary layer around the particle can be decreased by higher velocities and/or smaller particles.

For similar geometries, heat and mass transfer are analogous. The heat flux q through the boundary layer can be calculated as follows:

$$q = h\ (T_B - T_s), \quad (2.7)$$

where T_B is the bulk temperature, T_s the surface temperature, and h the heat transfer coefficient. Sh is then replaced by the Nußelt number Nu, and Sc by the Prandtl number Pr [36].

$$Nu = \frac{h\, d}{\lambda_f}, \quad (2.8)$$

$$Pr = \frac{\eta c_p}{\lambda_f}, \quad (2.9)$$

where c_p is the heat capacity at constant pressure, and λ_f the thermal conductivity of the fluid.

2.1.2 Internal heat and mass transport

The reactants are diffusing from the surface into the pores within the pellet, therefore the reactant concentrations will decrease from the surface to the center of the pellet. The pores inside the pellet are a series of tortuous interconnecting paths of pore bodies and pore throats with varying cross-sectional areas [36]. Hence, various transport mechanisms can occur inside the pores. When a pressure difference between the surface and the center of the pellet is present, this results in a convective flux. Furthermore, molecular or Knudsen diffusion can be present. For molecular diffusion, molecule-molecule collisions are dominating over molecule-wall collisions, whilst for Knudsen diffusion, the opposite is true [44]. In this latter case, the mean free path λ of the molecule needs to be much longer than the characteristic length of the pore l; which in turn means that the Knudsen number needs to be much higher than one [45]:

$$Kn = \frac{\lambda}{l} \gg 1, \tag{2.10}$$

Moreover, the molecules can move laterally on the adsorbed pore surface, which is called surface diffusion. All of these four transport mechanisms can occur simultaneously and can be combined, analogously to a resistance in an electric circuit. The fluxes of molecular and Knudsen diffusion behave like a serial circuit; in turn, this combined flux behaves like a parallel circuit to the surface diffusion and the convective flux [44]. A different type of transport mechanism is configural diffusion. The latter occurs in pores having approximately the same diameter as the molecules - e.g. those found in zeolites - where only one molecule after another can pass through [44].

Molecular diffusion is based on binary diffusion coefficients D_{ij}. For an ideal gas, D_{ij} can be determined according to the Chapman-Enskog theory [46]:

$$D_{ij} = \frac{1.86 \cdot 10^{-3}\, T^{3/2} \sqrt{\frac{1}{M_i} + \frac{1}{M_j}}}{P\, \sigma_{ij}^2\, \Omega^*} \qquad \left[\frac{cm^2}{s}\right] \tag{2.11}$$

where P is pressure in atm and M the molar mass in g mol^{-1}; the mean collision diameter σ_{ij}, expressed in Å can be calculated from the collision diameter of each species which are listed in literature [47]:

$$\sigma_{ij} = \frac{\sigma_i + \sigma_j}{2} \tag{2.12}$$

Values for the solution of the collision integral Ω^* are listed in literature [47]. The diffusion coefficient for Knudsen diffusion $D_{i,K}$ can be calculated as [48]:

$$D_{i,K} = \frac{2}{3} r_P \sqrt{\frac{8\,R\,T}{\pi M_i}} \tag{2.13}$$

where r_P is the mean pore radius, and R the universal gas constant. Furthermore, the pore size distribution, shape, and connectivity will influence the transport processes. Since a description of every pathway is very complex, different pore structure models have been developed, describing the average diffusion taking place at any position r in the pellet. In most of these models, an effective diffusion coefficient D_{eff} is introduced: this is a function of the permeability φ, which in turn is the ratio of the porosity ϵ and tortuosity τ (Equation 2.14).

$$D_{ij,eff} = D_{ij}\frac{\epsilon}{\tau}\,, D_{i,K,eff} = D_{i,K}\frac{\epsilon}{\tau} \tag{2.14}$$

The porosity ϵ is the ratio between the volume of void space and the total volume of the pellet, whereas the tortuosity τ is the ratio of the actual distance a molecule travels between two points and the shortest distance between those two points [36]. For τ different models have been developed - a summary can be found in [49]; typical values for industrial catalysts are in the range between three and six. Moreover, it is possible to determine this value with a Wicke-Kallenbach cell, mercury porosimetry [44], or BET measurements [50].

Common approaches to describe the fluxes inside catalyst pellets are the Wilke model, and the rigorous Stefan-Maxwell model, both of which only consider bulk diffusion; or the dusty gas model, which accounts for combined bulk and Knudsen fluxes; and finally, the Wilke-Bosanquet model, which is a simplification thereof. The Wilke-Bosanquet model is described in detail in Chapter 2.2, for the other models the reader is referred to [51]. They all can describe multicomponent diffusion.

The diffusion processes are slowing down the overall rate of the reaction. Therefore, an effectiveness factor η is introduced, which is defined as the ratio of the actual overall rate with diffusion limitations inside a catalyst, and the reaction rate for the

conditions at the outer surface of the catalyst (which do not include any internal diffusion resistances) [36]:

$$\eta = \frac{\int_0^{V_P} R(c_i, T) dV_P}{R\left(c_{i,s}, T_s\right) V_P} \tag{2.15}$$

where R is the reaction rate, and V_P the particle volume. Furthermore, it is possible to define an overall effectiveness factor η_B, which includes also external limitations and is defined as the ratio of the actual overall rate inside a catalyst and the reaction rate for bulk conditions:

$$\eta_B = \frac{\int_0^{V_P} R(c_i, T) dV_P}{R\left(c_{i,B}, T_B\right) V_P} \tag{2.16}$$

To describe the ratio of reaction rate and diffusion limitation, Thiele [7] introduced a dimensionless number, the Thiele modulus ϕ, which is defined as follows:

$$\phi = L \sqrt{\frac{k\, c^{n-1}}{D_{eff}}}, \tag{2.17}$$

where L is the characteristic length of the pellet, and k the reaction rate constant and n the reaction order. The Thiele modulus ϕ is small for slow reactions with minor diffusion limitations, resulting in a large effectiveness factor, and educt concentrations close to surface conditions throughout the whole particle. For large ϕ, diffusion is limiting, the effectiveness factor becomes small, and the educt concentration decreases to zero close to the surface of the particle. In Figure 2-2 this is shown for a first-order reaction in an isothermal spherical pellet. Similar to the external transport limitations, the internal diffusion limitations can be reduced by using smaller particles; this, in turn, will lead to a higher pressure drop in the reactor [44].

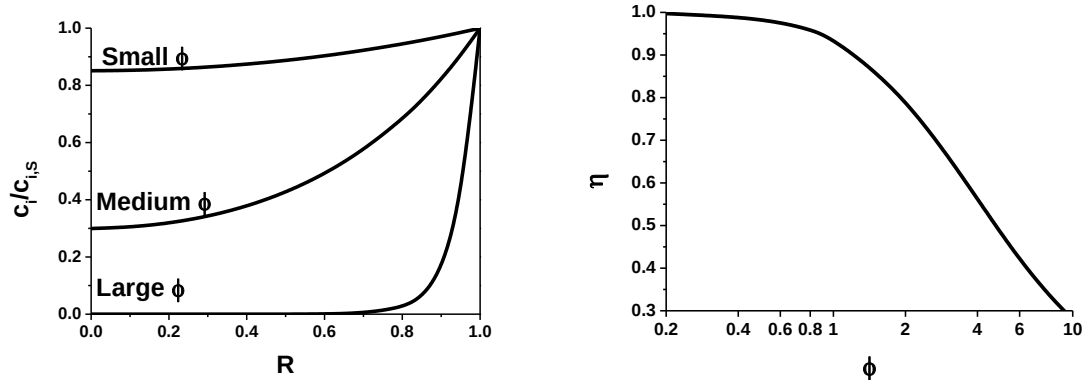

Figure 2-2: Concentration profile in a spherical pellet ($R = r/r_P$) for different Thiele moduli (left hand side). Effectiveness factor plot for a first-order reaction in an isothermal spherical pellet (right-hand side).

The heat transport inside catalyst pellets is described by the effective thermal conductivity λ_{eff}. It accounts for the heat transport through the solid structure (support, and active component) and the fluid phase in the pores. Different models have been developed to calculate λ_{eff} out of the pore structure, and thermal conductivity of the gas and the support material (e.g. [52], [53]), but also direct measurements of λ_{eff} are possible [54,55].

By combining mass and heat transport, the maximal temperature difference $(\Delta T_s)_{max}$ that could exist in a particle of any geometry under steady-state conditions, relative to the surface temperature T_s, can be calculated with the Prater number β (a derivation thereof can be found in [45]):

$$\beta = \frac{(\Delta T_s)_{max}}{T_s} = \frac{\mathrm{D}_{eff} c_{i,s}(-\Delta_R H)}{T_s\, \lambda_{eff}}, \tag{2.18}$$

where $\Delta_R H$ is the heat of reaction. For most industrial processes β is very small, and therefore the catalyst particles employed in such processes can be assumed as isothermal [45]. On the contrary, external temperature gradients are way more likely to subsist. To calculate the maximal temperature difference $(\Delta T_B)_{max}$ between the catalyst pellet and the bulk temperature, a Prater number β_B is defined, which includes external heat and mass transfer limitations [56]:

$$\beta_B = \frac{(\Delta T_B)_{max}}{T_B} = \frac{k_c c_{i,B}(-\Delta_R H)}{h\, T_B} \tag{2.19}$$

2.1.3 Multiplicity of steady states in catalyst particles

Combined effects of internal and external mass and heat transfer, adsorption, as well as the reaction itself can result in multiple steady state profiles inside a catalyst particle. Figure 2-3 shows a typical effectiveness diagram with multiple steady states (marked between the two lines) where the overall effectiveness factor η_B (Equation 2.16) is plotted against the Thiele modulus ϕ. It can be seen from the diagram that, for multiplicities, η_B must be greater than one. This is possible either for reactions where the reaction rate is increasing with increasing conversion or for exothermic reactions with external and/or internal mass and heat transfer limitations. For these conditions, different criteria have been theoretically developed by previous authors.

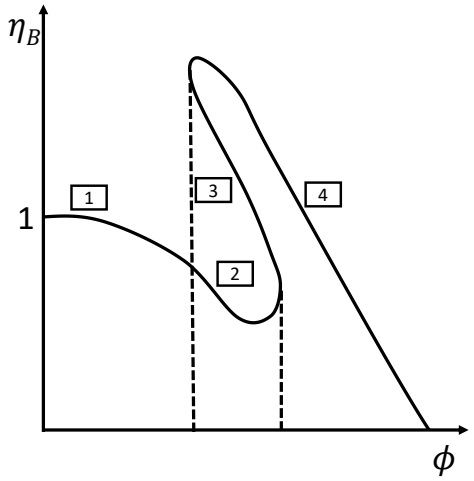

Figure 2-3: Effectiveness factor diagram showing the main controlling regions: (1) kinetic control, (2) diffusion control, (3) unstable steady states, (4) external mass transfer control; adapted from [57].

For an adiabatic particle, Luss [58] derived a criterion for a first-order reaction to estimate for which conditions multiple steady states are possible:

$$4(1+\beta) < \beta\gamma, \tag{2.20}$$

The Arrhenius number γ can be calculated as:

$$\gamma = \frac{E_A}{RT}, \tag{2.21}$$

where E_A is the activation energy. The aforementioned conditions verifying the Luss criterion are rarely occurring since high temperature gradients inside the particle are needed, whilst particles are in most cases nearly isothermal [45,57,59].

Isothermal particles can have multiple steady states when the following criterion is fulfilled [58]:

$$\left(c_i - c_{i,s}\right)\frac{d\ ln\ f(c_i)}{dc_i} > 1, \tag{2.22}$$

where $f(c_i)$ is the rate equation, and c_i the concentration inside the catalyst. The criterion furthermore requires [45]:

$$n < (n-1)\frac{c_i}{c_{i,s}}, \tag{2.23}$$

where n is the reaction order. Consequently, only reactions with a negative reaction order, i.e. where the reaction rate increases with conversion, can lead to multiplicities for certain values of $c_i/c_{i,s}$.

For exothermic reactions, where external heat transport is prevalent, multiplicities are even possible for isothermal particles with a positive reaction order. The criterion for an effectiveness factor $\eta = 1$, when no intraparticle gradients are prevalent, is [56]:

$$(\beta_B\gamma - (1-n)(1+\beta_B))^2 > 4\beta_B\gamma(1+\beta_B) \text{ for } n \geq 1 \tag{2.24}$$

For all other reactions orders it is [56]:

$$(\beta_B\gamma + 1 - n)^2 > 4\beta_B\gamma(1+\beta_B) \text{ for } n \leq 1 \tag{2.25}$$

For intraparticle gradients where $\eta \neq 1$, the regime for possible multiplicities becomes narrower, as can be seen in Table 2-1, Equation 2.26, and 2.27.

Table 2-1: Summary of uniqueness criteria for the three different phenomena causing multiplicity

Phenomenon	Criterion for possible multiplicities	Reference	Eq.
Adiabatic particle	$4(1+\beta) < \beta\gamma$	[58]	2.20
Isothermal particle	$(c_i - c_{i,s})\frac{dlnf(c_i)}{dc_i} > 1$	[45,58]	2.22
Boundary layer $n \geq 1, \eta = 1$	$(\beta_B\gamma - (1-n)(1+\beta_B))^2 > 4\beta_B\gamma(1+\beta_B)$	[56]	2.24
Boundary layer $n \leq 1, \eta = 1$	$(\beta_B\gamma + 1 - n)^2 > 4\beta_B\gamma(1+\beta_B)$	[56]	2.25
Boundary layer $n \geq 1, \eta \neq 1$	$(\beta_B\gamma - (1-n)(1+\beta_B))^2 > 8\beta_B\gamma(1+\beta_B)$	[56]	2.26
Boundary layer $n \leq 1, \eta \neq 1$	$(\beta_B\gamma + 1 - n)^2 > 8\beta_B\gamma(1+\beta_B)$	[56]	2.27

2.1.4 CO Oxidation

The catalytic oxidation of carbon monoxide is industrially relevant for automotive emission control, and the CO removal from large gas streams of the petrochemical industry. In research, it is considered as a model reaction for understanding fundamental concepts in heterogeneous catalysis [60].

$$CO + \frac{1}{2}O_2 \rightarrow CO_2 \qquad \Delta_R H^0 = -283\ kJ\ mol^{-1} \tag{2.28}$$

The reaction can be catalyzed by various metals. Commonly, noble metals are used: for example, automotive exhaust catalysts contain Pt, Pd, and/or Rh, which are supported on monoliths; Ir could be also employed [61]. These noble metals require temperatures above 100 °C; but some catalysts are active at lower temperatures, e.g. gold nanoparticles, Pt supported on tin(IV)oxide, or copper oxides [62]. Furthermore, tricobalt tetraoxide nanorods were found to be able to convert CO at temperatures as low as -77 °C [63].

Among all mentioned catalysts, CO oxidation on platinum is one of the most investigated reactions in literature. It can be divided into the following elementary steps [64]:

$$O_2 + (Pt) \underset{k_1^-}{\overset{k_1^+}{\rightleftharpoons}} O_2(Pt), \tag{2.29}$$

$$O_2(Pt) + (Pt) \underset{k_2^-}{\overset{k_2^+}{\rightleftharpoons}} O(Pt) + O(Pt), \tag{2.30}$$

$$CO + (Pt) \underset{k_3^-}{\overset{k_3^+}{\rightleftharpoons}} CO(Pt), \tag{2.31}$$

$$CO(Pt) + O_2(Pt) \underset{k_4^-}{\overset{k_4^+}{\rightleftharpoons}} CO_2(Pt) + O(Pt), \tag{2.32}$$

$$CO(Pt) + O(Pt) \underset{k_5^-}{\overset{k_5^+}{\rightleftharpoons}} CO_2(Pt) + (Pt), \tag{2.33}$$

$$CO_2(Pt) \underset{k_6^-}{\overset{k_6^+}{\rightleftharpoons}} CO_2 + (Pt), \tag{2.34}$$

where k_i^+ and k_i^- are the rate constants of the forward and the reverse reaction, respectively. Allian et al. [65] developed a Langmuir-Hinshelwood-Hougon-Watson (LHHW) mechanism by assuming Equation 2.32 as the rate-determining step, the adsorption of CO and O_2 as quasi-equilibrated (2.29, 2.31), Equation 2.33 and 2.34 are considered to be irreversible, and neglecting Equation 2.30 altogether; which results in the following expression for the overall reaction rate:

$$r = \frac{k_4^+ K_3 K_1 p_{CO} p_{O_2}}{\left(1 + K_3 p_{CO} + K_1 p_{O_2}\right)^2}, \tag{2.35}$$

where p_{CO} and p_{O_2} are the partial pressures of CO and O2, respectively, and K_i is the equilibrium constant defined as the ratio of k_i^+ and k_i^- .

The CO oxidation over Pt occurs in a high- and a low-active regime. At low temperatures, i.e. the low active regime, K_3 becomes high, hence, the surface is predominantly covered with CO, and the reaction rate is proportional to p_{O_2}/p_{CO}. The common assumption of quasi-equilibrated molecular and dissociative adsorption of O_2 and subsequent reaction of $O(Pt)$ with $CO(Pt)$, would result in CO oxidation rates proportional to ${p_{O_2}}^{0.5}/p_{CO}$ in the low-active regime [65]. However, this is not in accordance with many experimental works in literature, since fitted LHHW mechanisms often have the form of Equation 2.35 (e.g. [32,33,65–67]).

The high-active regime occurs at higher temperatures. In literature, the surface at these conditions is intensively discussed. There is general agreement among researchers that the surface is nearly free of CO. However, it is not clear if either metallic platinum [68,69], chemisorbed oxygen [70], or a partially oxidized platinum surface [71] causes the high activity of the catalyst. In this regime, often strong external and/or internal diffusion limitations are observed [32]. These have not always been excluded in kinetic measurements, which might explain the wide range of activation energies for CO oxidation on Pt found in literature [32], ranging from 30 kJ mol^{-1} [72] to 120 kJ mol^{-1} [73].

Inside catalyst pellets, high- and low-active regimes can exist for the same external condition, resulting in two different steady state concentration profiles. This occurs when the diffusion resistance leads to significant concentration gradients inside the pellet. The shift from one to the other regime happens suddenly, by small changes in the boundary conditions (e.g. temperature, CO/O_2 ratio, velocity). It will be accompanied by a significant temperature change of the catalyst in adiabatic systems. However, the opposite shift happens at different conditions, which lead to a hysteresis [67,74].

The observation of kinetic oscillations in critical runaway episodes of CO removal reactors opened the evolution of the whole research field of nonlinear dynamics in surface science [60]. Oscillations for CO oxidation on Pt have been observed on clean Pt structures under ultra-high-vacuum (UHV) conditions [75,76], but also on monoliths [26], single catalyst particles [74,77], Pt nanoparticles [78], Pt gauzes [74], and in macroscopic flow reactors [39,79] under atmospheric pressure. They can be

explained by structural dynamic responses, ranging from surface reconstructions to subsurface state populations [60]. These mechanisms are quite specific, depending on the reaction conditions and the active component of the catalyst.

2.2 Fundamental CFD equations

For modeling a heterogeneous catalytic reactor, governing equations for conservation of mass and momentum (Navier-Stokes equations), conservation of each species, and conservation of energy need to be implemented. All simulations in this work were carried out assuming laminar flow and steady state. Therefore, no turbulence models and time dependent equations are required. The conservation of mass can be expressed as [80]:

$$\nabla \cdot (u\rho) = 0, \tag{2.36}$$

where ρ is the mixture averaged density, and u the velocity vector. Conservation of momentum means the following holds[80]:

$$\rho(u \cdot \nabla)u + \nabla \cdot p + \nabla \cdot \tau = 0 \tag{2.37}$$

The viscous stress tensor τ can be calculated as:

$$\tau = -\mu(\nabla u + (\nabla u)^T) + \frac{2}{3}\mu(\nabla \cdot u)I \tag{2.38}$$

where μ is the dynamic viscosity of the mixture and I is the identity matrix. Conservation of species i is defined as [81]:

$$\rho(u \cdot \nabla)w_i + \nabla \cdot j_i - \sum_j \nu_{i,j} R_j M_i = 0 \quad i = 1, \dots, N_g, j = 1, \dots, N_R \tag{2.39}$$

Where $\nu_{i,j}$ is the stoichiometric coefficient of the species i in the reaction j, w_i is the mass fraction, R_j is the net production rate, and M_i is the molar mass. The diffusion mass flux j_i, with respect to the mass average velocity, is calculated as [82]:

$$j_i = -\left(D_{i,m}\rho\nabla w_i + D_{i,m}\rho w_i \frac{\nabla M_n}{M_n}\right) \tag{2.40}$$

where the mean molar mass M_n is

$$M_n = \left(\sum_i \frac{w_i}{M_i} \right)^{-1}, \tag{2.41}$$

and the mixture averaged diffusion coefficient $D_{i,m}$ is defined as follows [51]:

$$D_{i,m} = \frac{1 - w_i}{M_n \sum_{\substack{i=1 \\ j \neq i}}^{N_g} \frac{w_j}{M_j D_{ij}}}, \tag{2.42}$$

where D_{ij} is calculated according to Equation 2.11. In this study, the Wilke-Bosanquet model is applied which combines molecular and Knudsen diffusion to a diffusion coefficient $D_{i,M}$. To describe the diffusion inside the pellet accurately, the pore geometry and connectivity need to be accounted for. Therefore, an effective diffusion coefficient $D_{i,eff}$ is introduced, that accounts for all these parameters [51]:

$$D_{i,eff} = \frac{1}{\left({D_{i,m}}^{-1} + {D_{i,K}}^{-1} \right)} \frac{\epsilon}{\tau} = D_{i,M} \frac{\epsilon}{\tau} \tag{2.43}$$

$D_{i,K}$ is calculated according to Equation 2.13. Conservation of energy is calculated as follows [80]:

$$\rho C_p u \cdot \nabla T - \nabla \cdot (\lambda \nabla T) - \sum_j \left(-\Delta H_{r,j} \right) R_j = 0, \tag{2.44}$$

where C_p is the mixture averaged heat capacity at constant pressure and λ is the mixture averaged thermal conductivity. For the catalyst particle, C_p and λ are catalyst properties. Furthermore, the ideal gas law needs to be included:

$$p = \frac{\rho R T}{M_n} \tag{2.45}$$

2.3 Focused ion beam

The focused ion beam (FIB) system can be used to understand and manipulate structures at the nanoscale. It is used for four basic functions: milling, deposition, implantation, and imaging, because greater mass ions are interacting with the

surface [83]. A schematic diagram with all major components of the apparatus is shown in Figure 2-4.

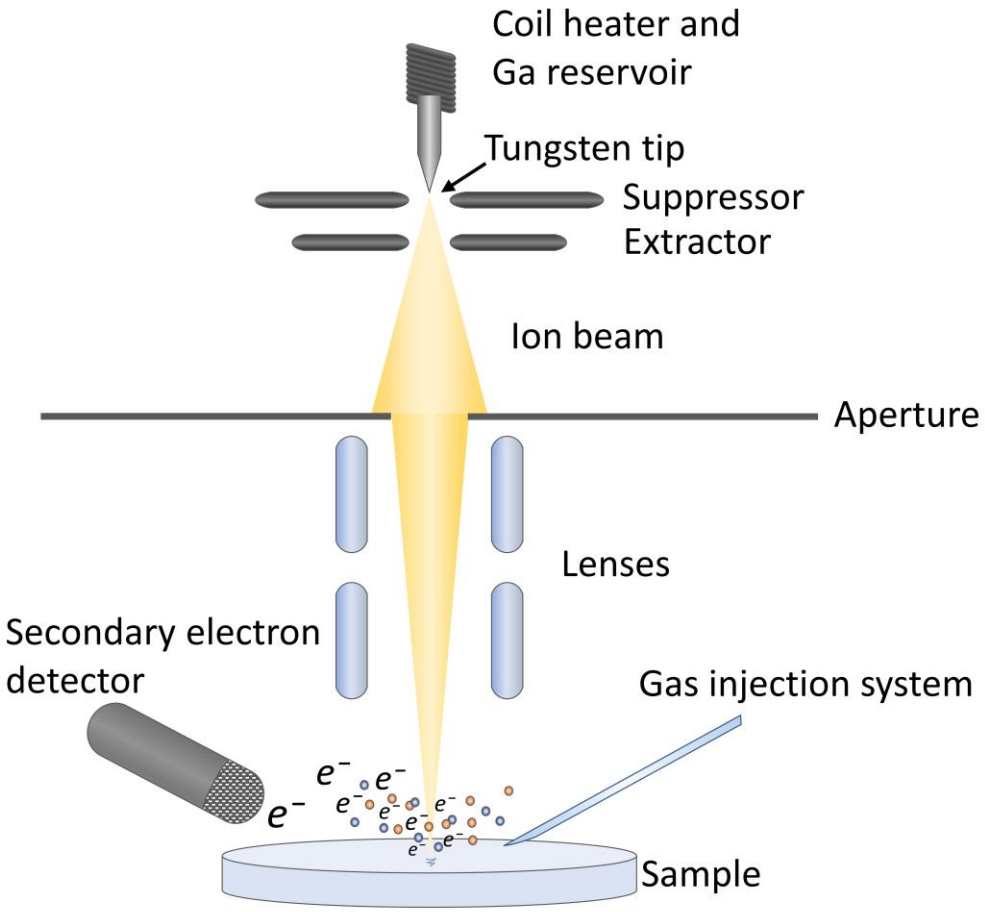

Figure 2-4: Schematic diagram of a FIB with all major components. Adapted from [83].

FIB systems most commonly use a liquid-metal ion source, typically Ga^+. A reservoir of heavy metal atoms is heated to near evaporation so that it starts flowing down a heat-resistant tungsten needle. At the tip, Ga forms a "Taylor cone", caused by a potential difference between the needle tip and the extractor (~ -6 kV). The apex of the cone is only 5 nm, and therefore small enough that the extractor voltage can pull Ga from the tip and ionize it by field evaporation. This effect appears because the potential barrier preventing the Ga from evaporation is lowered by the electric field,

and it can only be crossed by the ionization of the evaporating Ga atom. The current emitted from the tip is controlled by both, the suppressor and the extractor. The suppressor maintains the beam current constant by applying an electric field of up to +2 kV.

These ions are subsequently accelerated by a potential down the ion column (~ 30 kV) and pass through the aperture. There, the beam is focused by electrostatic lenses, which have been proven to be more effective for ions than magnetic lenses. Subsequently, the sample surface is scanned by the focused ion beam. On the surface, either elastic or inelastic ion-atom collisions occur. The inelastic scattering transfers some of the energy either to the surface atoms or electrons, releasing secondary electrons, which can be used for imaging. They are collected by a multi-channel plate or an electron multiplier depending on the apparatus. Furthermore, secondary ions are emitted following the secondary electrons. During the elastic scattering, surface atoms are excavated, resulting in a process called milling or sputtering. By injecting an organometallic gas just above the surface sample where the beam strikes, the material can be deposited. Almost any microstructure can be created by combining deposition and milling. For imaging purposes or milling fine structures, currents of less than 100 pA are applied to avoid surface damage. For rough structures, currents in the nA range are applied for a faster procedure [83].

2.4 Mass spectrometry

The mass spectrometer (MS) produces ions from neutral species and determines the mass of these ions based on the mass-to-charge ratio (m/z, z is the number of elemental charges) and/or the number of ions [84]. It consists of four main components (Figure 2-5): the sample inlet into the vacuum chamber (I, not shown in the Figure), an ion source (II), a mass analyzer (III), and an ion detector (IV). Various main components exist, the choice of which to use depends on the analyzing task. Here, only components and physical concepts of the HALA EPIC Low Energy mass spectrometer, which was used in this work, are explained in detail.

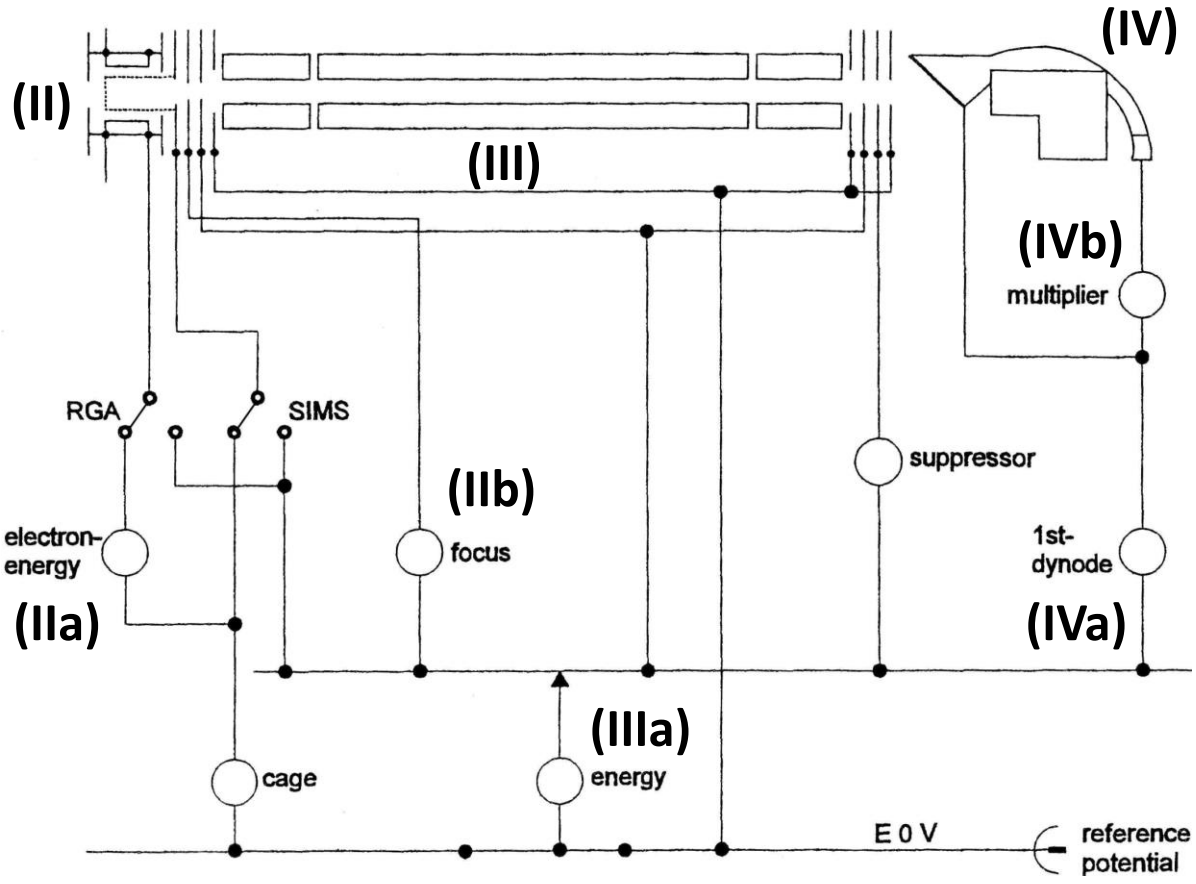

Figure 2-5: Electrodes of the HALA EPIC Low Energy mass spectrometer, adapted from [85].

2.4.1 Electron impact ionization

Electron impact ionization (EI) is the most commonly used principle for ion generation today. Electrons are emitted from a cathode (a heated filament usually made from tungsten, rhenium, or thoriated iridium) and are accelerated towards an anode (IIa). The kinetic energy of the electrons must be larger than the ionization energy (IE) of the sample molecule (e.g. IE of Ar is 15.8 eV [86]). Most of the molecules have their respective maximum of the total ionization cross section around 70 eV, which is why this electron energy is usually applied [86]. The gaseous sample molecules enter the ion source perpendicular to the electron beam and start to form positively charged molecular ions. If these ions have sufficient internal energy, they will undergo further fragmentation within a few microseconds, and the signature molecule-dependent mass spectrum is obtained [84]. These ions are drawn out of the source by a focus electrode (IIb).

2.4.2 Quadrupole mass filter

A quadrupole mass filter (QMF; III, Figure 2-5) consists of four cylindrical or hyperbolical rods which extend in z-direction in a quadratic order. A pair of opposite rods always has the same potential. In Figure 2-6 a sketch with cylindrical rods is shown, ideally, the rods should have a hyperbolical shape. The applied potential Φ_0 consist of a direct current (DC) U and a radiofrequency (RF) voltage V with the angular frequency ω.

$$\Phi_0 = U + V\,cos\omega t \tag{2.46}$$

Both pairs of rods have the same magnitude of RF but are out of phase by 180° and have an antipodal direct current. The oscillating field within the rods is given by

$$\Phi_{x,y} = \Phi_0 \frac{x^2 - y^2}{r_0^2} = (U + V\,cos\omega t)\frac{x^2 - y^2}{r_0^2} \tag{2.47}$$

where r_0 is the one-half distance between the opposite electrodes, and x and y are the distances from the center of the field. The motion of an ion through the quadrupole in x- and y-direction can be described by the Mathieu equations [87]:

$$\frac{d^2x}{d\tau^2} + (a_x + 2q_x\,cos\,2\tau)x = 0 \tag{2.48}$$

$$\frac{d^2y}{d\tau^2} + (a_x + 2q_y\,cos\,2\tau)y = 0 \tag{2.49}$$

where τ is equal to $\omega t/2$, and the dimensionless parameters a and q are given by

$$a_x = -a_y = \frac{8eU}{m\omega^2 r_0^2} \tag{2.50}$$

$$q_x = -q_y = \frac{4eV}{m\omega^2 r_0^2} \tag{2.51}$$

The quadrupole itself does not induce any acceleration in z-direction. The velocity is determined by the kinetic energy of the ion leaving the ion source and by the setting of the energy electrode (IIIa, mid axis potential). For a high mass resolution, the ions must experience a minimum number of RF cycles. If they are too slow, they will

experience too many cycles, and too many ions of the correct mass-to-charge ratio will be ejected. This results in a good mass resolution but low sensitivity. If the ions are too fast, the opposite will happen: the ions will not experience enough RF cycles, resulting in a poorly resolved mass scale, but high sensitivity.

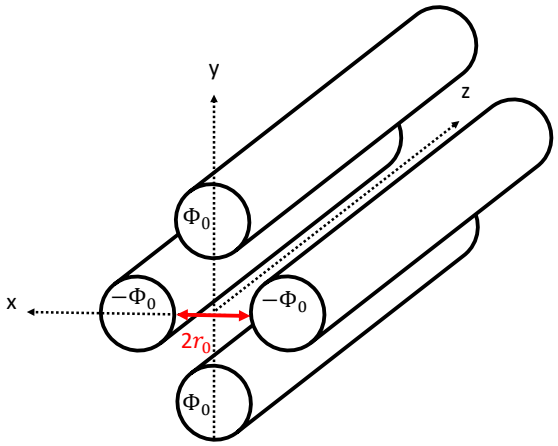

Figure 2-6: Sketch of a linear quadrupole analyzer, adapted from [88].

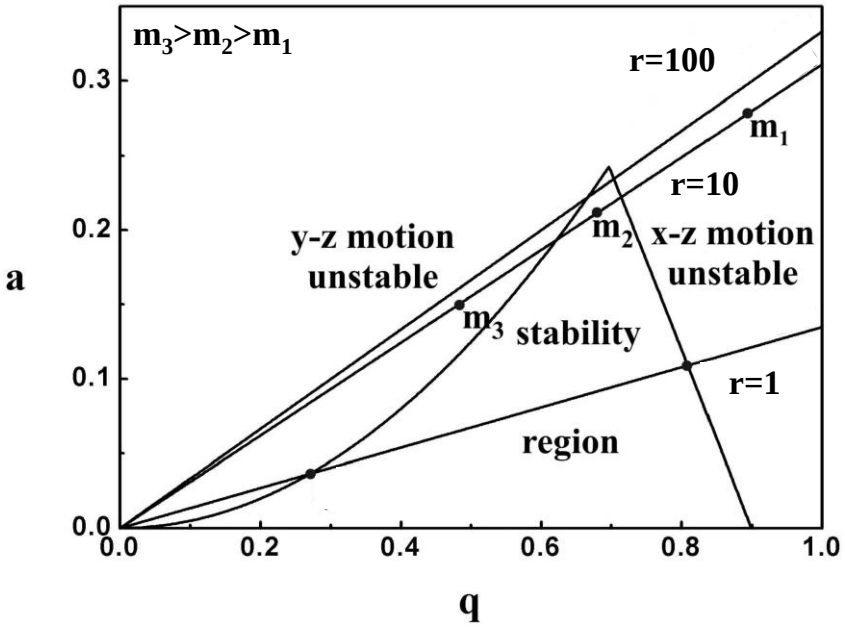

Figure 2-7: Stability diagram of a QMF with mass scan lines of different resolution r, adapted from [89].

The Mathieu equation has stable solutions when $|x|$ and/or $|y|$ do not exceed r_0. When both x and y have stable solutions, the ions that are oscillating within $2r_0$ between the rods have a stable trajectory, whereas ions that exceed this value (unstable solution) are ejected from the quadrupole and will not be detected [88]. Figure 2-7 shows a stability diagram that also describes the performance of the quadrupole mass filter.

The stable region is the interface of the stable y-z and x-z motions. Out of this region either the y-z motion is stable while the x-y is not, or vice versa. The straight lines in the diagram are called mass scan lines: their slope s depends on the setting of the RF and DC voltage.

$$s = \frac{2U}{V} = \frac{a}{q} = \frac{\Delta a}{\Delta q} \tag{2.52}$$

Furthermore, the mass resolution r is defined as:

$$r = \frac{m}{\Delta m} = \frac{a}{\Delta a} = \frac{q}{\Delta \mathrm{q}} \tag{2.53}$$

Figure 2-7 shows that the highest mass resolution is gained at the apex of the stability region. For the example of r=10 with m_2 in the stable region, the higher mass m_3 will have y-unstable trajectories, whereas the lower mass m_1 will have x-unstable trajectories. The ratio of U/V determines the mass resolution. By changing the absolute magnitude of U, and V, ions of higher mass are brought into the stability region from left to right. Alternatively, the magnitude of U and V can be fixed and the RF can be changed [89].

2.4.3 Secondary electron multiplier

The secondary electron multiplier (SEM) is the most common detector in mass spectrometry today, because of its high sensitivity and fast measurement [84]. The ions leaving the QMF are accelerated to the first dynode by a negative potential (IVa Figure 2-5, detail in Figure 2-8). The dynodes are made from metals or semiconductors. Due to the impact of the ions, secondary electrons are emitted from the surface. These electrons will be accelerated to the next dynode, which has a positive potential, and several more secondary electrons are emitted. Usually, electrons will pass through between 12 and 20 dynodes, with a high voltage of 1-3 kV (IVb) between the first (conversion dynode) and the last dynode (anode). In this way an amplification of the ion current by a factor of 10^6 to 10^8 is possible. The lifetime of an SEM is limited since the first dynode can only emit between 0.1 and 10 C of charge [87,88]. However, a simple Faraday cup – a commonly employed ion detector - only measures the current of the ions leaving the mass filter, resulting in poor sensitivity.

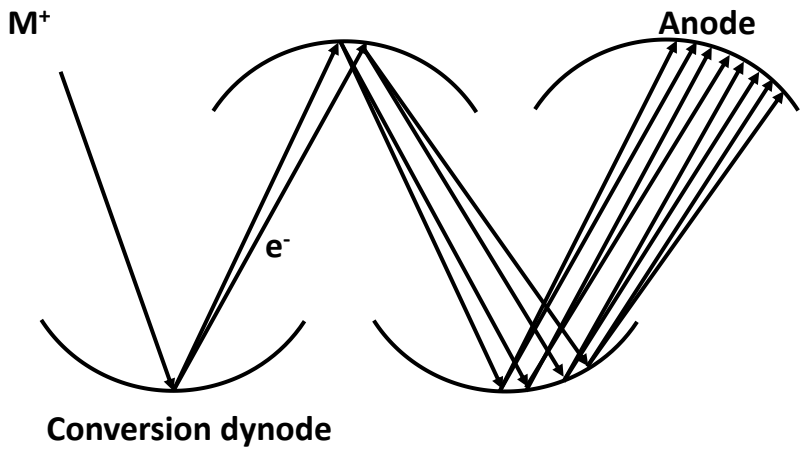

Figure 2-8: Principle of an SEM with dynodes, adapted from [87].

2.5 Raman spectroscopy

Raman spectroscopy is a method of studying rotational or vibrational states of molecules or phonons in a crystal lattice; it was discovered by Raman in the 1920s [90]. The Raman effect is an inelastic scattering of light on molecules in which the incident electric field induces a dipole on molecules. In this process, the molecules will change their vibrational and/or rotational state, resulting in an energy transfer. Therefore, the scattered light will have a higher (anti-Stokes), if they were already excited, or a lower (Stokes) frequency than the incident light. However, elastic scattering (Rayleigh scattering), which does not change the frequency of the incident photons, will occur simultaneously with intensities that are of a factor 10^3 stronger than the Raman scattering. In contrast to IR spectroscopy, homonuclear, diatomic molecules are Raman active - allowing, for example, studies of O_2 and N_2 [91].

2.5.1 Rotational Raman spectra

To have a rotational Raman spectrum, the polarizability of a molecule needs to be anisotropic. This is the case for all linear and di-atomic molecules. The selection rules for linear molecules, which are the only ones used in this work, are $\Delta J = 0, \pm 2$, where J is the rotational quantum number. $\Delta J = 0$ does not change the frequency of the scattered photon and is as a result part of the Rayleigh scattering. For $\Delta J = +2$, the

molecule will be in a higher energy level, thus absorbing energy and shifting the wavenumber to a lower value compared to the incident number $\tilde{\nu}_A$. The permitted energy levels for Stokes lines which will appear at the wavenumbers $\tilde{\nu}$ for the rotational quantum numbers $J = 0,1,2,3$ ..., are given in the following:

$$\tilde{\nu}(J+2 \leftarrow J) = \tilde{\nu}_A - 2B(2J+3) \tag{2.54}$$

B is the rotational constant, which is molecule-specific and its values can be found in literature. For $\Delta J = -2$, the emitted photons will have higher energy and the wave number will be shifted to higher values. Below are the Anti-Stokes lines:

$$\tilde{\nu}(J-2 \leftarrow J) = \tilde{\nu}_A + 2B(2J-1) \tag{2.55}$$

The different energy-levels and a schematic drawing of the resulting spectrum are shown in Figure 2-9. The relation for the Raman line intensity I_R of the scattered light for a rotational transition between state $J = i$ and f for most processes is given by [92]:

$$I_R \propto N\, f(i)\, \tilde{\nu}_{(i,f)}^4 S(i,f) I_L \tag{2.56}$$

with the number of scattering molecules per volume unit N, the fraction of molecules in the initial state $f(J = i)$, the frequency of scattered radiation $\tilde{\nu}(i,f)$, the Raman transition probability $S(i,f)$, and the intensity of the incident laser I_L. In equilibrium, $f(i)$ can be expressed by the Boltzmann distribution function.

$$f(i) = \frac{g_i e^{-\frac{E(i)}{k_B T}}}{Q_{rot}} \tag{2.57}$$

The parameters of this equation will be defined for a rigid rotator below. For other molecules, the reader is referred to [91,93,94]. g_i is the degeneracy of the level i and can be calculated with the following equation:

$$g_i = 2J + 1 \tag{2.58}$$

The rotational partition function Q_{rot} with:

$$Q_{rot} = \frac{k_B T}{hcB} \tag{2.59}$$

with the Planck constant h and the speed of light c. The energy of the rotational level with $J = i, E(i)$ can be calculated as:

$$E(i) = hcB\, J(J+1) \tag{2.60}$$

However, even and odd values of J are not always populated the same way. For molecules that are exchanging identical cores during rotation, the Pauli principle needs to be considered. For homonuclear, di-atomic molecules, with the spin quantum number I, the relation between the occupations of even and odd J is given as [91]:

$$\frac{number\ of\ ways\ of\ achieving\ odd\ J}{number\ of\ ways\ of\ achieving\ even\ J} = \begin{cases} \dfrac{I+1}{I} & for\ half-integral\ \ spin\ nuclei \\ \dfrac{I}{I+1} & for\ integral\ \ spin\ nuclei \end{cases} \tag{2.61}$$

Note that heteronuclear molecules are not affected by spin-statistics [95].

2.5.2 Vibrational Raman spectra

To have a vibrational Raman spectrum, the polarizability of a given molecule needs to change during vibration. The specific selection rule is the quantum number variation $\Delta v = \pm 1$, where v is the vibrational quantum number. The lines for Δv = -1 will be at higher wavenumbers than the incident laser and are called anti-Stokes lines; whereas for $\Delta v = +1$, they will be at a lower wavenumber and are called Stokes lines. The energies G of the different vibrational quantum numbers expressed in wavenumbers are [91]:

$$G(v) = \left(v + \frac{1}{2}\right)\tilde{\nu} \tag{2.62}$$

The wavenumbers of the allowed vibrational transitions $\Delta G_{v+1/2}$ for $v+1 \leftarrow v$ are:

$$\Delta G_{v+1/2} = G(v+1) - G(v) = \tilde{\nu} \tag{2.63}$$

The number of molecules in each vibrational level is dependent on the Boltzmann distribution [93]:

$$N_v = \frac{N}{Q_{vib}} e^{-\frac{G(v)hc}{k_B T}}, \tag{2.64}$$

where Q_{vib} is the vibrational partition function. For higher vibrational energy levels, the motion of a molecule becomes anharmonic, meaning the restoring force on the atom is not proportional to its displacement anymore. This causes a shift in the upper vibrational Q-branches because the energy difference between the upper vibrational states is decreasing. Therefore, these lines will appear closer to the incident wave number and are visible in a vibrational spectrum. This is exemplarily shown for the Stokes bands in Figure 2-9. Thus, the energy levels need to be corrected with the anharmonicity constant x_e [91]:

$$G(v) = \left(v + \frac{1}{2}\right)\tilde{\nu} - \left(v + \frac{1}{2}\right)^2 x_e \tilde{\nu} \tag{2.65}$$

In gas phase spectra, the rotational lines are superimposed on vibrational ones. The same selection rules as for pure rotational spectra apply. Therefore, in the spectrum, an O-branch ($\Delta J = -2$), a Q-branch ($\Delta J = 0$) and an S-branch ($\Delta J = +2$) appear, which is shown for the vibrational Anti-Stokes bands in Figure 2-9 [91].

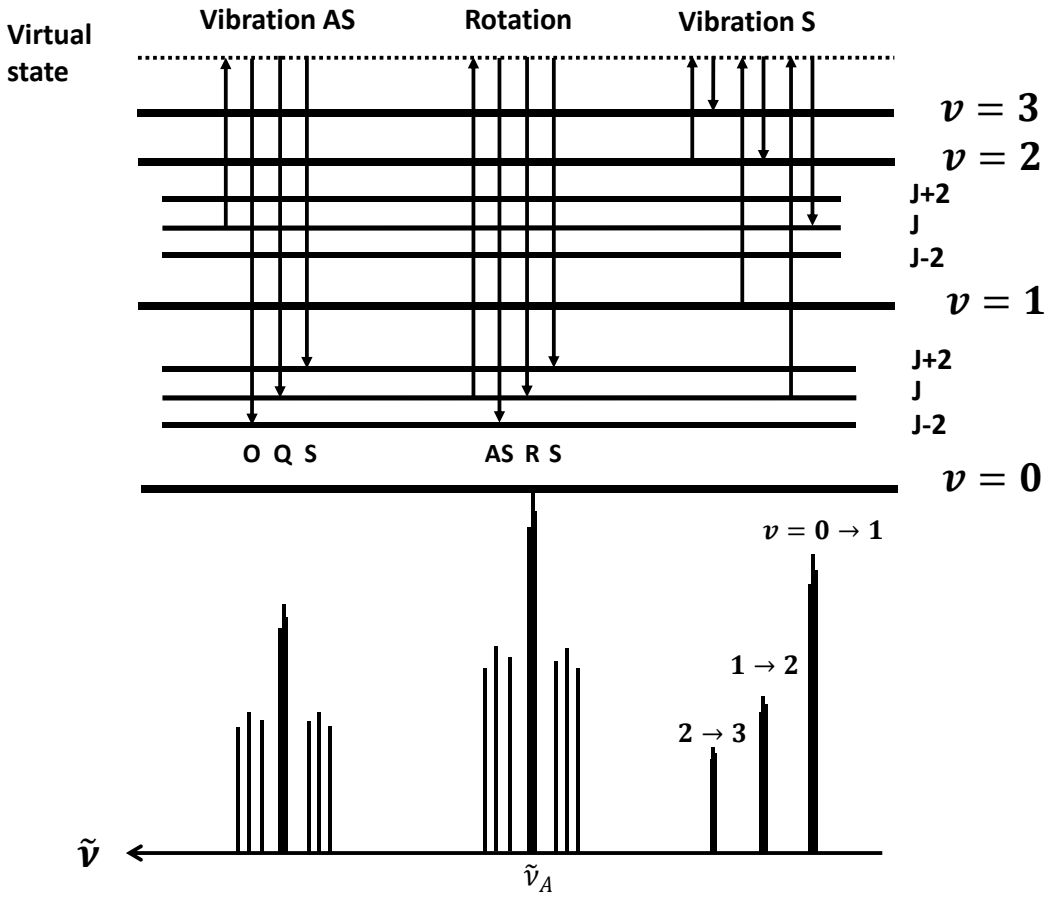

Figure 2-9: Energy-level representation of Raman scattering and resulting spectra for vibration-rotation Anti-Stokes (AS) with O, Q, and S-branch, rotation including Rayleigh scattering (R) at $\tilde{\nu}_A$and vibration Stokes (S) with anharmonicity of the upper vibrational states, adapted from [96].

3 Materials and methods

In this chapter, the newly developed set-up is explained (3.1), details are given about the prototype platinum coated alumina catalyst (3.2), the preparation of the sampling channel inside the particle (3.3), and the sampling capillary (3.4). Furthermore, the configuration and connection of the mass spectrometer (3.5.1) and the data analysis for the samples taken are described (3.5.2). Furthermore, the set-up is presented which combines the profile sampling technique with Raman spectroscopy (3.6.1) and it is presented how the spectra can be analyzed to gain spatial gas phase and temperature profiles (3.6.2).

3.1 Reactor set-up

The reactor is designed to measure concentration profiles inside and around a single porous catalyst pellet, in a defined flow and temperature field. The reaction chamber is in the center and has a width of 2 cm, a height of 2 cm, and a length of 6 cm (Figure 3-1). On both the left and the right, a heating block is mounted; each is heated by two cartridges with a maximal power of 100 W (Friedr. Freek GmbH, Menden, Germany). During operation, the inlet temperature is kept constant by a PID controller (Eurotherm, Worthing, UK). The temperature in the reactor is measured with a Type K thermocouple (TMH, Maintal, Germany) and recorded by a Pico USB TC-08 Temperature Logger (Pico Technologies, St. Neots, UK). To avoid heat losses, insulation material with a thickness of 2 cm is built around the reactor. However, for spectroscopic measurements (e.g. Raman spectroscopy), the insulation material from the top of the reaction chamber can be removed (as shown in Figure 3-1), and the reactor is optically accessible by a glass window. For the detailed set-up of the reactor in combination with a Raman microscope see Chapter 3.6.

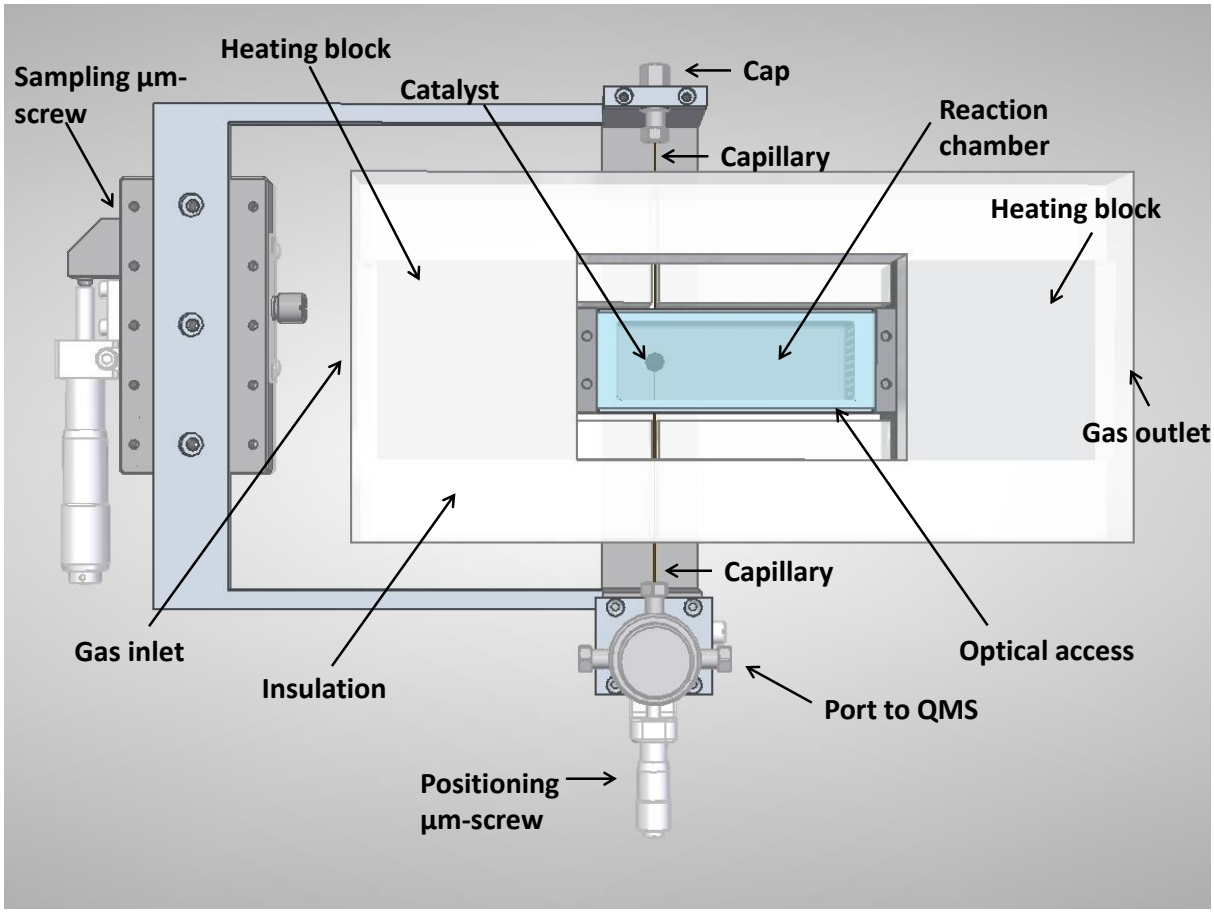

Figure 3-1: Top view of the reactor set-up.

Reactant gases (CO and O_2, as well as Ar as inert) were fed via calibrated mass flow controllers (Brooks instruments, Hatfield, USA) from the left side, and were leaving the reactor on the right. The details of the inside of the reactor are shown in Figure 3-2. Gases were mixed, then sent via either 1/4" or 1/8" pipes to the reactor where the diameter was conically increasing to 2 cm x 2 cm. Subsequently, a flow distributor was passed before entering the reactor chamber to avoid flow maldistributions (Figure 3-2, inlet). The catalyst was mounted on a magnesia rod (Figure 3-2, holder) with an alumina-based adhesive (Ceramabond 569, Kager Industrietechnik, Ditzenbach, Germany) to withstand high temperatures. It was possible to orient the particle at different angles to the flow. In some experiments, a hole with a diameter of 300 µm and a depth of 2 mm was drilled into the pellet, to place a thermocouple (250 µm diameter) directly inside - and thus measure the temperature within the pellet.

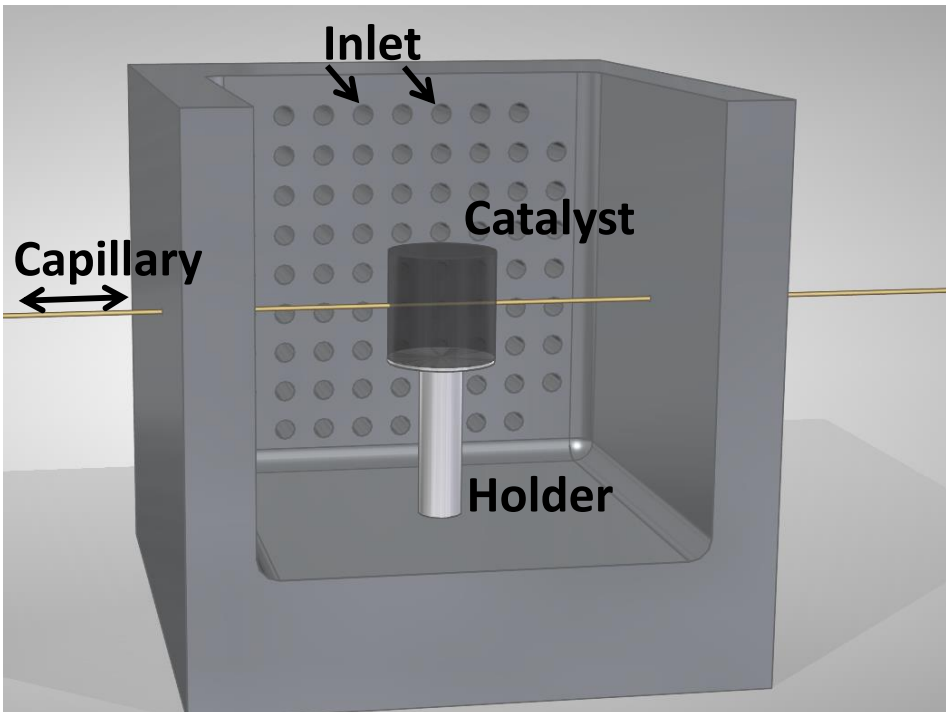

Figure 3-2: Detail of the inside of the reactor.

Sampling was done with a fused silica capillary passing through the drilled channel in the catalyst pellet (details in Chapter 3.3), horizontally to the flow. The capillary exited through the reactor wall and was inserted in a T-port (Figure 3-1), which was connected via a transfer line to the vacuum chamber of the Quadrupole mass spectrometer (QMS). Samples from within the catalyst pellet or the boundary layer were taken through the tip of the capillary or a side orifice in the wall of the capillary (Figure 3-3). When sampling with the tip (not shown in Figure 3-1 and Figure 3-2), the capillary could be moved through the reactor either with the sampling or the positioning μm screw. Both have a resolution of 10 μm.

For sampling with the side orifice, the other side of the capillary exited through the opposite reactor wall, the tip of the capillary was sealed and was fixed inside a cap. In this case, the positioning μm screw was used for fixing the capillary in the right position and keeping it under tension during the experiments. Only the sampling μm screw could be used for moving the capillary through the reactor. This way, it was possible to measure the gas phase concentration inside the catalyst pellets with fewer disturbances in comparison to a one-side open channel; and it was possible to measure in the boundary layer on both sides of the pellet.

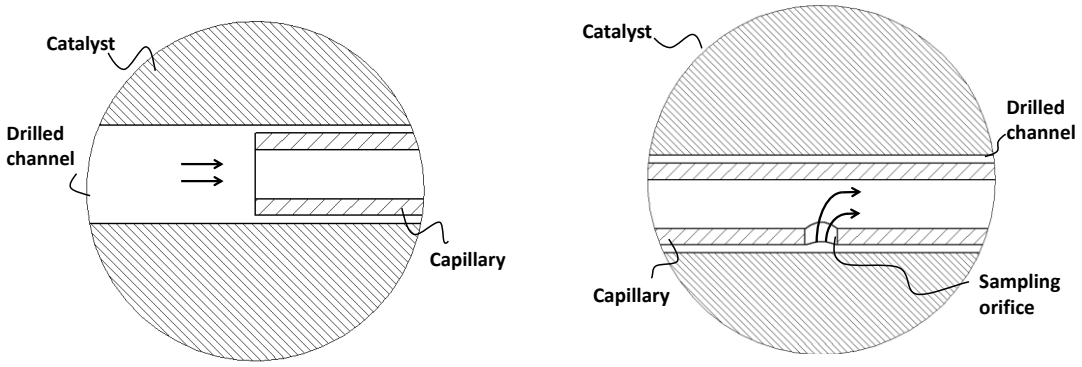

Figure 3-3: Detail of the sampling. Left: sampling with the tip of the capillary. Right: sampling with a side orifice inside the capillary.

3.2 Catalyst

The catalyst used in this study was a platinum-coated, porous alumina cylinder. The γ-alumina support (length 5 mm, diameter 5mm) was kindly provided by Sasol Germany GmbH (Hamburg, Germany). The particle had the following properties: density 1168 kg m^{-3}, porosity 0.55, BET surface area 203 m^2 g^{-1}, average pore radius 47 Å, and thermal conductivity 0.1 W m^{-1} K^{-1}. Surface area and pore size were determined with a Quantachrome autosorb IQ 2 (Anton Paar GmbH, Graz, Austria) and the thermal conductivity with a C-Therm TCiTM thermal conductivity analyzer (C-Therm Technologies Ltd., Fredericton, Canada). A 3 wt.% platinum/alumina loading was prepared by incipient wetness impregnation with an aqueous solution of H_2PtCl_6 * $6H_2O$ (~40% Pt, Carl Roth GmbH, Karlsruhe, Germany) as precursor, and dried in a desiccator. Subsequently, the catalyst was reduced in a tubular furnace with 5% H_2 in N_2 (V_{total}=450 ml min^{-1}) at a temperature of 500 °C for 5 h.

3.3 Sampling channel

The channel in the particle was mechanically drilled into the catalyst support before impregnation. A spindle speed of 15000 rpm was applied, and a tungsten carbide micro drill with a diameter of 300 μm and a length of 5.5 mm was used. These drills can be produced with diameters as small as 25 μm and a maximal aspect ratio (length to diameter) of 30:1. The drilling process might cause problems with harder materials, such as α-alumina, which is another commonly used catalyst carrier. The

Mohs hardness of α-alumina is nine, compared to six of γ-alumina [97]. Nevertheless, machines with spindle speed above 150000 rpm might overcome this issue.

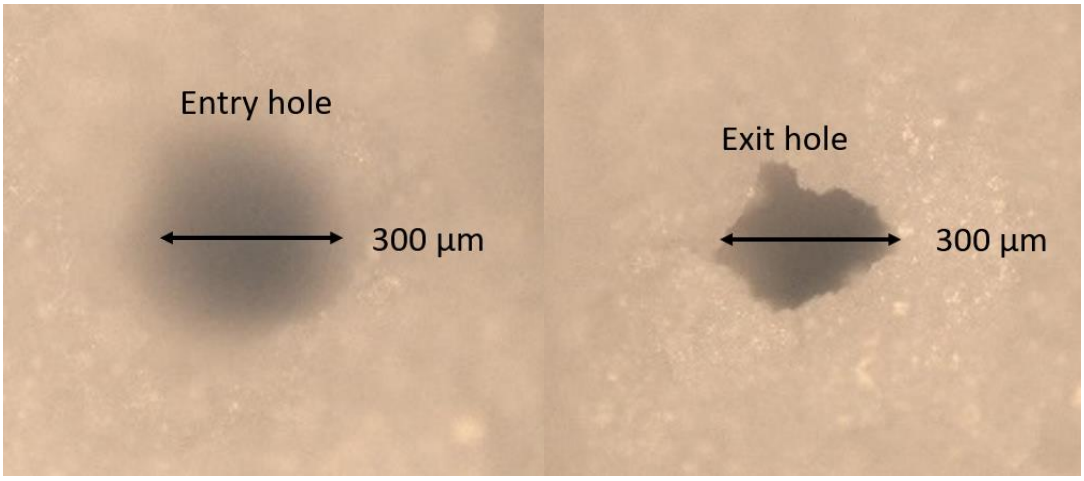

Figure 3-4: Holes by laser drilling in an alumina cylinder of 2.5 mm depth, left picture showing the entry, right picture the exit hole.

For higher aspect ratios and harder materials, laser drilling could be a solution. This method allows for aspect ratios as high as 50:1, and it is possible to handle nearly any material (e.g. ceramics, metals, semiconductors) [98]. A test drill was conducted by Ter Hoek (Rijsen, Netherlands) on the γ-alumina cylinders. The cylinders were cut in half, resulting in a depth of 2.5 mm, and a 200 µm-diameter channel was attempted. However, as visible in Figure 3-4, the entry and exit holes do not have the same diameter, highlighting the drawback of this method: the conical shape of the laser cannot create evenly-sized holes. This can be solved by drilling the particle from both sides, but it is not clear if that will work for the depth of a full 5 mm cylinder as well. Another possible technique with potentially high aspect ratios is electron beam drilling. However, this method is highly dependent on the material of the catalyst and the wanted aspect ratio. For a summary of micromachining methods, the reader is referred to [99]. An interesting approach warranting further research would be to build the catalyst around the capillary to ensure a tight fitting.

3.4 Sampling capillary

To disturb the particle as least as possible the sampling volume should be as low as possible. However, it needs to be still detectable by the QMS. The sampling volume can be controlled by taking capillaries of different IDs. This volume flow can be

calculated with the Hagen-Poiseuille equation for gases (Equation 3.1 [100]); where p_1 represents the pressure inside the reactor, p_2 that of the vacuum system, d the inner diameter of the capillary, and l the length of the latter.

$$\dot{V} = \frac{\pi}{256}\frac{1}{\eta}\frac{d^4}{l}\frac{{p_1}^2 - {p_2}^2}{p_1} \tag{3.1}$$

Unfortunately, the equation seems to overestimate the sampling flow rate, as demonstrated by Sa et al.[26]. They measured a flow rate in a 75 µm ID capillary that was less than 10% of the calculated one, therefore Equation 3.1 was considered as a worst-case scenario.

The calculated sampling rates for different tested capillary dimensions can be found in Table 3-1. The pressure in the vacuum chamber was below $2 \cdot 10^{-7}$ mbar, therefore it could be neglected. l is defined as the length of the capillary from the T-port to the sampling point, which is 7 cm. The sampling capillaries are made of fused silica and are coated with polyimide (Polymicro Technologies, Phoenix, USA). The coating was removed on the part of the capillary that was inside the reactor.

Table 3-1: Dimensions of the capillaries used and the corresponding sampling volumes.

ID [µm]	OD [µm]	Sampling Volume [nL/min]
10	130	500
5	130	30
2	130	0.8
0.3	320	0.004

To fill the entire channel in the particle with the capillary, a side orifice needed to be opened in the capillary. This was done by milling a hole with a FIB microscope (FEI Strata 205, TSS Microscopy, Beaverton, USA), operated with 30 kV and 20 nA. To avoid missing the inner channel of the capillary, it was aimed for an orifice diameter of 15-25 µm. As can be seen in Figure 3-5, the holes are conical, resulting in a smaller diameter in the center. Furthermore, the back wall of the capillary got damaged. Unfortunately, this could not be avoided since the inner channel of the capillary was too small to insert protection (e.g. a wire). Moreover, the capillary could not be sputtered with gold for a better discharge, since gold nanoparticles can be used as a catalyst for CO-oxidation [101]. Therefore, results were not always reproducible since the surface got sometimes charged which slowed down the milling process and/or the channel got blocked. The milling process of fused silica can be optimized by

inserting XeF_2 [83]. The XeF_2 physiosorbs on the surface, and by ion impact reacts to SiF_4, which enhances the milling rate seven to ten times. Another alternative for better results might be selective laser-induced etching [102]. In this technique, a transparent volume is chemically changed by absorbing energy from an ultrashort pulse laser. This volume can subsequently be etched by KOH, allowing for precise holes with high aspect ratios to be created.

Figure 3-5: Side sampling orifice, from the top (left) and the side (middle) with a laser scanning microscope. The right side shows another orifice, taken with the FIB.

3.5 Mass spectrometry

3.5.1 Set-up

Mass spectra were measured with a QMS equipped with an SEM (HAL 510, Hiden Analytical, Warrington, England). Due to the low sampling flow rate withdrawn from the catalyst pellet, pressure in the QMS vacuum chamber was below $2*10^{-7}$ mbar. To achieve higher sensitivity, the samples were fed directly into the ionizer of the QMS, and the mid-axis potential of the probe was decreased, to increase the speed of the (positive) ions down the mass filter. This way, more ions pass through the mass filter, but they do not experience the minimum number of RF cycles required, resulting in a loss of mass resolution. However, the latter resulted in a gain of sensitivity, a compromise that could be made in this study because all species had sufficiently different masses (CO, O_2, CO_2, and Ar at m/z=28, 32, 44, and 40 amu respectively).

In tests with a QMS with Faraday cup (QME 220, Pfeiffer Vacuum, Aßlar, Germany), no signals of the sampling species were detected, when sampling with a 10 µm ID capillary.

3.5.2 Data evaluation

For evaluation, the base peak of each component was integrated, and the peak area was converted into a mole fraction value by using the argon peak area as an internal standard. Each sampling point was measured three times at least. By sampling only Argon, strong background signals at m/z=28 and 32 were detected (up to 50 % of the Ar peak, while sampling with a 10 µm capillary), probably originating from leaking air, even though no helium peaks were detected when testing all connections for leakages. The leaking rates might be minimal, but since the aperture consists of several connectors and the sampling rates are low, they add up in the background as a result. The background could be reduced to less than 10 % (with a 10 µm capillary) by feeding the samples directly into the ionization head. However, the background increased with decreasing sampling volume as can be seen in Figure 3-6: with a 10 µm ID capillary, the background of CO_2 was less than 0.5 % of the Ar signal (y-axis intercept), whereas it was more than 25 % with the 2 µm ID capillary. Furthermore, the time between each sampling point needed to be increased with decreasing sampling volume. Equilibrium in the QMS was reached after 2-3 minutes with the 10 µm capillary whereas 20 minutes were needed with the 2 µm capillary.

The background was not found to be stable, and therefore the y-axis intercept of the calibration lines was determined at least once a day during experiments. On the contrary, the slopes of the calibration lines were stable and were reassessed only after changing the set-up. By changing the mid-axis potential, the coefficients of determination are decreasing. This can be counteracted by decreasing the mass increment to the minimum (0.01 amu). Furthermore, a higher background caused higher uncertainties as shown in Figure 3-6: the standard deviation increased with an increasing background. Thus, the standard deviation of the O_2 and CO concentrations was higher than the one of CO_2 (see Figure 5-2 and Figure 5-3).

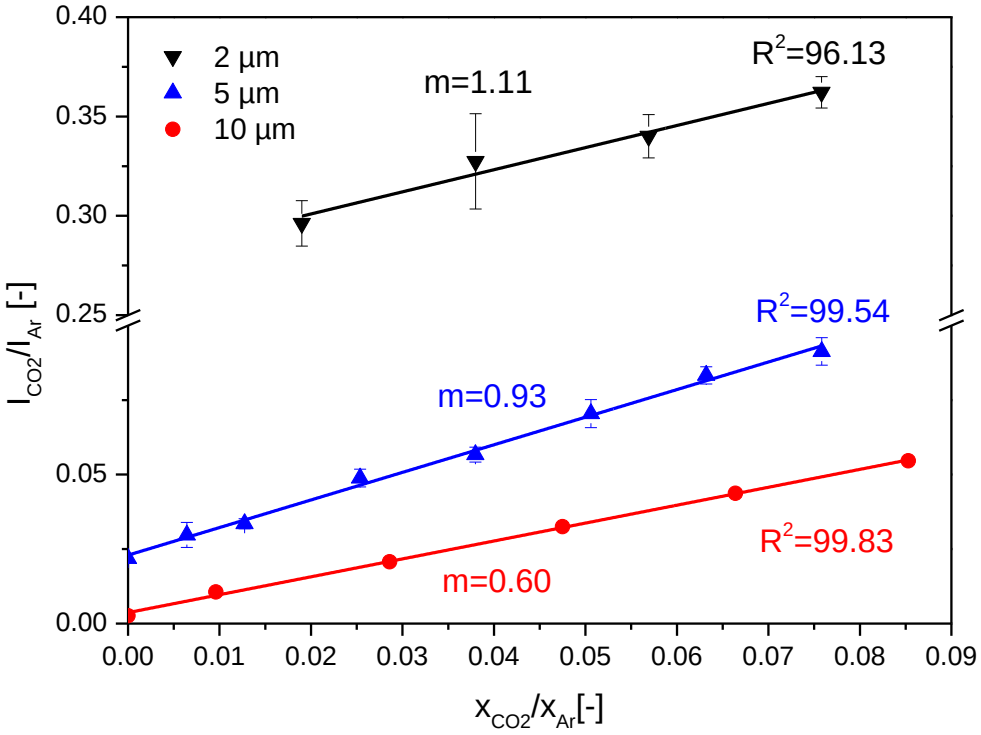

Figure 3-6: Calibration lines of CO_2 with standard deviation resulting from three measurements for capillaries with an inner diameter of 2, 5, and 10 µm.

The calibration lines were determined by the intensity ratio of each species I_i and argon I_{Ar}, hence, a ratio X_i between the molar fraction of each species x_i and the molar fraction of the inert x_{Ar} was obtained. Since the total number of moles decreases during the CO-oxidation, x_{Ar} could not be determined directly and x_i was calculated by solving the following linear equation system:

$$\frac{x_i}{x_{Ar}} = X_i \qquad for\ i = CO, O_2, CO_2 \tag{3.2}$$

$$\sum_i x_i + x_{Ar} = 1 \tag{3.3}$$

3.6 Raman spectroscopy

3.6.1 Set-up

Raman spectra were recorded by a triple filter Raman spectrometer (TriVista 557 S&I GmbH) with a liquid nitrogen cooled CCD camera (Princeton Instruments) as the detector. The spectrometer was attached to a microscope (Olympus, BX51WI), using a frequency-doubled Nd:YAG laser with a wavelength of 532 nm for excitation. The reactor was placed underneath the microscope on a positioning stage with µm-resolution in x and y-direction. The objective (Olympus, LMPLFLN10X, 10x objective with 21 mm working distance) was placed in between the insulation in the opening of on top of the reactor (see Figure 3-1). For temperatures above 100 °C, the heat was accumulating at this point and the objective needed to be cooled by a fan. By moving the stage and the height (z-axis) of the objective, the laser could be focused through the glass window at different positions inside the reactor to get spatial profiles. In this work, only the feasibility of the method is demonstrated. Raman measurements were conducted without reaction, to avoid concentration gradients inside the reactor, which will make the evaluation more complicated. The reactor was heated at different temperatures, and different mixtures of nitrogen and oxygen were steadily flowing through it. From observed rotational and/or vibrational bands, it is possible to gain information about temperature, concentrations, and adsorbed species on the catalyst particle. Nitrogen, oxygen, and hydrogen have been proven the most accurate for Raman temperature measurements in literature [96]. Vibrational bands were measured with one spectrometer and a notch filter for stray light rejection. Pure rotational bands appear close to the laser wavelength; therefore, a better stray light rejection is needed. This is gained by operating the spectrometer in triple subtractive mode. It consists of three spectrometers in a row, allowing measurements of wave numbers as close as 10 cm^{-1} to the laser. Laser intensities up to 500 mW could be employed. The intensity on the sample was not measured; however, mirrors and lenses of the aperture will result in a loss of power, and the actual intensity on the sample will be less.

For temperature calibration measurements, the laser was focused on the tip of a Type K thermocouple (TMH, Maintal, Germany) inside the reactor. Subsequently, the laser was switched off and the temperature was measured with the thermocouple. For the following Raman measurement of the gas phase, the thermocouple was pulled out of the focus to avoid any interactions with the laser.

By employing confocal Raman spectroscopy, data can be acquired with volumetric resolutions of a few μm^3 [103]. However, the microscope used in this work does not have a confocal aperture, which decreases the resolution, especially in the z-direction (focus axis of the microscope), as shown in Figure 3-7. The path of the scattered light is focused on a point C in a confocal microscope. The confocal aperture rejects most of the scattered light from points B and A, and mainly stray light from C passes through. Therefore, without the confocal aperture, the Raman spectrum of point C will be distorted from other planes. For a 50x objective without pinhole, Tabaksblat et al. [104] measured a depth resolution of only one tenth compared to a measurement with a 300 µm pinhole.

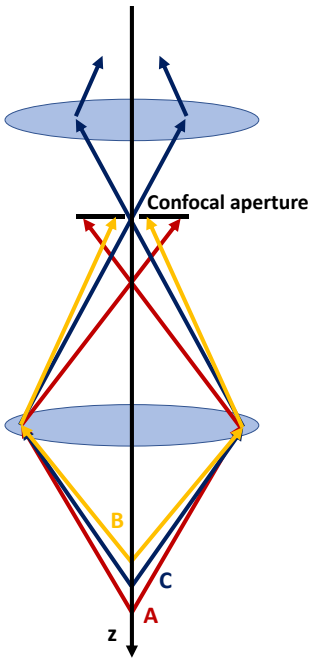

Figure 3-7: Laser that is focused at a point C. The confocal aperture is rejecting most of the stray light from A and B which are out of focus and lets mainly the stray light from C pass through. Adapted from [103].

3.6.2 Data evaluation

From the set-up in this work, three possibilities arise to measure the temperature by Raman spectroscopy. One option is to use the ratio of two different rotational lines of the same molecule. The other two originate from vibrational bands, either from the ratio of a Stokes and an Anti-Stokes band or from the ratio of two vibrational Q-branches created by different energy levels (e.g. $0 \rightarrow 1$, $1 \rightarrow 2$) [96].

By evaluating two different rotational lines - i, j respectively - of the same molecule, Equation 2.56 can be simplified to [93]:

$$\frac{I_i}{I_j} \propto \frac{g_i}{g_j} e^{\frac{E(j)-E(i)}{k_B T}} \quad (3.4)$$

resulting in:

$$T \propto \frac{E(j)-E(i)}{k_B} \ln\left(\frac{I_j}{I_i}\frac{g_i}{g_j}\right) \quad (3.5)$$

The temperature from two different vibrational states, whether Stokes/Anti-Stokes or vibrational Q-branches, can be calculated with:

$$\frac{I_i}{I_j} \propto e^{\frac{G(j)-G(i)}{k_B T}} \quad (3.6)$$

which is resulting from Equation 2.64.

To calculate relative concentrations, line intensities of either vibrational or rotational transitions originating from two different species, l, and k, can be used with Equation 2.55 [105]. Most parameters will become constant, and the following relation will result:

$$\frac{n_k}{n_l} \propto \frac{I_k}{I_l} e^{\frac{E(k)-E(l)}{k_B T}} \quad (3.7)$$

For vibrational lines G instead of E would need to be inserted. The rotational constants B used in the evaluation can be found in the following table:

Table 3-2: Rotational constant for N_2, O_2, CO, and CO_2; data are from [91].

		N_2	O_2	CO	CO_2
B	[cm^{-1}]	1.99	1.45	1.93	0.39

Spectra were integrated for at least 10 min to get a meaningful signal, and the continuum background was corrected with the method of Gornushkin et al. [106]. For evaluation, the intensity peaks were integrated to avoid high sensitivities of instrument properties.

4 CFD simulations

The proposed method aims to study the interplay of diffusion and reaction in and around a porous catalyst pellet, by a spatially-resolved sampling of the diffusive fluxes inside the particle, and in the boundary layer surrounding the pellet, using a small capillary. Before any measurements were conducted, as part of a feasibility study, the invasiveness of the sampling method was investigated using numerical simulations employing a kinetic expression for CO oxidation on a Pt catalyst taken from literature (Equation 4.1, Table 4-1). These simulations do not aim to represent the pellet and catalyst used in this thesis exactly. Their only purpose is to explore how strongly the intraparticle profiles of a pristine pellet are disturbed by the sampling process. No absolute comparisons between the simulations and the measured data were made in the present work. Two aspects of the experiment were explored numerically: first, the gap between the capillary and the wall of the channel drilled through the pellet in which the capillary moves for spatial sampling, and second, the gas flow rate sampled. In Chapter 4.1 the implementation of the model in COMSOL Multiphysics is described; and in Chapter 4.2 their results are shown.

4.1 Model implementation

A model of the reactor setup was implemented in Comsol Multiphysics® comprising the reaction chamber, the catalyst pellet, the channel, the sampling capillary, and the holder. Standard CFD equations for conservation of mass, momentum, and energy were used, and are explained in Chapter 2.2. Mass based species balances of N_g-1 species were solved and the mass balance was closed by determining the mass fraction of Argon by subtracting the sum of the other species from one. This is a common approach when one species is in high excess [82]. The gas phase density was calculated according to the ideal gas law, and thermodynamic data were calculated with the Shomate equation using parameters taken from the NIST

Parts of this chapter were published in B. Sosna, O. Korup, R. Horn, Probing local diffusion and reaction in a porous catalyst pellet, J. Catal. 381 (2020) 285–294. [107]

database [108]. The capillary was implemented as a non-permeable wall with a no-slip boundary condition at the surface. Sampling was included by defining an outlet volume flow as a boundary condition on a small circular area of the size of the ID of the capillary. The sampling volumes resulting from the different IDs can be found in Table 3-1. The flow in the reactor was laminar ($Re_p \approx 5.7$), the inlet temperature was set to 190 °C, and the inlet mole fractions of O_2 and CO were 3.2% and 5.4%, respectively. The catalyst pellet was modeled as a solid phase, which meant that convection inside the pellet was neglected. The annular gap between the channel wall and the capillary inside the catalyst pellet was treated as part of the fluid phase. The basal plane of the cylinder, which was glued to the magnesia rod, was considered to be impermeable to gases because it was fully covered by the adhesive. The reaction source term for the reaction shown in Equation 2.28 is taking place in the solid phase and was modeled with a Langmuir-Hinshelwood kinetic rate expression taken from Shishu and Kowalczyk [33]:

$$r = \frac{k K_{CO} K_{O_2} p_{CO} p_{O_2}}{\left(1 + K_{CO} p_{CO} + K_{O_2} p_{O_2}\right)^2} \qquad (4.1)$$

The equation is derived in Chapter 2.1.4. At the conditions employed in this work, gas phase reactions can be neglected [109]. The kinetic parameters can be found in Table 4-1. A constant particle pressure of 1 bar was assumed. The tortuosity was assumed as 3 based on the simulations from Wehinger et al. [18].

Table 4-1: Kinetic parameters used in the simulations.

τ	k	K_{CO}	K_{O_2}
[-]	[mol kg^{-1} s^{-1}]	[Pa^{-1}]	[Pa^{-1}]
3	$1.4E6\ e^{-45400/RT}$	$2.1E-5\ e^{10600/RT}$	$1.3E-9\ e^{24830/RT}$

For CO oxidation, it has been shown that very steep temperature and concentration gradients can occur at the surface of the catalyst particle, and CO can be consumed within less than 100 µm [18]. Therefore, 10 layers of orthogonal prismatic cells (prism layers) of 10 µm were applied inside the particle at all surfaces. They can be seen in Figure 4-1 on top of the annular gap inside the catalyst. For a better resolution of the boundary layers in the gas phase, 15 prism layers - with a layer thickness ratio of 1.1, starting from 15 µm, were implemented on the outer surface of the particle. Cells in the annular gap between the channel wall and the capillary were between 1 and

10 μm, resulting in a total count of 4.9 million. The particle itself consisted of 480000 cells. In total, the computational domain comprised 13 million cells. The mesh in the center of the catalyst including the drilled hole, the capillary, and the sampling spot is shown in Figure 4-1.

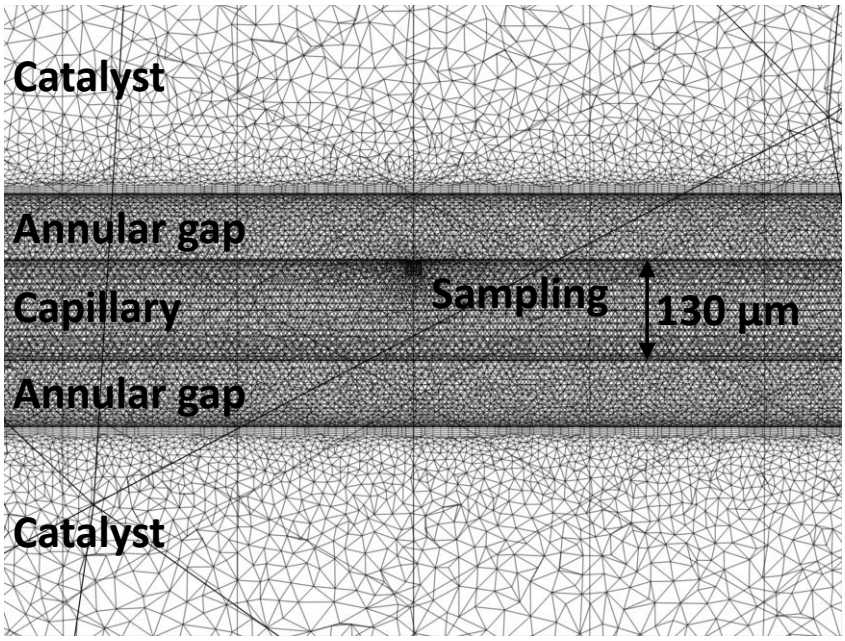

Figure 4-1: Mesh in the center of the catalyst particle with the drilled hole, the capillary, and the sampling spot.

4.2 Invasiveness of the sampling method

Two aspects of the experiment that are distorting the processes inside the particle compared to a pristine particle were explored numerically: first, the gap between the capillary and the wall of the channel drilled through the pellet (in which the capillary moves for spatial sampling); and second, the gas flow rate sampled.

Figure 4-2 shows simulations of the pristine catalytic pellet (Figure 4-2a), of the drilled pellet with the capillary going through the entire channel (Figure 4-2b), and of the drilled pellet with the capillary partially penetrating the channel (Figure 4-2c).

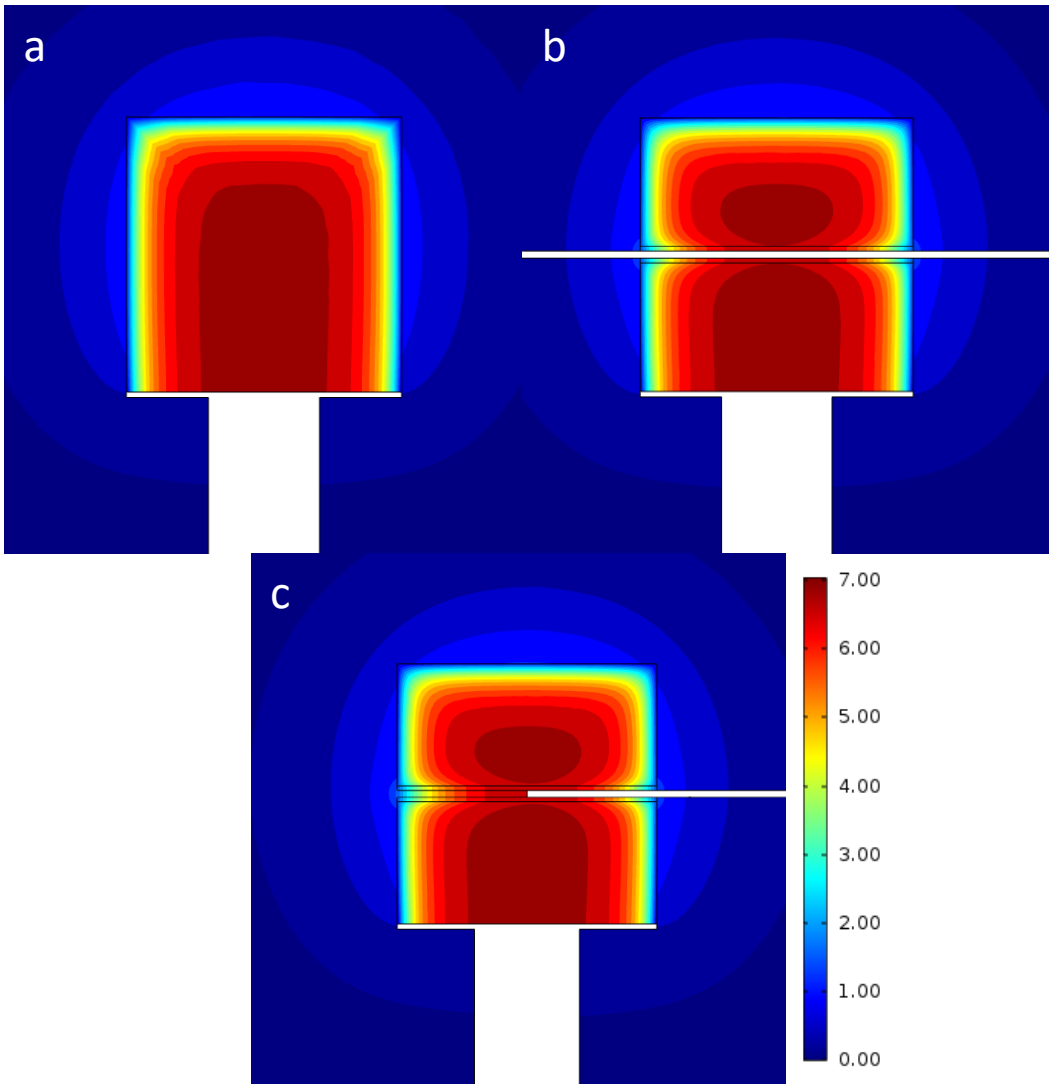

Figure 4-2: CO_2 fractions in mole-% around and inside the pristine catalyst pellet (a), the drilled pellet with the capillary going through the entire channel (b), and the drilled particle with the capillary not going through the entire channel (c).

At first sight, the center fraction of CO_2 seems unexpectedly high. At full conversion, the resulting mixture would contain 5.55 mole-% of CO_2. However, the process is diffusion limited and Knudsen diffusion is prevailing. Therefore, the profiles are controlled by the Knudsen diffusion coefficient which is proportional to $M_i^{-0.5}$, and therefore $D_{CO,K} > D_{O2,K} > D_{CO2,K}$ which is causing different relative diffusion velocities of the species to each other. This causes higher CO_2 fractions in the center of the pellet than what stoichiometry predicts at full conversion.

The channel through which the capillary moves, influences the CO_2 concentration gradient by an increased diffusion of educts through the gap. The average diffusional flux per unit area through the surface between the bulk and the gap is about ten times higher than the average flux through the outer particle surface. The average

convective fluxes per unit area through the gap are less than one percent of the diffusive fluxes and can be neglected. Thus, the flux through the gap is controlled by fast molecular diffusion (Equation 2.42), whereas the flux into the particle is controlled by a combination of the reaction rate (Equation 4.1) and the slower effective diffusion (Equation 2.13). If the sampling capillary does not extend through the entire channel, the CO_2 distribution becomes slightly asymmetric due to enhanced diffusive and convective fluxes through the open side of the channel.

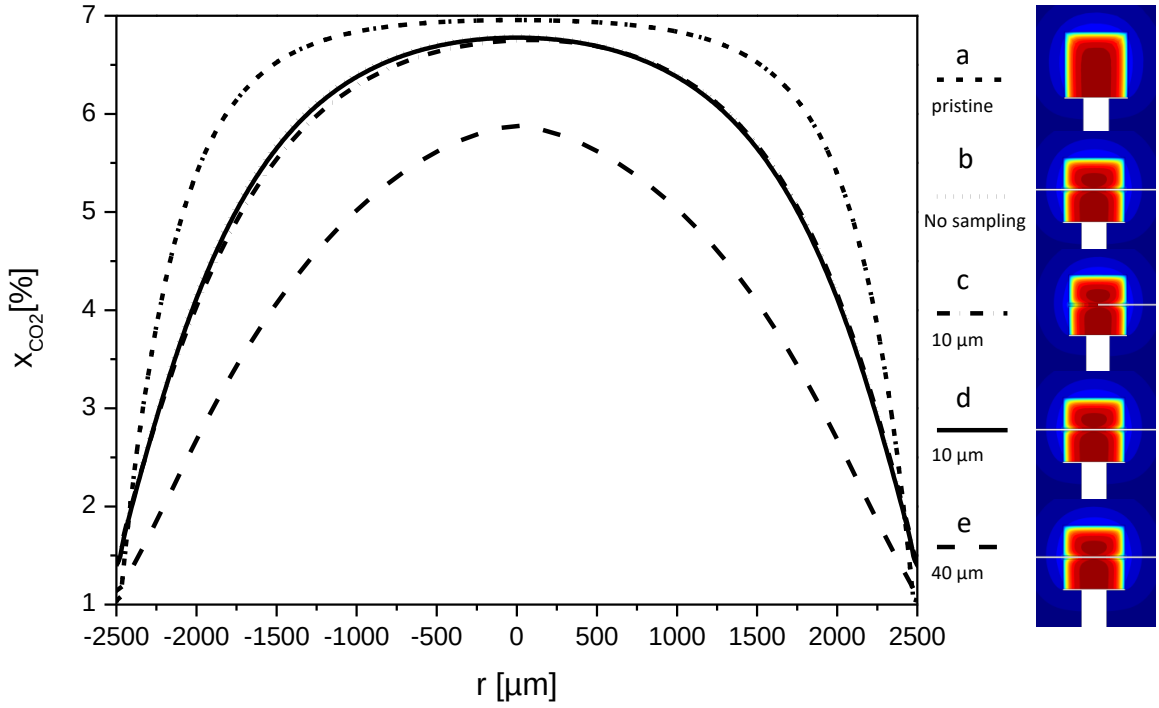

Figure 4-3: Simulated CO_2 fractions inside the cylindrical catalyst pellet. : a) no channel (short dashed line), b) capillary going through the whole channel without sampling (dotted line, not visible because underneath the solid line), c) sampling through the tip of a 10 µm ID capillary (dash-dotted line), d) sampling through a side orifice inside a 10 µm ID capillary (solid line), and e) sampling through a side orifice inside a capillary of 40 µm ID (long dashed line).

To get a more quantitative picture of the invasiveness of the method, and the effect of extracting a continuous sample flow from within the pellet, stemming from the previous figure, Figure 4-3 shows the CO_2 profile along the top of the capillary for five different scenarios: a) pristine pellet, b) capillary going through the whole channel without sampling, c) sampling through the tip of a 10 µm ID capillary, d) sampling through a side orifice inside a 10 µm ID capillary, and e) sampling through

a side orifice inside a capillary of 40 μm ID. For all three sampling scenarios sampling in the center of the pellet was modeled.

As already seen in the contour plots in Figure 4-2, diffusion and convection in the annular gap between the channel and the capillary lead to a slightly lower CO_2 concentration in the center of the catalyst pellet (6.8% instead of 7.0%). Furthermore, the CO_2 plateau in the center of the pellet is somewhat less pronounced in presence of the channel compared to the pristine pellet. If sampling is activated in the model, the convective fluxes in the gap increase. This can be seen by the simulated CO_2 profile extracted through a rather large 40 μm ID capillary (scenario e), for which the center CO_2 concentration drops even more from 7.0% to 5.9%. However, if the sample flow rate is just kept low enough - for example by using a capillary with an inner diameter of 10 μm (scenario d), the effect of sampling becomes so negligible that the concentration profile cannot be distinguished from the "without sampling" scenario (scenario b). In fact, the two profiles fall on top of each other. If the 10 μm ID capillary does not fill the entire channel because samples are extracted through the tip (scenario c), the fluxes are higher on the open side of the channel, and more educts enter from this side, resulting in lower CO_2 concentrations and a shift of the maximum concentration to the side where the capillary enters the pellet.

Since the sampling capillary is moving, the boundary conditions inside the gap will change. Therefore, simulations with sampling with the tip and the side orifice of the 10 μm ID capillary were conducted at different positions. The concentration directly at the sampling spot is shown in Figure 4-4 (squares for sampling with the tip, triangles for sampling with the side orifice), and compared to the capillary going through the whole channel without sampling (scenario b Figure 4-3). The previous results from sampling with the side orifice are confirmed: even by moving the capillary to different spots, the concentration is the same as without sampling. However, the drawback of sampling with the tip becomes obvious now. In contrast to the side orifice, the tip is taking the sample from the left side of the capillary - where the open side of the gap is - and not from the top, where the particle is situated (see Figure 3-3). Therefore, the measured product concentration will be lower than the one at the actual sampling spot, when the tip is directed towards lower concentrations of the product; which can be observed for $r<0$ in Figure 4-4. Conversely, for $r>0$, the tip is directed towards higher product concentrations than the ones present at the sampling spot, and consequently a higher CO_2 concentration will be measured.

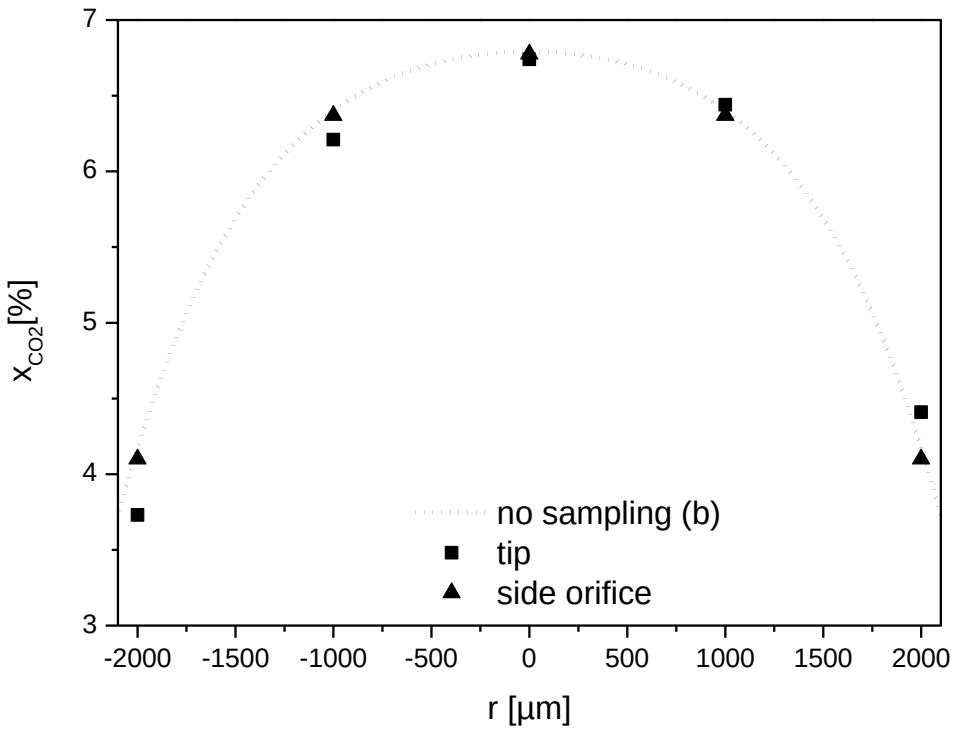

Figure 4-4: Simulated CO_2 fractions inside the cylindrical catalyst pellet. Capillary going through the whole channel without sampling (dotted line, scenario b), sampling through the tip of a 10 µm ID capillary at different positions (squares), and sampling through a side orifice inside a 10 µm ID capillary at different positions (triangles).

Two more potential scenarios have been studied in Figure 4-5. Sampling with the side orifice in a smaller annular gap (left side) and sampling with the side orifice in a particle without Knudsen diffusion (right side). On the left in Figure 4-5, the gap between the capillary and the particle has been decreased by increasing the OD of the capillary to 240 µm, resulting in an annular gap of 30 µm (scenario f), instead of 85 µm. It would have been in principle also possible to decrease the diameter of the hole inside the particle. The capillary was penetrating the whole particle, and sampling with a 10 µm ID capillary was simulated. The profiles for the pristine particle and the 85 µm gap are the same as in Figure 4-3, a, and d, respectively. As can be seen, data quality can be improved by decreasing the annular gap. Because less CO is diffusing through the gap, the CO_2 plateau becomes more pronounced than with the actual set-up (85 µm gap); however, the CO_2 fraction is still decreasing faster than in the pristine particle. Despite this phenomenon, the difference between the CO_2 fractions in the center of the particle becomes marginal.

On the right, in Figure 4-5 the results are shown when Knudsen diffusion was neglected. Due to increased diffusion coefficients inside the particle, the reaction rate becomes the limiting factor, and CO_2 is not plateauing in the center of the particle anymore. However, the diffusion coefficients inside the pellet are still lower than in the gas phase inside the gap, by a factor $\frac{\epsilon}{\tau}$. Thus, the CO_2 profile without Knudsen diffusion in the gap (scenario h) follows the same pathway as in the pristine particle (scenario g) but it is 0.1 mol-% less in the center of the particle. Such as in the simulations with Knudsen diffusion, the two profiles originating from the scenarios with (scenario i) and without sampling (scenario h) are identical, showing a negligible distortion from the sampling itself.

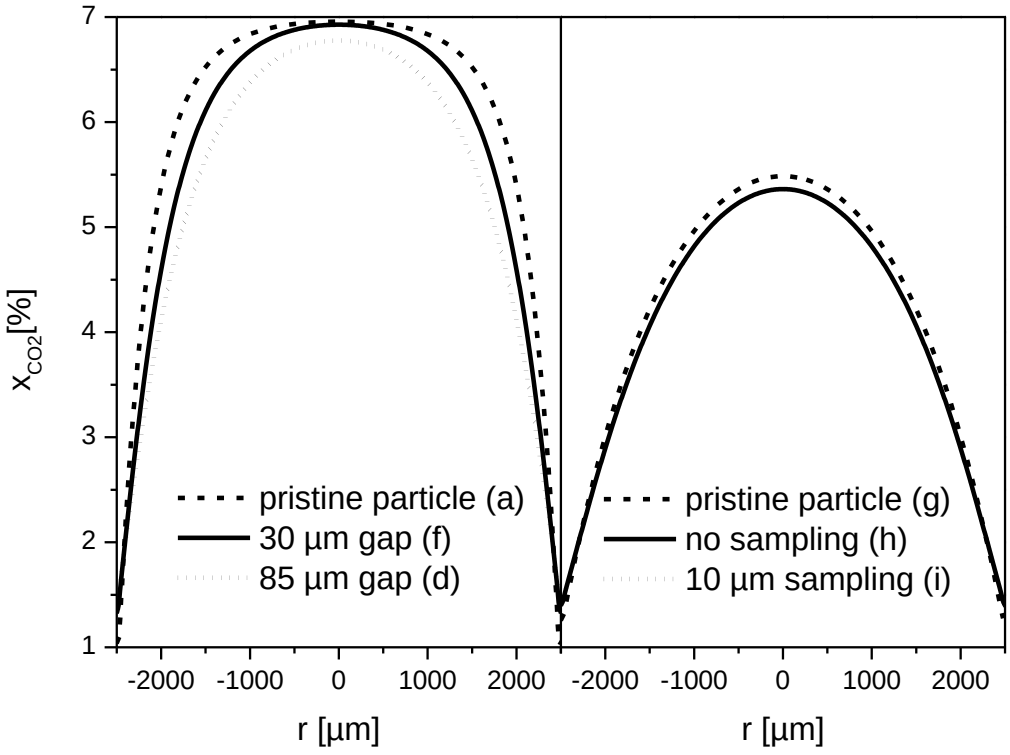

Figure 4-5: On the left: Simulated CO_2 fractions inside the cylindrical catalyst pellet for the pristine particle (scenario a) and sampling with the side orifice of a 10 µm ID capillary in two different sizes of the annular gap, 30 µm (f)and 85 µm (d), respectively. On the right: CO_2 fractions simulated without Knudsen diffusion for the pristine particle (g), capillary going through the whole channel without sampling (h) and sampling with the side orifice of a 10 µm ID capillary (i).

For a more quantitative comparison, the effectiveness factor η is considered which is defined as the ratio of the actual overall rate inside a catalyst and the reaction rate

that would result if the entire surface were exposed to the external surface concentration $c_{i,s}$ [36]:

$$\eta = \frac{\int_0^{V_P} R(c_i, T) dV_P}{R(c_{i,s}, T_s) V_P} = \frac{\tilde{R}}{R_s} \tag{4.2}$$

Two different effectiveness factors were calculated, η_P which is calculated for the particle, with the average reaction rate on the surface R_s and the volume average reaction rate $\tilde{R}$ inside the pellet (without the drilled channel and the capillary) and η_L which is based on the profiles shown in Figure 4-3 and Figure 4-5. In this case the reaction rate on the surface $R_{L,s}$ was evaluated based on the conditions at r=-2500µm, and for $\widetilde{R_L}$ the profile above the capillary was averaged based on the cylinder volume. However, this procedure neglects that species are diffusing into the particle via the top planar surface of the particle.

Table 4-2: Average reaction rates, surface reaction rates (s), and resulting effectiveness factors for the scenarios in Figure 3. Evaluated for the particle (P) and from the profiles in Figure 3 (L).

Scenario	$\tilde{R}$ [mol m^{-3} s^{-1}]	R_s [mol m^{-3} s^{-1}]	η_P [-]	$\widetilde{R_L}$ [mol m^{-3} s^{-1}]	$R_{L,s}$ [mol m^{-3} s^{-1}]	η_L [-]
a	4.6	15.0	0.31	3.9	15.4	0.26
b	4.7	15.2	0.31	6.6	14.5	0.45
c	4.7	15.2	0.31	6.9	14.4	0.48
d	4.7	15.2	0.31	6.6	14.4	0.46
e	5.1	16.9	0.30	10.3	16.9	0.61
f	4.7	15.2	0.31	5.6	14.9	0.38

By comparing $\tilde{R}$, only sampling with a 40 µm ID capillary (scenario e) is changing the conditions in the particle significantly. For all other scenarios, the conditions are similar. The picture changes, when looking at η_L for scenarios with the 10 µm ID capillary (scenario c, d). Based on the measured profile, η_L increases from 0.26 to 0.48 when measured with the tip (scenario c). However, data gained from this method will still be valuable. Catalyst particles can be optimized by comparing profiles from different particles to each other. As long as the same sampling method is used for all pellets, relative comparisons can be made and the effect of pore structure, active component distribution, or orientation to the flow on the pellet performance can be explored.

In combination with CFD simulations that include the gap also quantitative parameters such as the tortuosity or kinetics can be determined. Furthermore, the method can still be improved, for example by decreasing the gap between particle and capillary as scenario f shows. For particles, where Knudsen diffusion can be neglected, the profiles can be even evaluated directly as Table 4-3 shows. In this case, the difference in η_L between the pristine particle (scenario g) and sampling with a 130 μm OD and 10 μm ID capillary (scenario i) is as small as 3%.

Table 4-3: Average reaction rates, surface reaction rates (s) and resulting effectiveness factors for a pristine particle without Knudsen diffusion (g) and sampling with a 10 μm ID capillary (i)

Scenario	$\widetilde{R_L}$ [mol m^{-3} s^{-1}]	$R_{L,s}$ [mol m^{-3} s^{-1}]	η_L [-]
g	5.0	6.8	0.73
i	5.1	6.7	0.76

Overall, the numerical results displayed in this chapter indicate that the capillary sampling method disturbs the concentration profiles inside the pellet to some extent, because of convective and diffusional fluxes caused by the annular gap between the capillary and the channel wall, and by the sampling process itself; in fact, sampling with the side orifice shows less disturbance than sampling with the tip. Nevertheless, the disturbances are much smaller than initially forecasted, and they should in general not limit the practical applicability of the method to optimize industrial catalyst pellets. In most practical applications the disturbances will be somewhere between the ones shown in Figure 4-3 and Figure 4-5b. The pores of the simulated pellet in Figure 4-3 were rather small (average pore radius 47 Å) allowing for Knudsen diffusion, whereas if neglecting Knudsen diffusion, the pores need to be rather large (>50 nm). Industrial pellets possess often a bimodal pore distribution allowing for high diffusional fluxes through macro-sized transport pores, and reaction in micro-sized reaction pores accounting for high specific surface areas.

The invasiveness of the method can be further reduced by reducing the gap between capillary and particle - either using capillaries with bigger outer diameters or by drilling smaller holes into the particle. Furthermore, the technique can be optimized by using capillaries with smaller inner diameters and hence even smaller sampling flow rates. The final limits of the method will depend on the aspect ratio of the sampling channel that can be machined, the minimum possible diameter of the sampling capillary, and the sensitivity of the available analytical equipment.

5 Profile measurements

This chapter shows the results from the measurement with the spatial sampling capillary technique inside the catalyst pellet and in the boundary layer. In Chapter 5.1, the reproducibility of the results, the direction dependence of the measurements, and the resolution of the method are demonstrated. Chapter 5.2 shows an analysis of the external mass transfer for different Reynolds numbers and particle orientations to the flow by high resolution concentration profiles of the boundary layer. The interplay of mass and heat transfer, as well as kinetics that result in multiple steady states, is demonstrated in Chapter 5.3 presenting the effect on profiles inside and in the boundary of the catalyst pellet. Chapter 5.4 analyses temperature and concentration oscillations in the single pellet. In Chapter 5.5, improvements to the method by sampling with a side orifice and capillaries with smaller ID are shown.

5.1 Reliability

In the first series of experiments, profiles in and around the catalyst were measured for inlet temperatures of T_{in}=173 °C, 182 °C, and 191 °C with 3.2% oxygen and 5.4% carbon monoxide, at a Re of 5.7. Figure 5-1 shows the spatially resolved mole fraction profiles of CO_2 for these three temperatures (top), and a repetition of the experiment (bottom); the particle area is highlighted in grey. The measurements were conducted by sampling through the tip of a 10 μm ID capillary (Figure 4-3, scenario c). The profiles are slightly asymmetric due to the open channel to the left, as already predicted by the numerical simulations (Chapter 4.2). At an inlet temperature of 173 °C, the CO_2 mole fraction in the pellet center (r=0 μm) reaches 7.0% and then drops on either side, until it reaches zero outside the particle (r< -2500 μm, r> 2500 μm). The temperature inside the reactor, measured 2 mm above the particle, increased by 2 K. At 182 °C, the maximal CO_2 fraction is only 0.2% higher, showing a slightly broader plateau in the pellet center. The temperature 2 mm above the pellet

Parts of this chapter were published in B. Sosna, O. Korup, R. Horn, Probing local diffusion and reaction in a porous catalyst pellet, J. Catal. 381 (2020) 285–294. [107]

increased by 7 K. By increasing the inlet temperature further, the catalyst pellet ignites and changes its state from low conversion (reaction-limited) to high conversion (diffusion-limited), accompanied by a significant temperature rise. At an inlet temperature of 191 °C, the temperature measured 2 mm above the pellet increased by 46 K. The CO_2 fraction reaches a maximum of 6.8 mole % in the pellet center. The CO_2 mole fraction plateau stretches on the undisturbed right side up to a position of r=-2000 μm, and then decreases towards the outside of the particle (r=-2500μm). In this case only the outer shell (~500 μm) of the catalyst is used, which results in the low efficiency of the catalyst. In the ignited state, a boundary layer builds up around the catalyst pellet stretching more than 1000 μm into the bulk gas phase. At r=-3500 μm, the end of the scanned length, the CO_2 fraction has still not reached zero, indicating a pronounced film-diffusion limitation.

The sudden transition of a catalyst pellet from a low conversion state to a high conversion state (ignition) upon a small variation of an operating parameter is an example of bifurcation behavior, and it happens because the pellet was subjected to a range of parametric sensitivities. In the case of CO oxidation on Pt, the low-activity regime is caused by adsorbed CO on the platinum surface – namely, poisoning the surface [71,74]. In the high-activity regime, the surface is nearly free of CO and is either partially oxidized [71] or covered with chemisorbed oxygen [70]. This state is induced by high temperatures and low CO concentrations. Therefore, the ignition temperatures decrease with a decreasing $CO:O_2$ ratio [110].

To demonstrate the reproducibility of the measurements and the validity of the experimental setup, the measurement series has been repeated after the reactor was flushed with argon (Figure 5-1 bottom). For all three experiments of the second cycle, CO_2 fractions in the center were lower compared to the first run: nevertheless, the pathway of both curves is similar. The particle ignites at an inlet temperature of 195 °C instead of 191 °C the first time, but both experiments reach the same gas phase temperature of 246 °C inside the reactor. Hegedus et al. [67] could reproduce the ignition temperature within ±10 °C and observed a shift in the ignition to higher temperatures for catalysts that have been used more than once as well.

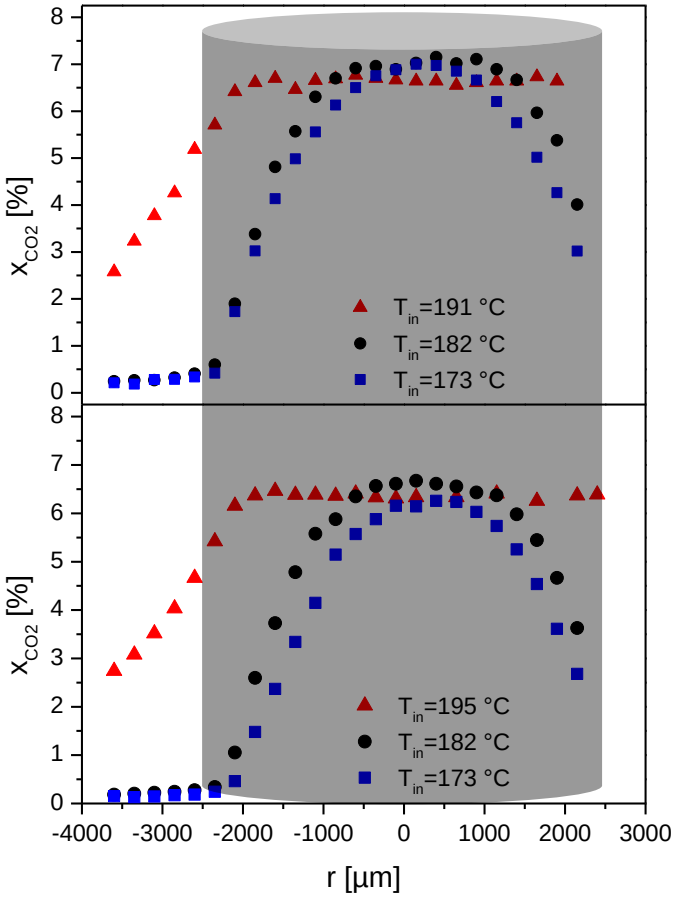

Figure 5-1: Spatially resolved mole fraction of CO_2 for T_{in}=173 (■), 182 (●) and 191 °C (▲) with 3.2% O_2 and 5.4% CO, measured with the tip of the capillary (top), (bottom) shows a repetition of the experiment. The grey area is representing the particle.

Furthermore, the direction dependence of the measurement was tested for a measurement with x_{CO}=5.6%, x_{O_2}=4.0% and an inlet temperature of 172 °C. In Figure 5-2, the capillary was moved from r=1350 µm to r=-4150 µm, and immediately afterward in a second run in the opposite direction. Overall, the results for all three species are in good agreement regardless of the direction. In the areas where the gradients are steep (between -1000 and -2500 µm), the CO_2 fractions of the measurement coming from the center of the particle, and thus from the higher CO_2 concentrations, showing higher values than the ones from the measurement of the other side. This is caused by two factors: firstly, the mass spectra are measured with an increment of 0.04, which leads to errors up to 0.45 mol-% of CO (see Chapter 3.5). Secondly, equilibrium in the QMS has not been reached, because the period between sampling points is too short for these steep gradients.

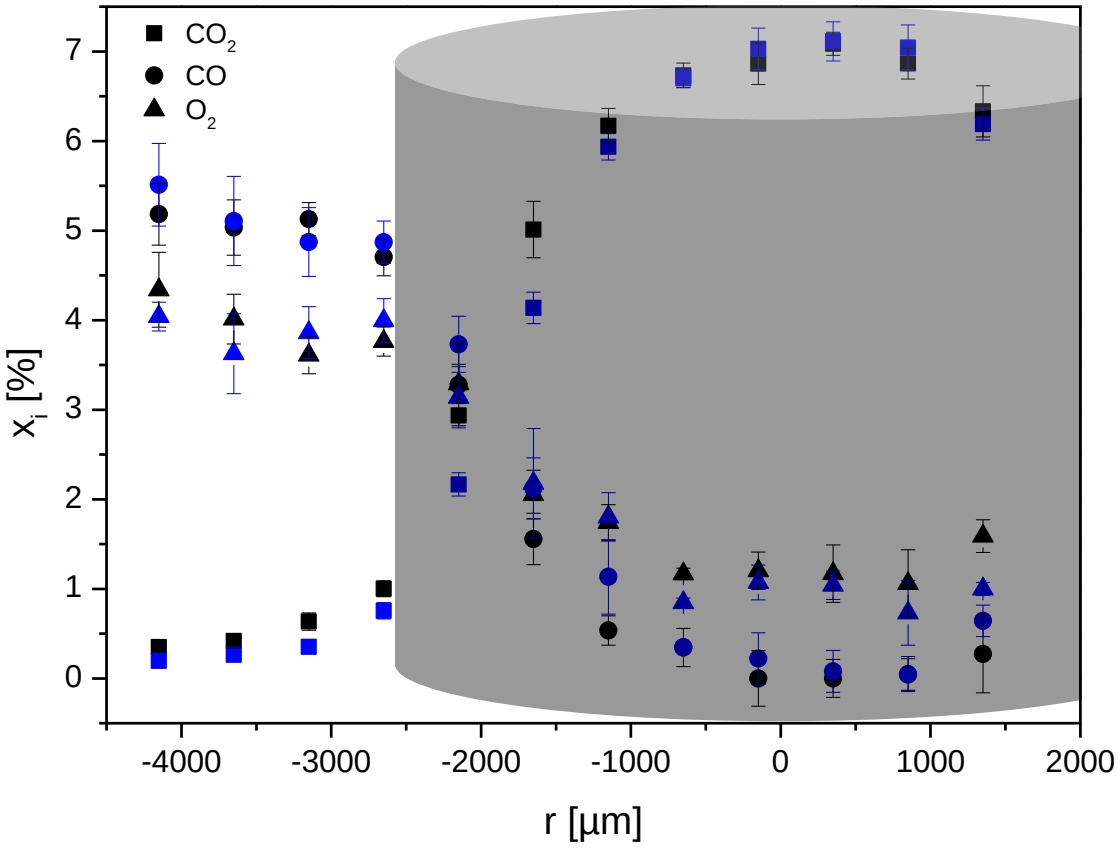

Figure 5-2: Profiles of CO_2, CO, and O_2 for T_{in}=172 °C, x_{CO}=5.6% and x_{O_2}=4.0%, measured from plus to minus (black) and minus to plus (blue). Error bars result from four measurements at every sampling point.

Indeed, measuring with a higher resolution or taking more time while sampling in areas of steep gradients will avoid this. In Figure 5-3 more data points were measured, and each measurement was repeated four times to demonstrate the spatial resolution and the reproducibility of the method. The data were measured for a Re of 20 and for a feed composition of x_{CO}=5.5% and x_{O_2}=4.7% in axial flow (cylinder turned by 90°). As can be seen, even steep gradients can be resolved with high spatial resolution. Close to the interface between the pellet surface and the gas phase, the points were measured with a step width as low as 10 µm. The higher uncertainties (represented in the error bars of Figure 5-3) of x_{CO} and x_{O_2} compared to x_{CO_2} originate from a non-constant background noise at m/z=28 amu and m/z=32 amu, in turn, caused by N_2 and O_2 in the background vacuum of the mass spectrometer (see Chapter 3.5). As a rule of thumb, the spatial resolution of the method is in the order of five times the diameter of the sampling orifice, so approximately 100 µm in the present experiments.

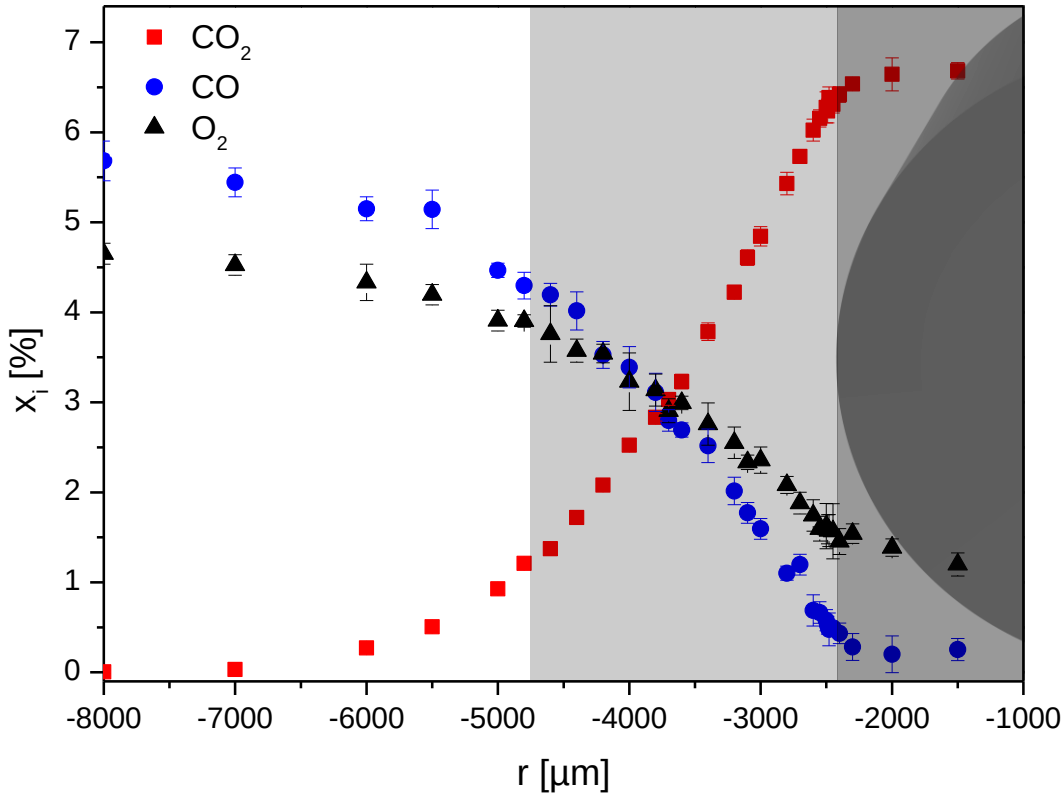

Figure 5-3: Mole fractions for Re=20, x_{CO}=5.5% and x_{O_2}=4.7%. At the interface between the gas phase and the catalyst pellet, data points have a resolution as close as 10 µm. Error bars result from four measurements at every sampling point. The light grey area is representing the boundary layer.

5.2 External mass transport

The external heat and mass transport around the catalyst are controlled by the flow conditions around it. As shown in Chapter 2.1.1 they are mainly controlled by the particle diameter and the velocity at given pressure and temperature.

The influence of the Re on the concentration profiles is shown in Figure 5-4. Both measurements were conducted in axial flow. They were carried out in the high-active regime, and external mass transfer is limited since a boundary layer around the particle built up. The CO_2-fractions within the whole boundary layer are higher for Re=3.9 compared to those for Re=20. For the CO fractions it is the opposite: as expected, they are decreasing sharper with a higher Re number. The bulk conditions (corresponds to the inlet conditions in this work) of CO and CO_2 are not reached at r=-7500 µm for the lower Reynolds number, whereas for Re=20 they are reached

at -7000 µm. In contrast, inside the cylinder (r >-2500 µm) both profiles behave very similarly; in both experiments, the particle temperature reached 281 °C. The boundary layer for Re=3.9 is about 350 µm thicker than the one for Re=20 (2650 µm compared to 2300 µm). It is experimentally determined by a method taken from Jess and Wasserscheid [111] which works as follows. Assuming the molar fraction of each species has been determined, a straight line was drawn through the first values in the boundary layer next to the particle. For good reliability, values in the first 400 µm were used in this work. The r value of the point of intersection of this line with the bulk concentration is the boundary layer thickness δ. Since x_{CO_2} values can be determined most reliably (see Chapter 5.1), they have been used to draw the straight line as shown in Figure 5-4 and Figure 5-5.

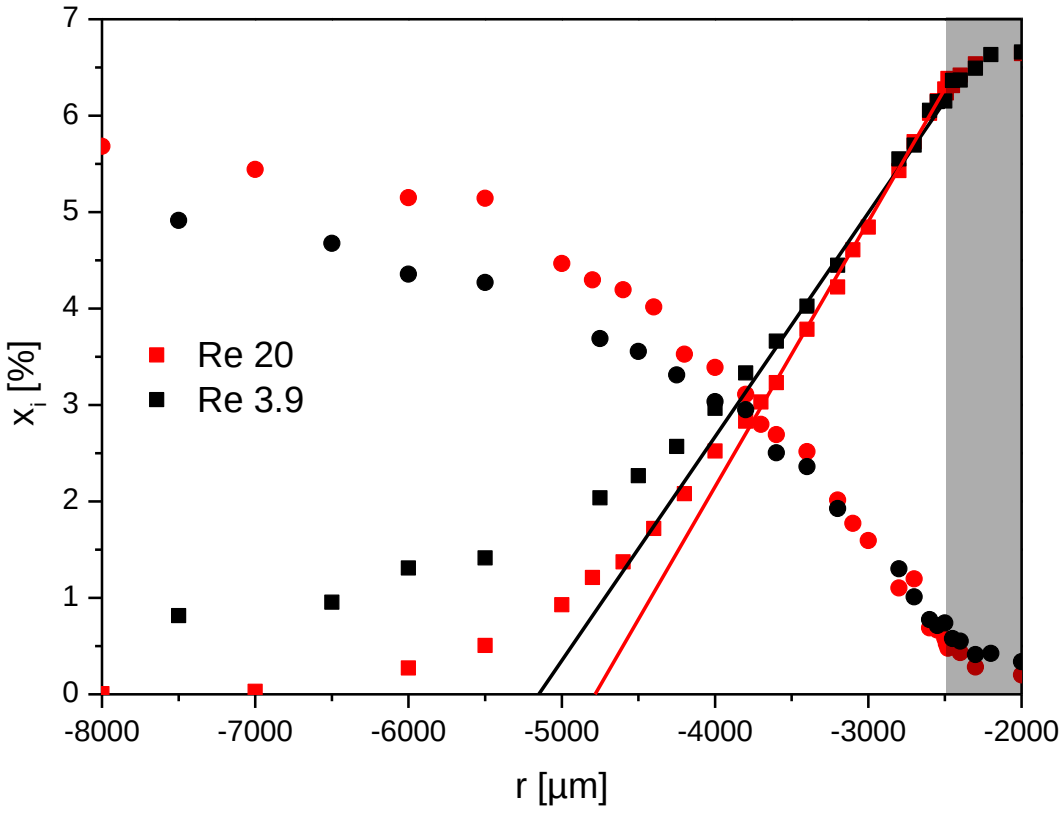

Figure 5-4: Comparison of the CO_2 (■) and CO (●) molar fractions with a cylinder in axial flow for experiments with T_{in}=173 °C, x_{CO}=5.5%, and x_{O_2}=4.7%, black symbols are measured with Re=3.9, red ones with Re=20. The interceptions of the straight lines with the x-axis represent the thickness of the boundary layer δ for Re=20 (red) and Re=3.9 (black).

The influence of the particle orientation to the flow on δ is shown in Figure 5-5. Both experiments were conducted with identical conditions: Re=20, T_{in}=173 °C, x_{CO}=5.5% and x_{O_2}=4.7%, except for inclination angle; one experiment was conducted in cross

flow, the other in axial flow. Since Re is given for the volume equivalent sphere diameter, which is common for correlations in packed beds, it is the same for both experiments and would result in the same values of δ. However, it can be observed that the CO_2 fractions in axial flow are higher within the whole boundary layer compared to the cross flow, and consequently are plateauing faster inside the cylinder. The beginning of the particle (r=-2500 µm) has been used as a reference point; so far this could be only detected by eye, with a mirror. For this reason, it is assumed that the reference point can only be determined with an accuracy of ±75 µm. Nevertheless, a significant difference in the boundary layer between both experiments is visible (about 650 µm). Furthermore, the particle temperature measured in axial flow was 23 K higher than the one in cross flow (281 °C compared to 258 °C). These results agree with previously reported observations [112–114]. An increasing heat transport was measured for cylinders with an increasing inclination angle, where 90° corresponds to cross flow, 0° to axial flow. Due to the analogy of heat and mass transport, the same behavior is expected for mass transport. For a cylinder with an l to d ratio smaller than four, the heat transport was maximal at an angle between 40° and 50° as reported by Oosthuizen and Mansingh [112]. Still, the heat transport for this particle was more effective in cross than in axial flow, which the results in Figure 5-5 show. The dependency on the inclination angle has not been further investigated in this work but could be further investigated with the presented set-up. In Table 5-1 the experimentally determined δ, and resulting values for k_c for different Re are listed.

Table 5-1: Experimentally determined and calculated values for k_{cCO_2} and δ from Equation 2.5 for different Re and orientations to the flow.

Re		3.9	5.8	5.8	20	20	35
Orientation		axial	axial	cross	axial	cross	cross
δ	[µm]	2650	2400	2000	2300	1650	1450
δ_{calc}	[µm]	5561	4536	3999	2439	2161	1638
k_{cCO_2}	[m s^{-1}]	0.0096	0.0106	0.0128	0.0112	0.0155	0.0174
$k_{cCO_2,calc}$	[m s^{-1}]	0.0046	0.0056	0.0064	0.0105	0.0118	0.0156

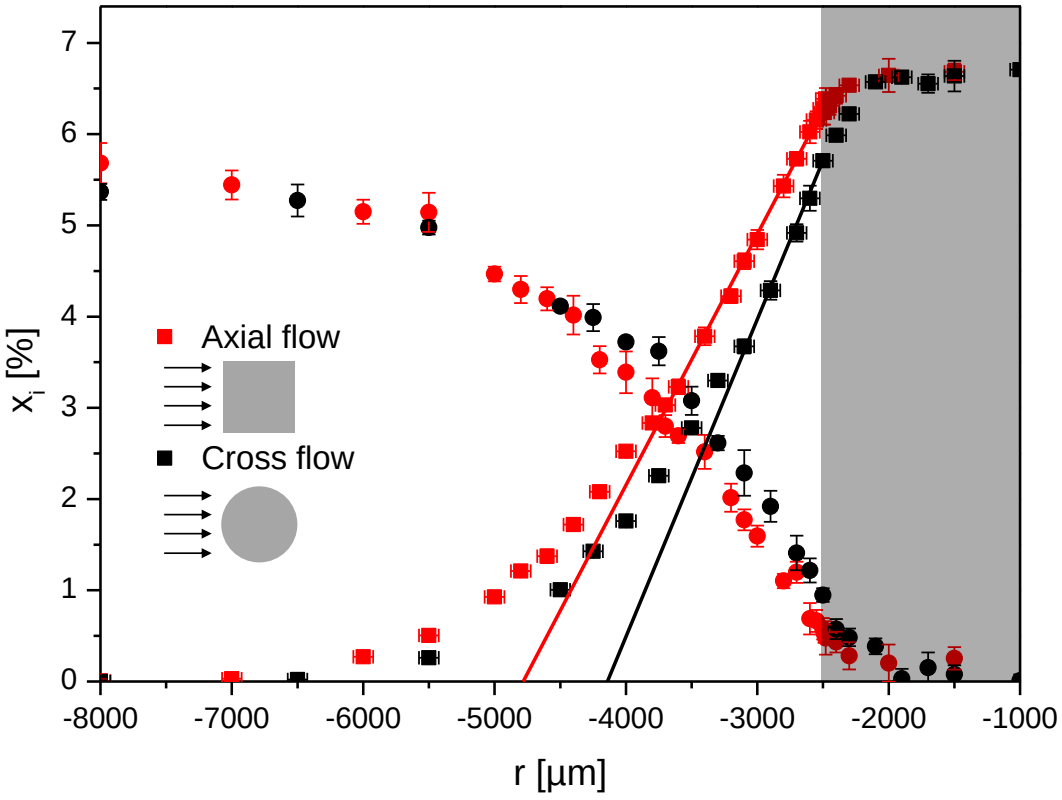

Figure 5-5: Comparison of the CO_2 (■) and CO (●) molar fractions for experiments with Re=20, T_{in}=173, x_{CO}=5.5% and x_{O_2}=4.7%, black symbols are measured for the cylinder in cross flow, red ones in axial flow.

The previously mentioned trends could be confirmed: within the axial and cross flow measurements, the boundary layer is decreasing with increasing Re. Furthermore, the boundary layer in cross flow is thinner, and in turn, the mass transport is better, than in axial flow for the same Re. CFD simulations of the flow around the cylinder confirm this - as can be seen in Figure 5-6: it shows higher flow velocities on the side of the cylinder for Re=20 in cross than in axial flow, and therefore a thinner boundary layer. The profiles depicted are on the side were concentration profiles were measured with the tip of the capillary, 65 µm above it. Furthermore, the figure highlights how the tip is disturbing the unwanted flow but an unavoidable side effect. With the tip at r=-3000 µm, the velocity for both cross and axial flow is decreasing compared to the flow around the cylinder with the tip inside the particle. Even considering this, the velocities in cross flow are still higher.

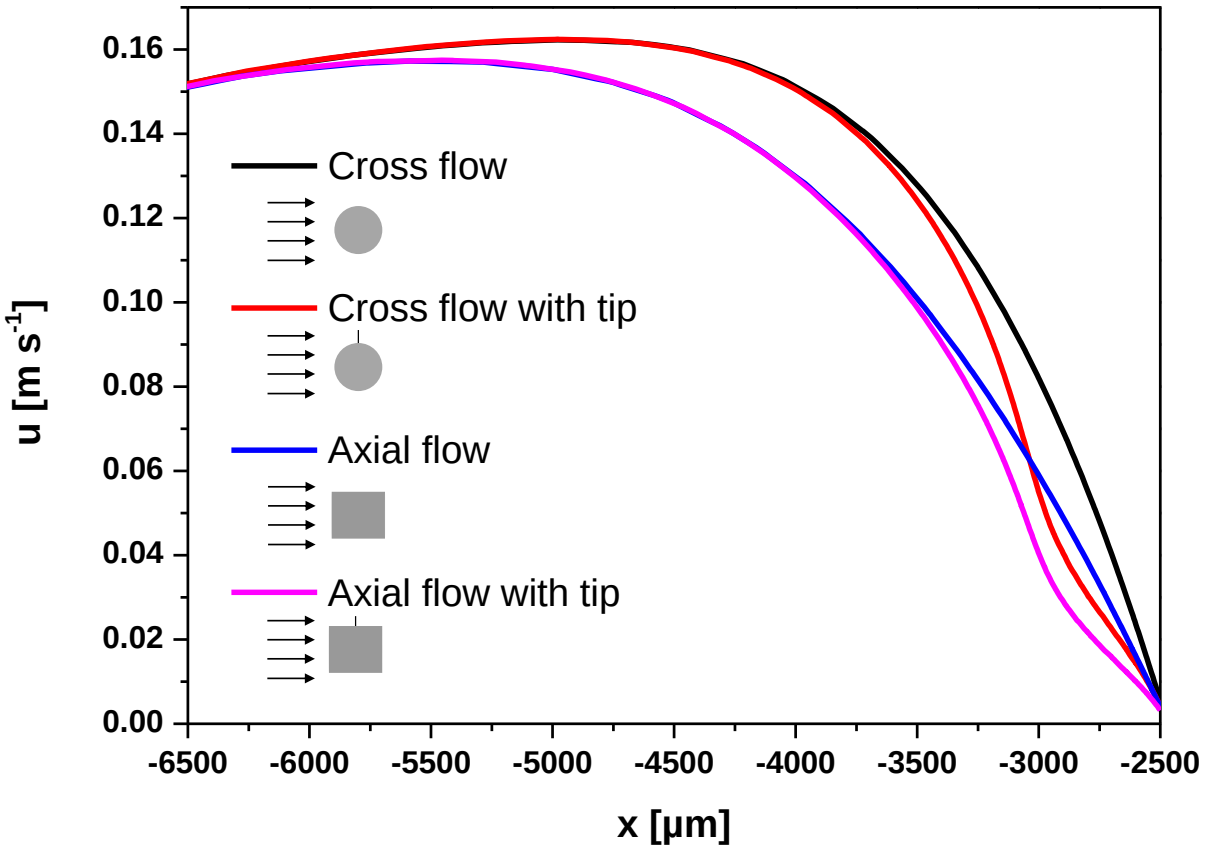

Figure 5-6: Simulated velocity profiles at 90° from the particle, 65 µm above the capillary, for the cylinder in cross flow (black), cross flow with the capillary at r=-3000 µm (red), axial flow (pink), and axial flow with the capillary tip at r=-3000 µm (blue).

Values for k_c and δ are calculated with the correlations from Chapter 2.1.1. The parameters used for the calculations can be found in the appendix (A Parameter). To account for the different possible orientations of the particle, the characteristic length for cross flow is taken as $d\pi/2$ and $d + d$ for axial flow, respectively. The characteristic length is represented by the length over which the fluid flows and is shown in Figure 5-7 for both cases [115].

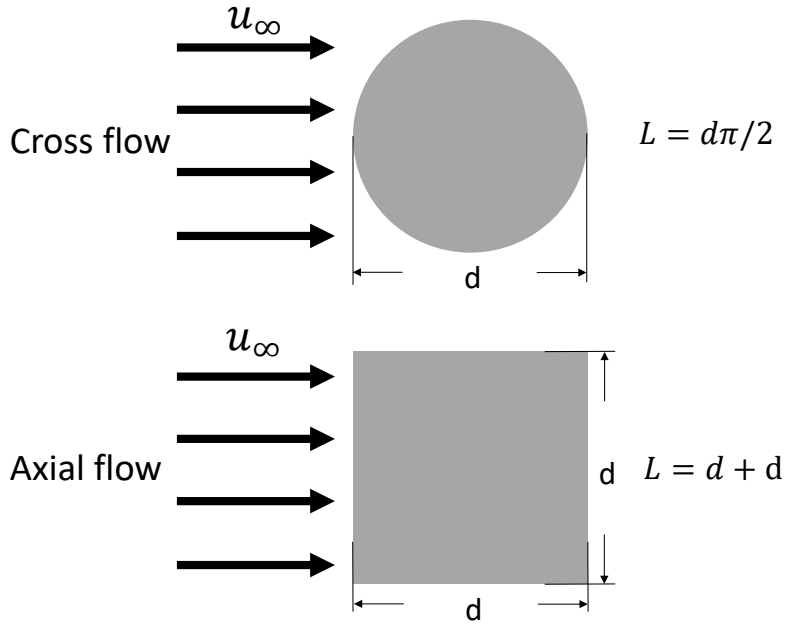

Figure 5-7: Characteristic length for an equilateral cylinder in cross flow (top) and axial flow (bottom).

For Re=20 and Re=35, there is a good agreement between the calculated values from CFD and the experimentally determined ones, both for axial and cross flow; however, the experimentally determined values are lower than the calculated ones. For Re=3.9 and Re=5.8, the experimental δ is about half the calculated one, resulting in k_c being twice as high. An explanation of the lower experimentally determined values compared to the calculated ones can be found in Figure 5-6. At r=-5000 µm, which equals to δ=2500 µm, the velocity starts to decrease again because of the no-slip boundary condition at the wall. This causes a higher maximal velocity between the wall and the cylinder compared to a cylinder in free flow, for which the correlations were determined. In CFD simulations, Mirhashemi et al. [116] determined a flow domain of 10-15 times the particle diameter to neglect wall effects. In this work, this ratio is four, confirming their findings. Moreover, the accuracy of the method used to determine the boundary layer experimentally might not be high enough. In Figure 5-4, the boundary layer for Re=3.9 seems to be thicker than the determined one of 2650 µm, since the bulk concentration of CO_2 has not been reached, even at a thickness of 5000 µm. Furthermore, it must be considered that the concentrations measured with the tip are lower than the actual concentrations in the boundary layer, as shown in Chapter 4.2. This, as a result, reduces the

experimentally-determined δ. Overall, measurements with the side orifice could improve the quality of the data.

5.3 Hysteresis

In catalyst pellets, the transition between the low- and the high-active regime happens suddenly by small changes in the boundary conditions (velocity, temperature, concentration), as described in Chapter 5.1. However, the transition back occurs at different conditions, resulting in a hysteresis, which can be seen in Figure 5-8. The figure shows the hysteresis of the particle temperature for educt concentrations of 3.2% O_2 and 5.4% CO, in dependence of the inlet temperature. In this experiment, the temperature of the particle and the temperature of the wall were measured; the latter was used for temperature control. The measurement was conducted at an early point of this study when the optical access caused heat losses, which was solved later on by also placing insulation material on it. This explains why the temperature above the particle on the low temperature branch is lower than the inlet temperature. The inlet temperature was slowly increased until the particle ignited. By decreasing the inlet temperature again, the catalyst pellet stayed in the ignited state for temperatures lower than the ignition temperature, until it extinguished and fell on the lower branch. Heating the pellet again, it stayed on the lower branch until its ignition temperature was reached. This phenomenon was observed also by previous authors [67,74].

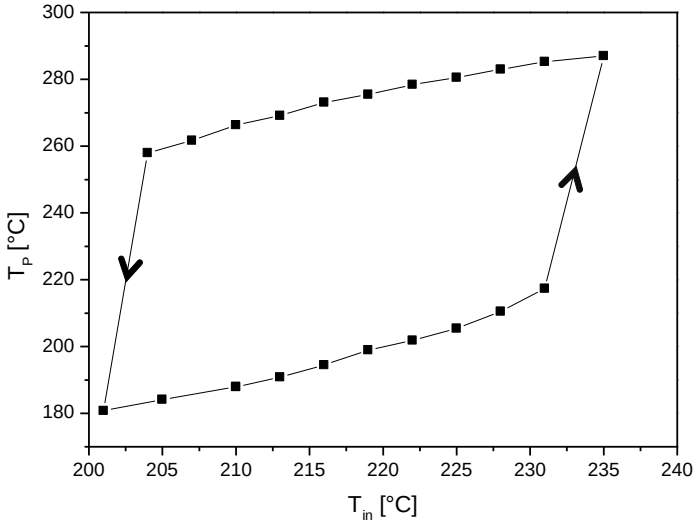

Figure 5-8: Temperature of the particle T_P for increasing (lower branch) and decreasing (upper branch) the inlet temperature T_{in} for x_{CO}=5.4% and x_{O_2}=3.2%.

The same behavior was observed with increasing O_2 concentration. Figure 5-9 shows on the right-hand side the resulting hysteresis of the temperature measured inside the pellet (T_P), by increasing/decreasing the O_2 concentration. On the left-hand side, the mole fractions for CO, O_2, and CO_2 are shown for the same conditions, but the upper one was in the ignited state and the lower one in the extinguished state. In the high-active state, a boundary layer of about 3.5 mm formed around the catalyst pellet, resulting in a surface concentration of about 6% CO_2, whereas in the low-active state the boundary layer was only 1 mm thick, and the CO_2 concentration on the surface was only 1%. Previous authors (e.g. [74,117]) showed that the hysteresis decreases with lower CO concentration, lower inlet temperature and/or smaller particle sizes.

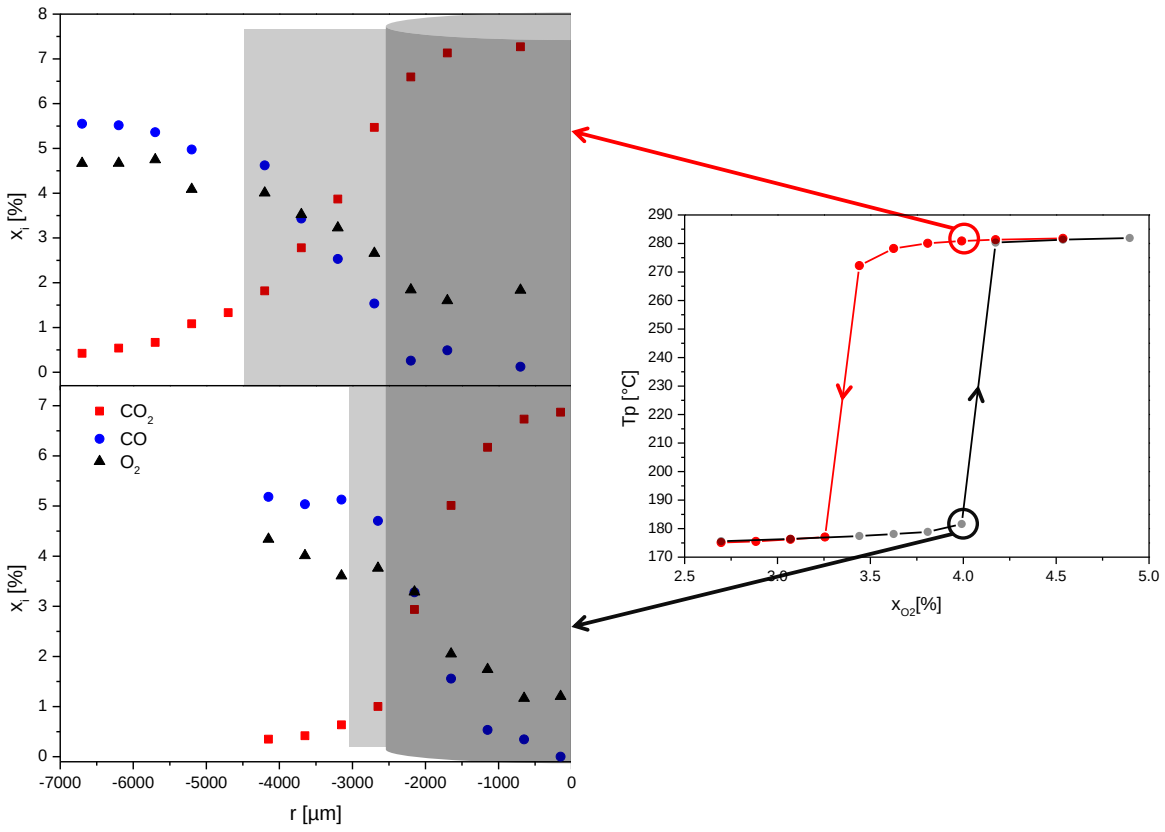

Figure 5-9: Particle temperature for different O_2 fractions with T_{in}=173°C and x_{CO}=5.4% by increasing (black) and decreasing the latter (red) (right-hand side). Spatial profiles of CO_2, CO, and O_2 for the same inlet conditions (left-hand side), the upper one in the diffusion limited state, the lower one in the reaction limited state. The light grey area is representing the boundary layer.

The conditions in the experiments were tested using the criteria for multiple steady states from Chapter 2.1.2. The CO poisoning of the Pt surface causes a negative

reaction order. Therefore, for certain conditions, the reaction rate increases with decreasing CO concentration. This might result in effectiveness factors greater than one, and consequently in multiple steady states. The criterion from Luss (Equation 2.22 and 2.23) for multiplicity requires that the CO concentration inside the particle becomes less than half of the concentration on the surface, for a reaction of minus first order. A look at the results presented in Figure 5-9 confirms this assumption for both shown profiles.

Moreover, the profiles show external mass transfer limitations. Therefore, criterion 2.27 holds, since the reaction is assumed to be of minus first order and because of internal diffusion limitations $\eta \neq 1$. The results can be found in Table 5-2. Since a wide range of activation energies was available in literature, calculations were performed for a maximum value of 100 kJ mol^{-1} and a minimal of 45 kJ mol^{-1}. As temperature boundaries for bulk temperature, 170 °C, and 300 °C were selected. For 170 °C and 100 kJ mol^{-1}, respectively, multiplicities are possible, whereas for 300 °C and 45 kJ mol^{-1} they are not anymore. However, for 240 °C (which was the maximal inlet temperature in Figure 5-8), multiple steady states are possible again according to the criterion. Finally, the criterion for an adiabatic particle without external limitations was verified (Equation 2.20). According to this criterion, no multiplicities are possible for all combinations, as can be seen in Table 5-2. In the future, obtaining a temperature profile through the pellet will help to further confirm this criterion, by observing if the temperature rise inside the catalyst pellet of less than 2%, predicted by the Prater number, is verified. All parameters used for the calculations can be found in the appendix (A Parameter).

Table 5-2: Uniqueness criteria for the boundary layer and an adiabatic particle at different temperatures and activation energies. For the green boxes, the criterion predicts possible multiplicities whereas for the red boxes none are predicted.

T	EA	Boundary layer $n \leq 1, \eta \neq 1$		Adiabatic particle	
[°C]	[kJ mol-1]	$(\beta_B\gamma + 1 - n)^2$	$8\beta_B\gamma(1+\beta_B)$	$4(1+\beta)$	$\beta\gamma$
300	45	194	216	4.04	0.10
300	100	814	481	4.04	0.22
170	45	484	422	4.06	0.18
170	100	2159	938	4.06	0.40

This evaluation shows that the right criterion needs to be chosen to scan for multiplicities. The criteria are based on different assumptions, and therefore it needs

to be proven if these assumptions hold in the investigated reaction system. Furthermore, they can give an indication at which conditions multiplicities are possible, however, not all combinations of parameters for which the criterion holds will result in multiplicities.

5.4 Oscillations

A typical phenomenon observed during the CO oxidation on alumina supported platinum catalyst pellets are concentration and/or temperature oscillations [74,79]. As observed by previous authors, by keeping the O_2 concentration constant, the particle ignites in this work with decreasing CO concentration [67,74]. A critical factor for oscillations is the CO:O_2 ratio, in literature, oscillations were observed below 1.7 [118]. In this study, oscillations were observed with a CO:O_2 ratio of less than one. Figure 5-10 shows an example of T_p at around 162 °C and different CO:O_2 ratios. By feeding only CO_2 and argon into the reactor, the temperature of the catalyst pellet is very stable, with fluctuations in the order of 0.1 °C - caused by the temperature control. In reaction regimes without oscillations, the temperature control reaches the same stability. With a CO:O_2 ratio of 0.47, irregular temperature oscillations were measured. By decreasing the ratio further, oscillations became regular, with an amplitude of around 2 K and a frequency of 2.5 min^{-1}. Temperatures, after changing the CO concentration and waiting for the steady state, have been cut out from Figure 5-10 for clarity. In good agreement with Beusch et al. [35], who also measured oscillations on a single catalyst particle, the frequencies were increasing with increasing temperature (see Table 5-3, from f to a) and maximal amplitude of two Kelvin was detected. Furthermore, the amplitudes decreased with increasing CO concentration, by keeping the CO:O_2 ratio constant (a-c). At higher frequencies, external and internal heat and mass transport might be limiting, and therefore amplitudes are decreasing.

The graph at the bottom in Figure 5-10 shows the corresponding CO_2 signal (m/z=44 amu), corrected for background noise and measured at circa 500 μm inside the particle. Without reaction, the signal oscillates irregularly. In regions with oscillating temperature, the CO_2 signal becomes more synchronized, oscillating rather regularly, and with a similar frequency as the pellet temperature. The absolute difference in the molar fraction of CO_2 between the maximal and minimal intensity is about

0.1 mol-%. Even though it is expected that the slow diffusional processes around the particle (i.e. Knudsen diffusion, film diffusion) are reducing the amplitude, the main cause for this behavior is most likely the sampling system. The equilibrium in the vacuum chamber for each sampling point is obtained after two minutes. Consequently, with this technique, the real maximal and minimal concentrations will not be measured.

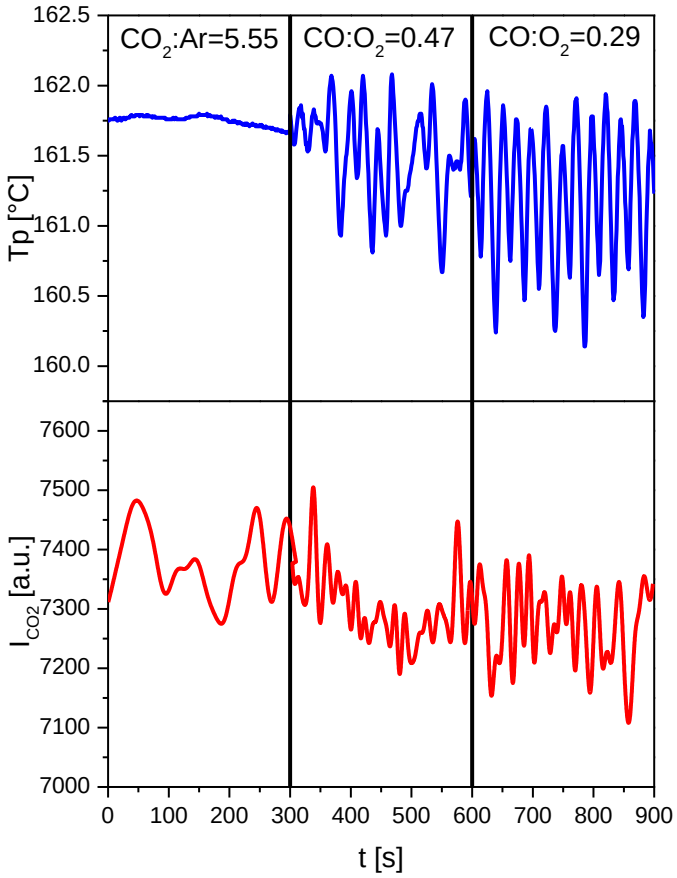

Figure 5-10: Particle temperature profiles (top) and the corresponding CO_2 signal at m/z=44 (bottom) for *Re*=5.7; without reaction (left), 3.4% O_2 and 1.6% CO (middle), as well as 3.4% O_2 and 1% CO (right).

There is consensus in literature that these oscillations occur when the catalyst changes periodically from a high-active to a low-active surface structure [38,39,79]. However, a complete change of the particle between the ignited and extinguished state (see Chapter 5.2) has not been observed: in case b (Table 5-3), for example, the oscillations happened in the extinguished state, since the particle ignited by increasing the O_2 concentration, resulting in a particle temperature of 205 °C. The

amplitude was 1.8 K, which is less than 15 % of the temperature rise in the completely ignited state.

Table 5-3: Amplitudes and frequencies of oscillations for five different cases, in descending order (from a to f) of the average particle temperature T_P.

		a	b	c	d	e	f
x_{CO}	[%]	2.34	2.04	1.85	1.87	1.03	1.43
$CO:O_2$	[-]	0.78	0.78	0.76	0.54	0.30	0.42
T_{heat}	[°C]	190	190	190	175	165	165
$T_{P,av}$	[°C]	200.3	193.3	190.0	176.0	161.2	161.6
Amplitude	[°C]	0.5	1.2	1.8	1.6	1.9	1.5
Frequency	[1/min]	12.5	6.5	5.5	4.2	2.4	2.3

At atmospheric pressure and low partial pressures of CO (<20 mbar), Vendelbo et al. [39] reported that the oscillations are synchronous, with a periodic re-faceting of Pt nanoparticles. For partial pressures p_{CO}>1 mbar, the particles had a more spherical shape, whereas for p_{CO}<1 mbar they had a more faceted shape. This is in accordance with Yoshida et al. [119], who observed the same behavior: at room temperatures, where more CO molecules adsorb on the surface, the particle had a more spherical shape; whereas at elevated temperatures (200 °C), where CO desorption increases, they had a more faceted shape.

Vendelbo et al. [39] found conditions in which the spherical shape is more active than the faceted, which explains the oscillations. If an oscillation cycle starts in the low-active regime (R is small), when the CO pressures just increased (A, Figure 5-11), the particle will approach a more rounded shape (A→B). At point B the round shape is in equilibrium, and the particle switches to the high-active regime (C); therefore, the CO concentration decreases. Next, a faceted shape builds up (C→D). At point D, the faceted shape is in equilibrium, the particle switches to the low-active regime, the CO concentration will increase again (A), and one cycle is completed. Vendelbo et al. did not observe any oxides on the surface at 573 K [39]. Similar structural changes have been observed by Ertl et al. [75] on clean Pt(100) single crystals under UHV conditions. This surface is stable (and less active) in a pseudo-hexagonal structure (resembling Pt(111)). With CO adsorbed, on the other hand, it changes into its unreconstructed structure and becomes more active, because O_2 adsorbs significantly better on this structure. In this work, partial CO pressures of less than 1 mbar close to the surface could only be reached in the ignited state. In the extinguished state these low concentrations, if at all, are only present in the center of the particle (e.g. Figure

5-9). This leads to the question whether the oscillations originated in the extinguished state emanate only from the center of the particle, or if other conditions exist at which the spherical shape is more active than the faceted one.

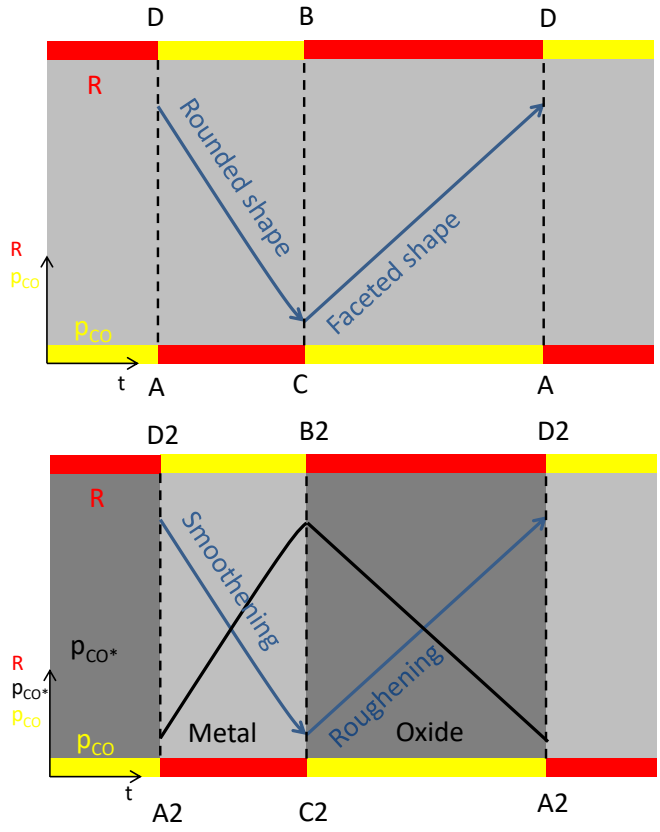

Figure 5-11: Oscillation mechanisms from Vendelbo at al.[39] (top) and Hendriksen [38] (bottom). The red bars representing the speed of reaction R and the yellow bars the partial pressure of CO in the gas phase (p_{CO}). Adapted from [38].

Oscillations at higher CO concentrations and atmospheric pressure, similar to this work, have been reported as well in literature [38,61,79,120]. At these conditions, a change of an active oxide surface and a low active CO surface have been observed. However, these structures are changing in activity. If an oscillation cycle starts in the low-active regime when the CO pressures just increased (A2, Figure 5-11), the particle is in a rough metal state, hence more CO will adsorb, and the surface will become smoother (A2→B2). At some point, the smooth surface becomes more stable in the oxide state, the reaction rate increases, and the CO concentration drops (C2). The metal oxide surface starts to roughen (C2→D2) until it becomes more stable in the metal state, and the reaction rate will drop again (A2) [38]. This model predicts the observed increase in frequency with increasing temperature [78] and is therefore in good agreement with our data. However, the mechanism was observed on Pd and

not on Pt. Therefore verification of this mechanism on Pt, e.g. with the operando X-ray diffraction method from Hendriksen [38], is necessary to validate the theory.

Overall, it can only be concluded that CO:O_2 ratio and temperature are critical values for the oscillations and that these surface changes occur only with oxygen in stoichiometric excess. If too much CO is adsorbed (CO concentration is too high), the surface will be poisoned, and at high temperatures, the reaction becomes too fast, and the catalyst cannot oscillate between the high- and the low-active state.

The oscillation on a porous catalyst pellet in a non-isothermal reactor is a complicated phenomenon. Heat and mass transfer effects around and inside the pellet are interplaying with surface phenomena - such as the re-faceting or oxidation/reduction of the Pt surface due to the adsorption of CO and O_2. The concentration and temperature measurements performed in this work provide a promising insight. In the future, spatial temperature profiles coupled with spatial concentration profiles should provide a deeper understanding of the oscillations processes in and around a catalyst pellet.

5.5 Profile measurements – Optimizations

To decrease the diffusive fluxes inside the sampling channel, and to avoid asymmetric boundaries around the particle by sampling with the tip, sampling with a side orifice in the wall of the capillary was tested, at an inlet temperature of T_{in}=170 °C and for a feed containing 3.2% O_2 and 5.4% CO. The mole fractions of CO_2 and O_2 are displayed as red symbols in Figure 5-12. The blue profiles were measured under the same conditions, with the tip of a 5 μm capillary to reduce the sample flow and hence the invasiveness of the method. The sampling volume flow will be reduced to 1/16 compared to the 10 μm ID capillary, according to Equation 3.1.

The CO_2 profile measured with the side orifice is symmetric, whereas the profile measured with the tip looks slightly shifted: it is increasing slower from -2500 μm to 0 than from 0 to 2500 μm. This confirms the simulations from Chapter 4 (Figure 4-4), where the CO_2 is slightly shifted because of the higher diffusivity of the educts. However, the sampling technique itself is not the only cause of the reduced CO_2 concentration: the measurement with the 5 μm capillary was performed a few days after the side orifice measurement, resulting in reduced activity of the catalyst,

accounting for the lower CO_2 concentration in the center of the pellet. The O_2 profiles in both measurements are fluctuating, particularly the one performed with the 5 µm ID capillary. This is caused by small changes in the O_2 background signal. The sampling flow rate extracted with the 5 µm ID capillary is so low that the O_2 background signal increased from 10% to 30% of the argon signal, making the O_2 signal more sensitive to background fluctuations. Overall, the data show that sampling with the side orifice results in a higher quality of measurements, as already stated before.

Tests with a 2 µm capillary showed that the detection of CO_2 is still possible (see Chapter 3.5), at the cost of an increase of the sampling time. However, the procedure will need to be optimized to get reliable results. Nowadays, capillaries with an ID as small as 100 nm are commercially available. Nevertheless, tests with a 300 nm ID capillary (Polymicro Technologies, Phoenix, USA) showed that the verification of species is possible, but the MBMS used in this work is not sensitive enough for any quantification.

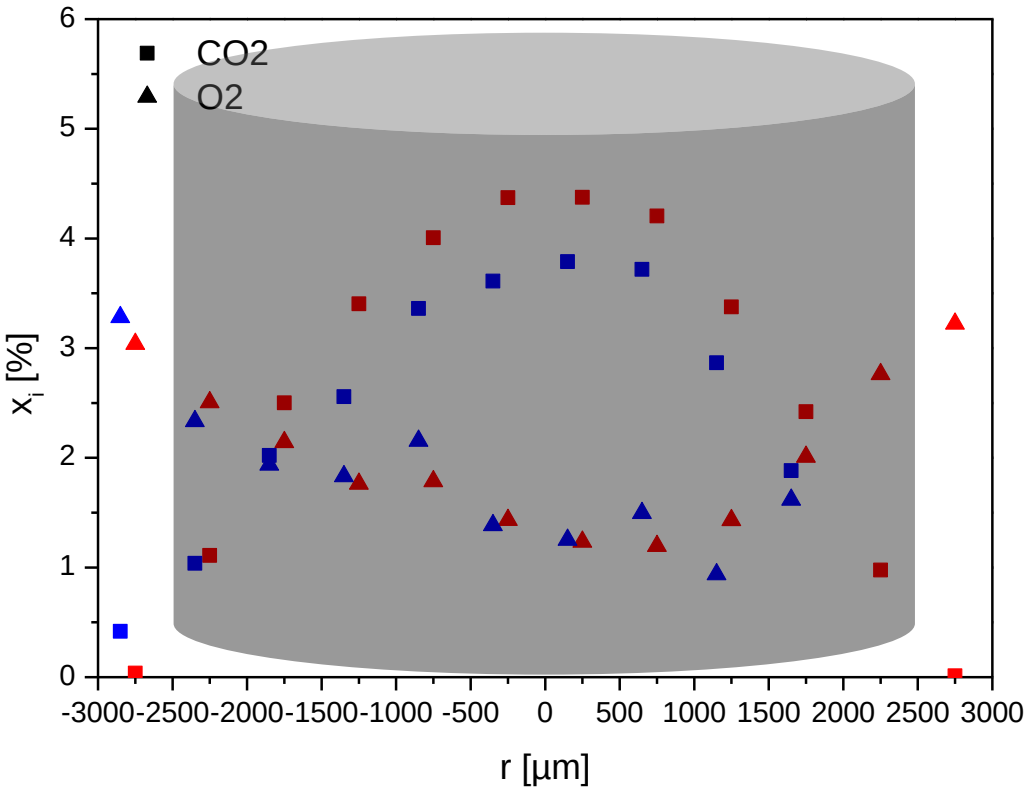

Figure 5-12: Spatially resolved mole fraction of CO_2 (■) and O_2 (●) with 3.2% O_2, 5.4% CO and T_{in}=170 °C, measured with the side orifice (red) and the tip of a 5 µm ID capillary (blue).

6 Temperature and concentration measurements by Raman spectroscopy

The concentration profiles measured with the capillary already give some information about the boundary layer forming around the particle. However, the measurements are bounded to the channel through the catalyst pellet and can only be acquired on one straight line in the reactor. More information about the gas phase would be useful to investigate the processes around the particle (e.g. film diffusion) in greater detail. Raman spectroscopy offers the possibility of measuring temperature and/or concentration from rotational and vibrational bands. Coupled with a confocal microscope, volumetric resolutions of a few μm^3 are reachable theoretically [103]. Nevertheless, the Raman scattering has an inherently low sensitivity due to the small Raman scattering cross-sections as compared to IR absorption coefficients. Furthermore, low reactant concentrations in the gas phase compared to the liquid or solid ones, and the low laser power that can be applied in the set-up decrease the signal even more. Quantitative Raman spectroscopy is already challenging because of the inherently unknown Raman-scattering cross-sections and the need for a precisely determined instrumentation function [121]. Therefore, this chapter shows some pilot experiments and explores the feasibility of using Raman microscopy to determine spatial temperature and concentration profiles in the gas phase of our reactor. Chapter 6.1 concentrates on the feasibility of measuring vibrational bands, whereas Chapter 6.2 concentrates on the rotational bands. The reliability of the calibrations is demonstrated (6.2.1), spatial temperature measurements in the reactor are shown (6.2.2), and the future perspective of measuring temperature and concentration profiles with rotational bands in multicomponent mixtures is outlined.

6.1 Vibrational Raman spectroscopy

Inside the reactor, no Anti-Stokes vibrational bands were detected by measuring at 175 °C and at an integration time of 60 minutes. Moreover, no upper vibrational Q-branches ($1 \rightarrow 2$, $2 \rightarrow 3$) were observed at the N_2 shift of 2330.7 cm^{-1}. According to Equation 2.64, the ratios of the number of molecules in $v = 1$ to that in $v = 0$ for O_2 and N_2 at three different temperatures were calculated, and are shown in Table 6-1 [93]. For all temperatures, the ratio is lower than the signal-to-noise ratio of the measurements, and therefore cannot be reliably detected.

Table 6-1: Ratio of the number of molecules in $v = 1$ to that in $v = 0$ for 300 K, 500 K and 1000 K.

Gas	$\Delta G_{v+1/2}$	$e^{-\Delta G_{v+1/2} hc/kT}$		
	[cm^{-1}]	For 300 K	For 500 K	For 1000 K
N_2	2330.7	1.4E-05	1.2E-03	3.5E-02
O_2	1556.4	5.7E-04	1.1E-02	1.1E-01

6.2 Rotational Raman spectroscopy

6.2.1 Calibration

In Figure 6-1, a rotational spectrum of a mixture of 82 % nitrogen and 18 % oxygen at a temperature of 467 K is shown. Below a wavenumber of 30 cm^{-1}, some Rayleigh scattering is distorting the profiles and therefore is cut off. As from predicted spin statistics, peaks of nitrogen odd J have about one third of the height of even J, whereas even J of oxygen are not visible at all. The results reveal the drawback of this method: some peaks of N_2 and O_2 are overlapping (e.g. at $\tilde{\nu}$=60 cm^{-1}). Peaks from N_2 have been chosen for temperature evaluation, since it is often used as an inert gas, and can be used as an internal standard. In this mixture, ground states of $J_{N_2} = 4, 8, 10, 14, 20$ were freestanding peaks that could be considered for evaluation. Because of the weak signal, odd numbers were not taken into account.

Variations of all ratios of the proposed J_{N_2}have been tested in a calibration with 200 ml_n/min N_2 flowing through the reactor, for temperatures between 300 and 525 K. An excerpt of the results are shown in Figure 6-2. The value on the y-axis T_{Raman} is dependent on the measured intensities and complies with the right term in

Equation 3.5. T_{Set} was measured with a thermocouple. The graph highlights the main trend of the results: reliability (R^2) is increasing with increasing sensitivity (m); and the most reliable calibration is with $J8/J20$. The root mean square error (RMSE) of T_{Set} from the straight line was determined as 1.6 K, which is similar to the intrinsic measuring error of a thermocouple (e.g. Type K ± 1.5 K [122]).

The RMSE was calculated for the deviation of the thermocouple measurements T_{Set} from the temperature T_{Lin}, which is calculated by inserting T_{Raman} in the linearization.

$$RMSE = \sqrt{\frac{\sum_{i=1}^{N}(T_{Set} - T_{Lin})^2}{N}}, \qquad (6.1)$$

where N is the number of calibration points. Moreover, the peak intensity is dependent on the Boltzmann distribution, thus the sensitivity of the peak ratio changes for different temperature regions and should be determined according to the application.

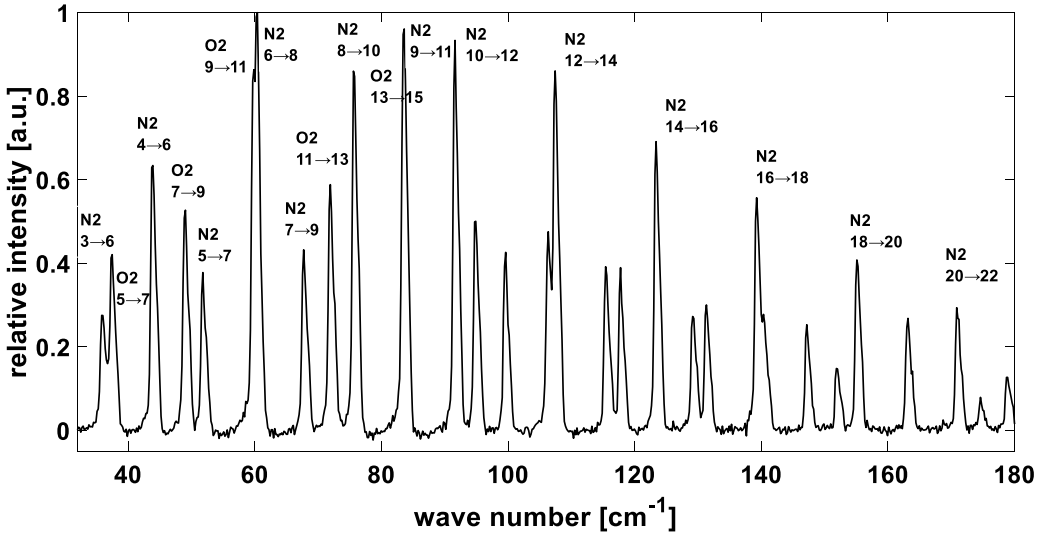

Figure 6-1: Part of a rotational Raman spectrum of a mixture of 82% N_2 and 18% O_2 at 467 K, 0.18 cm^{-1} resolution. Some peaks are labeled with the corresponding rotational quantum numbers of ground and final state.

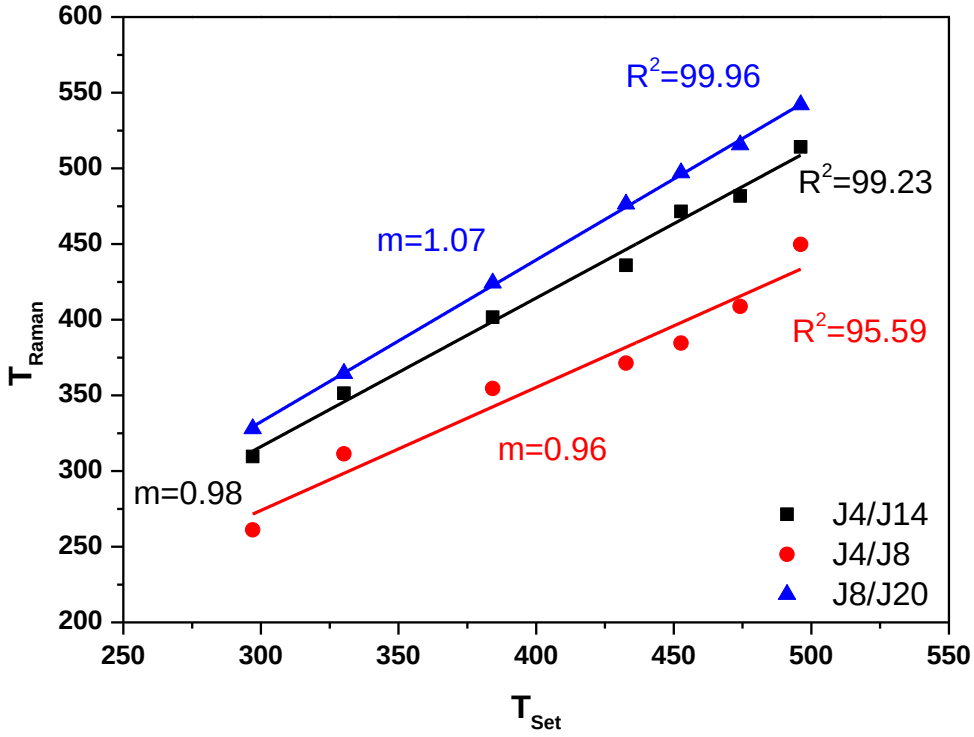

Figure 6-2: Raman rotational temperature calibration lines of N_2 for different ratios of rotational lines. T_{Raman} complies with the right term in Equation 3.5. T_{Set} was measured with a thermocouple.

To determine concentrations of O_2 in N_2, the ratios of the peak areas of $J_{O_2} = 11$ and $J_{N_2} = 8$ were used since these two J have high peaks in the considered temperature range. Calibration measurements were conducted at 23.6 °C and 194.4 °C and are shown in Figure 6-3. The left graph shows the calibration without correcting the signal ratio for temperature, such as shown in Equation 3.7 - the right one includes that correction. It appears obvious that the correction increases the quality of the correlation and must not be neglected.

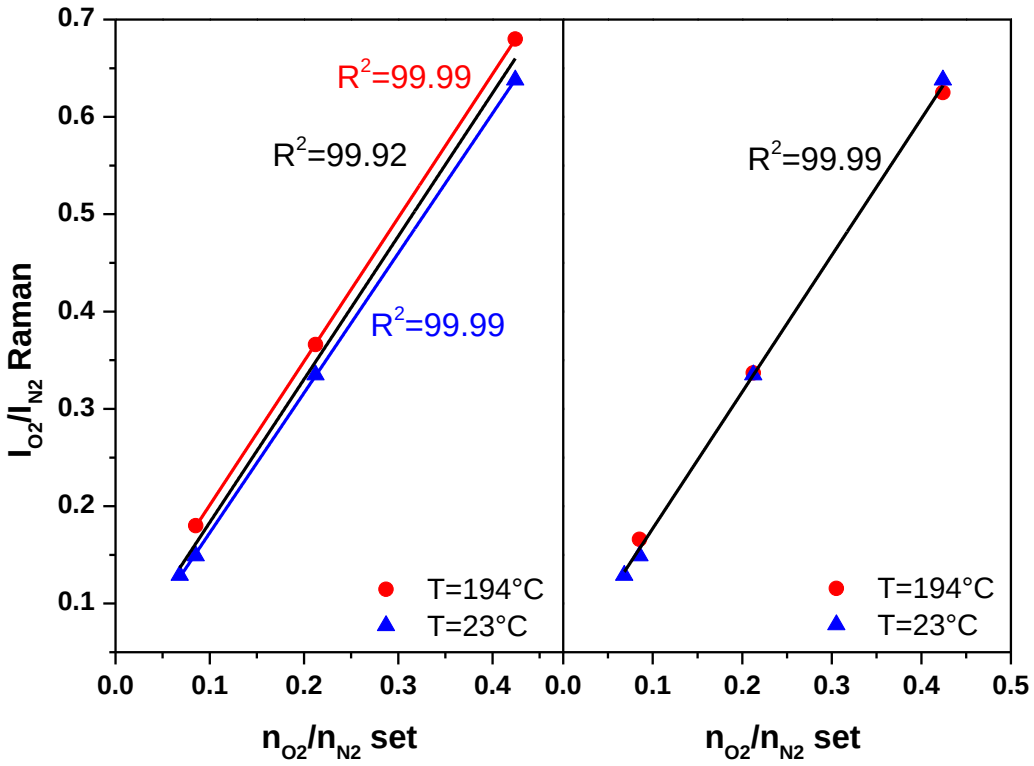

Figure 6-3: Calibration lines for the intensity ratio of $J_{O_2} = 11$ and $J_{N_2} = 8$ for measurements at 23 °C (blue) and 194 °C (red), left without temperature correction, showing calibration lines for all values together (black), for T=194 °C (red) and for T=23 °C (blue). On the right: calibration with temperature correction with one line for all values.

6.2.2 Spatial measurements

The calibrations were performed always on the same spot. Therefore, rotational Raman spectra were measured at different positions inside the reactor (shown in Figure 6-4) with a flow rate of 200 ml_n/min N_2. In the first series of measurements, the reactor was not heated, and hence the gas was entering the reactor at a temperature of 23.7 °C. In the second series, the heating block was set to a temperature of 200 °C. As mentioned in Chapter 6.2.1, the ratios of $J4/J14$ and $J8/J20$ were evaluated. The measured values are listed in Table 6-2 in the order they were measured; the first position was measured again at the end. For the measurement at room temperature, the values evaluated with the $J4/J14$ deviate up to 11.1 °C from room temperature. Values from $J8/J20$ deviate less and the maximal difference is 5.5 °C. For the measurements with 200 °C temperature variations inside the reactor were expected, due to the optical access and presence of the fan to cool the objective. Measurements with a thermocouple already revealed a temperature of 192 °C half a millimeter before and 182 °C half a millimeter after the particle close to the bottom of the

reactor, when setting the heating block to 200 °C. Detailed measurements with the thermocouple at different spots are not possible, since an exact positioning of the thermocouple through the flow distributor of the reactor is not feasible (see Figure 3-2). Because of the previous thermocouple measurement, temperatures are expected to be in the range of 180-200 °C: only the evaluation of $J4/J14$ at position b is off this range by a significant margin (163.9 °C). Nevertheless, some observations induce questions about the accuracy of the measurements and the set-up itself. For example, position a and b have the same distance from the particle, but a is located on the left and b on the right of it (compare Figure 6-4); both evaluations deviate at least by 10 °C (measurement 1, and 2). Even though the reactor is built symmetrically, the fan cooling the objective is mounted on the right side and seems to cause a gradient in the reactor: the left side is in the shadow of the objective and therefore has a worse heat transport due to less convection. Furthermore, before (position c and d) and after the particle (position e and f), the result from $J4/J14$ predicts nearly the same temperature, whereas the results from $J8/J20$ predict a temperature gradient. The latter agrees with the previous thermocouple measurements. In Figure 6-4 only the evaluation of $J8/J20$ is shown, since the values from $J4/J14$ were not considered as reliable in view of the previous findings. When looking at the z-axis, it is peculiar that the temperature for T_{in}=200 °C is decreasing with decreasing z. Since the window is on the top (at z=20 mm), and the reactor is isolated on the bottom, the opposite would be expected. This is an indication that the instrumentation factor is changing by moving the objective up and down.

Furthermore, the repetition of the measurement at position a (measurement 7), results in deviations of up to 18 °C compared to the first measurement at this position (measurement 1) at T_{in}=23.7 and T_{in}=200 °C, respectively. The $J8$ and $J20$ peaks of these four measurements are shown in Figure 6-5. At 23.7 °C, the pathway of the $J8$ and $J20$ peaks is similar; only the $J8$ peak is a little smaller, which explains the calculated temperature difference of 3.3 °C. At 200 °C, the efficiency of the detection system changed between the two measurements. Both the $J8$ as well as the $J20$ peak decreased. The background from both measurements is nearly identical, and cannot be the cause of the observed difference. This is another clue of a change in the instrumentation factor. Another alternative cause of this phenomenon could be dust from the insulation material that is brought onto the window by the fan.

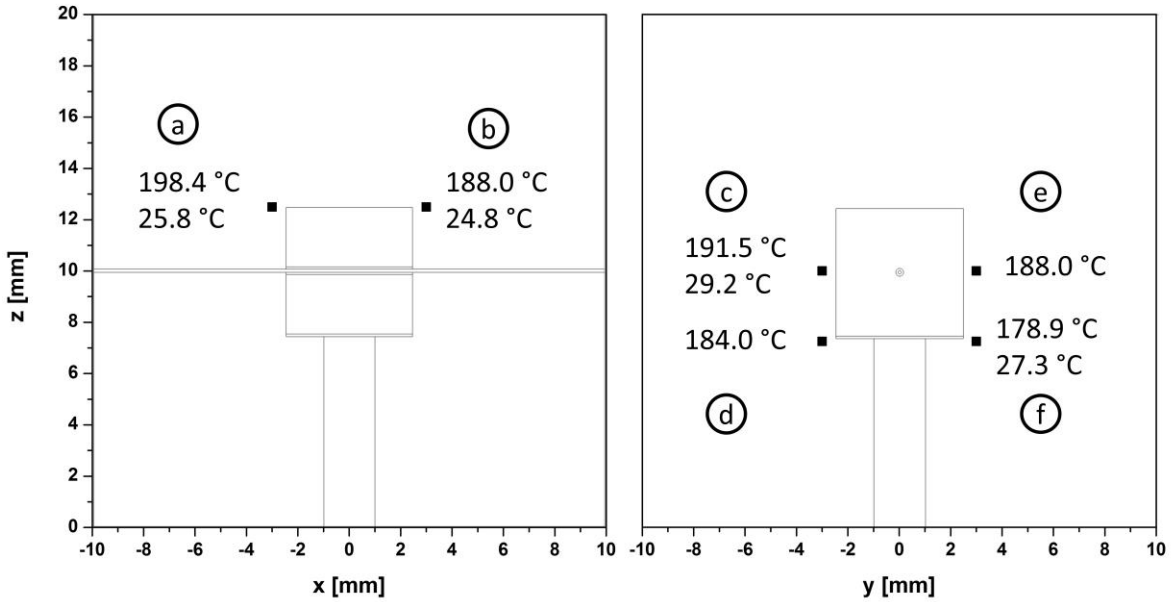

Figure 6-4: Measurement with $T_{in} = 200\ °C$ and $T_{in} = 23.7\ °C$ at different positions in the reactor, evaluated with the ratio of $J8/J20$. The gas is flowing from $-y$ to $+y$. The section on the left is at $y = 0$ and on the right at $x = 0$.

Table 6-2: Measurement at $T_{in} = 23.7°C$ and $T_{in} = 200°C$ at different positions in the reactor. Evaluated with the ratio of $J4/J14$ and $J8/J20$ respectively.

		T [°C]			
		T_{in}=23.7 °C		T_{in}=200 °C	
Measurement	position	J4/J14	J8/J20	J4/J14	J8/J20
1	a	27.2	25.8	189.7	198.4
2	b	37.2	24.8	163.9	188.0
3	e			194.7	184.6
4	f	31.6	27.3	181.9	178.9
5	d			202.3	184.0
6	c	34.1	29.2	182.0	191.5
7	a	34.8	29.1	184.0	180.7

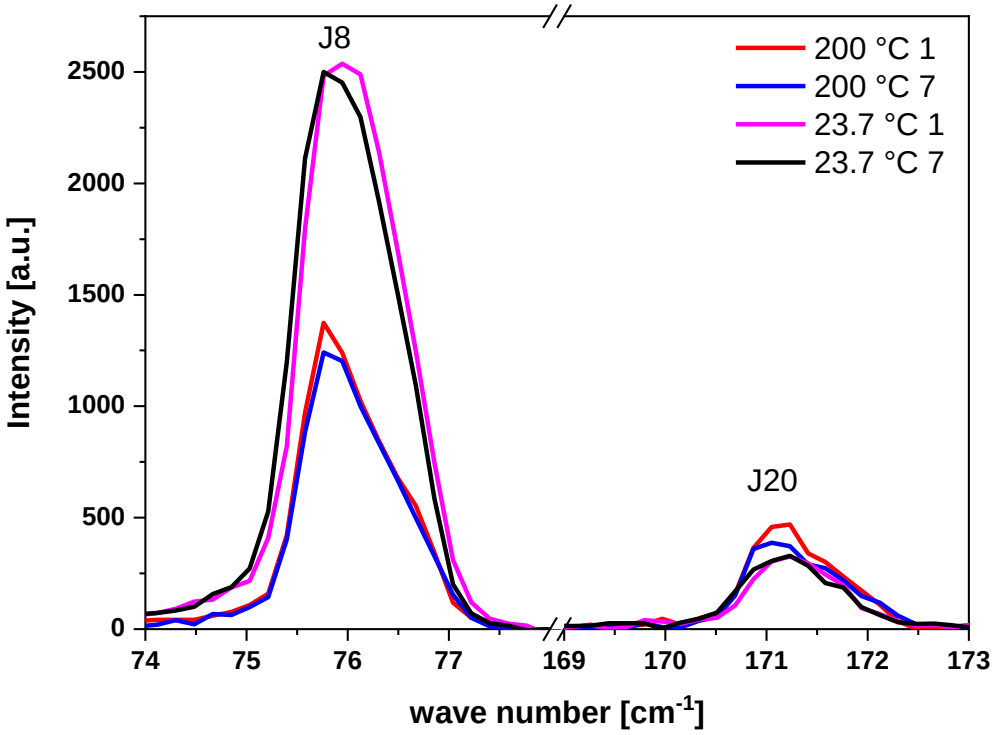

Figure 6-5: $J8$ and $J20$ N_2 peaks at the same position for $T_{in} = 200\,°C$ and $T_{in} = 23.7\,°C$, respectively and a repetition thereof. Measurements refer to Table 6-2.

6.2.3 Multi-component mixtures

Measuring properties of a multi-component mixture will increase the complexity of an already convoluted task. For the basic CO oxidation, the rotational bands of at least three components will superimpose; by using an inert such as N_2, even a fourth component needs to be considered. Figure 6-6 shows the calculated rotational Raman spectra for N_2, O_2, CO, and CO_2 at 500 K according to Equation 3.6. The peak heights of each species are relative to the maximum peak of the same component, and the width of each peak was chosen to be one wavenumber for a better overview. The measurements showed a peak width of at least two wavenumbers; they would need to be represented as a Gaussian function, rather than the bars of fixed width depicted in the graph. Observing the graph, it appears clear that it is nearly impossible to find a wave number with only one rotational transition. Nevertheless, by superimposing several Gaussian functions, an evaluation might be possible - albeit complicated; otherwise, no statement about the accuracy can be made.

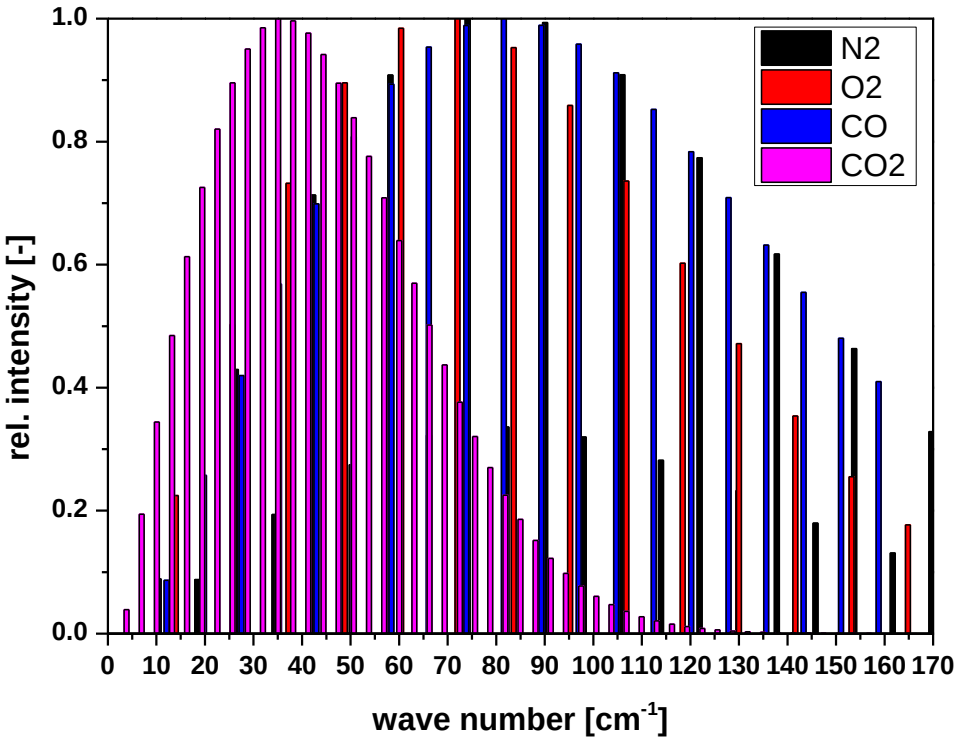

Figure 6-6: Calculated rotational Raman spectra for N2, O2, CO, and CO2 at 500 K, the peak heights of each species are relative to the maximum peak of the same, the width of each peak is one wave number.

Firstly, the accuracy of the measurements needs to be increased, as shown in the previous chapter. One option is to increase the peak intensity, which can be achieved in various ways.

Peak intensities are increasing linearly with the incident laser power. Therefore, in previous works, another set-up was preferred. The Raman detector is set-up at a 90° angle to a polarized laser beam. Since the Raman scattering is predominantly not depolarizing the laser, it will only be detected if the polarization of the laser is perpendicular to the detection optical axis. When the laser is polarized parallel to the optical detection axis, only detrimental effects like fluorescence and stray light will be detected. Since these effects are mainly not polarization-dependent, they appear in both measurements. By subtracting the parallel measurement from the perpendicular one, the background can be eliminated. This setup allows higher laser intensity (> 5 W) or measurements with pulsed lasers [29,123]. However, in this way, spatial profiles with high resolution are not possible to measure. Another option to increase the peak intensity is by using UV lasers, which takes advantage of the fourth power

frequency dependence. Furthermore, the peak intensities increase linearly with the integration time. In this work, the spectra were integrated for 45 minutes - which is already a long exposure time, considering that typically a highly-resolved spatial spectrum would consist of hundreds of points.

Moreover, from the results of the previous chapter, it is not clear if the instrumentation function, and therefore the calibrations, are changing at different positions in the reactor. This has to be investigated systematically. The missing pinhole in the microscope (see Chapter 3.6.1) affects the accuracy as well: the signal from other planes might distort the results.

To measure temperature and concentration in the gas phase simultaneously, with only one spectrum, and high accuracy with temperatures under 500 K, in a multi-component mixture with a confocal microscope does not seem to be feasible. The rotational band temperature evaluation shows promising results though and could be used to determine the temperature from an O- branch. This overcomes the superimposing bands' problem of the multicomponent mixture. Furthermore, a least square fit can be used to fit Equation 2.56 to the whole rotational spectrum. In this way, Breiland et al. [124] could determine the temperature with ±1 K accuracy. In this case, concentrations can be determined from the vibrational Q-bands of the different molecules. However, a second measurement would be necessary, since spectrometer gratings usually either have a wide range (to measure all the vibrational bands) or a small range (to resolve rotational bands).

Overall, the set-up used in this work allows measuring gas phase temperatures and concentrations from rotational Raman bands. By measuring at the same spot, calibrations with high accuracies of R^2 above 99.9% were achieved. However, for accurate spatial measurements, more tests, and an improvement of the set-up are needed - especially in the case of measuring multicomponent mixtures. Calibration curves should be determined at different z-positions: like this, it might be possible to determine an instrumentation factor in dependence of it. Furthermore, the cooling of the objective needs to be improved: dust on the top window might disturb the measurements. Overall, a temperature gradient inside the reactor disturbs measurements with a reacting particle, which would contradict the purpose of the set-up.

7 Summary of results and future perspective

In this thesis a new method was developed, one that allows the in-situ measurement of concentration profiles inside and in the boundary layer of a given porous catalyst particle with industrial dimensions.

The method is based on a sampling capillary made from fused silica, which is connected to a quadrupole mass spectrometer. To not disturb the minute diffusional fluxes inside porous catalyst pellets, the sampling volume was decreased to less than 1µl/min by using capillaries with an inner diameter of 10 µm or less. To allow for quantitative analysis, the probing volume was directly inserted into the ionization head of the mass spectrometer and the mid axis potential of the quadrupole was increased. In this manner, samples taken with a 2 µm capillary could be analyzed; this resulted in a calculated sampling volume of less than 1 nl/min.

The new technique was tested investigating CO oxidation as the model reaction on a platinum-coated, mesoporous equilateral alumina cylinder of 5 mm. To be able to move the capillary (130 µm outer diameter) through the particle, a 300 µm channel was drilled through the center of the cylinder. In this way, sampling could be either done by the tip of the capillary, or at a side orifice, which was drilled into the capillary with a focused ion beam.

Furthermore, to support the experimental investigations, CFD simulations integrating a literature kinetic were conducted, to ascertain the invasiveness of the proposed method; they predicted diffusion through the annular gap between capillary and channel wall, and that the sampling process would distort the measured profiles in comparison to the pristine pellet. Nevertheless, both these phenomena can be minimized to keep distortions negligible. Sampling with the side orifice provided higher quality results since sampling with the tip lead to a shift in the profiles because samples are taken not only from the spot of the tip but also from

the open side which the tip is facing. Furthermore, simulations demonstrate that the invasiveness of the method can be reduced, by reducing the gap between the capillary and the particle. This can be achieved either by drilling a smaller channel or using a capillary with a bigger outer diameter. Since the demonstration pellet is mesoporous, Knudsen diffusion is prevailing in the particle - which results in low diffusional fluxes. In simulations in which Knudsen diffusion is not present, higher diffusional fluxes in the particle are observed which in turn results in a decrease of the invasiveness of the method.

Demonstration measurements for CO oxidation in a cylindrical, Pt-containing, mesoporous Al_2O_3 pellet show that highly-resolved species profiles can be obtained, despite the low diffusional fluxes. Spatial resolutions on a 100 μm scale have been achieved, which are high, considering that industrial catalyst pellets have dimensions in the order of several millimeters to a few centimeters [125]. Measurements confirmed the simulation results: in contrast to measurements with the tip, measurements with the side orifice showed the expected symmetrical profiles inside the pellet.

The method allows probing the interaction between catalytic reactions, film, and pore diffusion; and to observe resulting phenomena such as boundary layers, multiple steady states, and oscillations. It is possible to directly determine the boundary layer thickness from the profiles and to directly calculate mass transport parameters. For Reynolds numbers above 20, good agreement between literature values and experimental data was found. For Reynolds numbers less than 10, wall effects, caused by the relatively small cross section of the reactor, resulted in deviations of more than 50 %. Multiple steady states and hysteresis were measured by increasing and decreasing either temperature or oxygen concentration. The experimental values were in the range of theoretical models from literature predicting multiple steady states. During temperature oscillations, an increase of frequencies with increasing temperature was observed, which supports the findings of a surface-restructuring model developed by Hendriksen [38].

The sampling capillary technique allows the measurement of concentration profiles in the boundary layer only along the axis of the capillary. To gain more information about temperature and concentration in the gas phase, the reactor was coupled with Raman microscopy. Test measurements were conducted with different concentrations of oxygen and nitrogen at various temperatures. Accurate calibration

lines could be determined from rotational bands, by measuring at the same position. However, moving the reactor or the microscope resulted in a changing system function, which is, in turn, changing the calibrations and increases the systematic error. In the future, this function needs to be determined.

In conclusion, with this method, it becomes possible to measure what effect size and shape of the catalyst pellet, pore network, spatial distribution of the active component, and the orientation of the pellet to the flow have on product selectivity and yield. Such measurements are a valuable complement to numerical simulations, which were until today the only way to access intra-pellet concentration profiles. In principle, it should be possible to extend this method to spatially-resolved temperature and spectroscopic measurements using thin temperature and spectroscopic probes; further research is needed in reactor construction, to solve the constraints which hinder the proposed method.

Appendix

A Parameter

Table A.0-1: Parameter for calculations in Chapter 5 at 170 °C and 300 °C.

T	[°C]	170	300
$c_{CO,in}$	[mol m^{-3}]	1.6	1.2
c_p	[J kg^{-1} K^{-1}]	552	554
d_p	[m]	5.0E-03	5.0E-03
d_v	[m]	5.7E-03	5.7E-03
d_{cross}	[m]	7.8E-03	7.8E-03
d_{axial}	[m]	9.9E-03	9.9E-03
$D_{CO_2,m}$	[m^2 s^{-1}]	2.6E-05	
$D_{CO,m}$	[m^2 s^{-1}]	3.7E-05	5.8E-05
$D_{CO,eff}$	[m^2 s^{-1}]	1.4E-06	1.7E-06
$E_{A,max}$	[J mol^{-1}]	100000	100000
$E_{A,min}$	[J mol^{-1}]	45000	45000
$\dot{V_{in}}$	[ml_n min^{-1}]	450	450
$\Delta_R H$	[J mol^{-1}]	287000	287000
η	[Pa s]	3.0E-05	3.60E-05
λ_{eff}	[W m^{-1} K^{-1}]	0.10	0.10
λ_f	[W/(m K)]	0.025	0.030
ρ_f	[kg/m^3]	1.06	0.82

List of symbols

Fundamental constants

amu	1.66056 10^{27} kg	Atomic mass unit
c	299792458 m s^{-1}	Speed of light in vacuum
e	1.60219 10^{-19} C	Elementary charge
h	6.62618 10^{-34} J s	Planck's constant
k_B	1.38066 10^{-23} J K^{-1}	Boltzmann's constant
R	8.314 J mol^{-1} K^{-1}	Universal gas constant

Latin symbols

a	[-]	Parameter in the Mathieu equation
B	[m^{-1}]	Rotational constant
c	[mol m^{-3}]	Concentration
$\bar{c}$	[m s^{-1}]	Thermal velocity
c_p	[J kg^{-1} K^{-1}]	Heat capacity
$D_{i,eff}$	[m^2 s^{-1}]	Effective diffusion coefficient
D_{ij}	[m^2 s^{-1}]	Binary diffusion coefficient
$D_{i,K}$	[m^2 s^{-1}]	Knudsen diffusion coefficient
D_{im}	[m^2 s^{-1}]	Mixture averaged diffusion coefficients
d	[m]	Capillary diameter
d	[m]	Characteristic length
d_v	[m]	Equivalent spherical diameter
E	[J]	Rotational energy lever

E_A	[J mol^{-1}]	Activation energy
$G(v)$	[m^{-1}]	Vibrational term
g_i	[-]	Degeneracy of the level i
$\Delta_R H$	[J mol^{-1}]	Heat of reaction
h	[W m^2 K^{-1}]	Heat transfer coefficient
I	[-]	Identity matrix
I	[-]	Signal Intensity
I	[-]	Spin quantum number
J	[-]	Rotational quantum number
j_i	[kg m^{-2} s^{-1}]	Diffusion mass flux
K		Equilibrium constant
k		Reaction rate constant
k_c	[m s^{-1}]	Mass transfer coefficient
l	[m]	Length of capillary
M	[kg mol^{-1}]	Molar weight
m	[-]	Slope of the calibration lines
m	[kg]	Mass
N	[-]	Number of molecules/ measured points
N	[mol m^{-2} s^{-1}]	Mole flux
n	[-]	Reaction order
n	[mol]	Amount of substance
Nu	d_v h λ_f^{-1} [-]	Nusselt number
P	[Pa]	Pressure
p	[Pa]	Partial pressure
Pr	η c_p λ_f^{-1}[-]	Prandtl number
T	[K]	Temperature
Q	[-]	Partition function
q	[-]	Parameter in the Mathieu equation
q	[W m^{-2} s^{-1}]	Heat flux
R	[mol m^{-3} s^{-1}]	Rate of reaction

$\tilde{R}$	[mol m^{-3} s^{-1}]	Volume average rate of reaction
R^2	[%]	Coefficient of determination
r	[m]	Radius
r	[-]	Resolution of the QMS
r_0	[m]	Half distance between the quadrupole rods
Sc	$\eta\ \rho_f^{-1}\ D_m^{-1}$[-]	Schmidt number
Sh	$d_v\ k\ D_m^{-1}$[-]	Sherwood number
s	[-]	Slope of the mass scan line
t	[s]	Time
U	[V]	Direct current
V	[V]	RF voltage
V	[m^3]	Volume
$\dot{V}$	[m^3 s^{-1}]	Volume flow
w	[-]	Mass fraction
x	[-]	Mole fraction
x_e	[-]	Anharmonicity constant

Greek symbols

β	$-\Delta H_R\ D_{eff}\ c_{co}^s\ \lambda_{eff}^{-1}\ T^{-1}$ [-]	Prater number
β_B	$-\Delta H_R\ k_c\ c_{co}^B\ h^{-1}\ T^{-1}$ [-]	Prater number for bulk conditions
γ	$-E_A\ R^{-1}\ T^1$ [-]	Arrhenius number
δ	[m]	Boundary layer thickness
ε	[-]	Particle porosity
η	[-]	Effectiveness factor
η	[kg m^{-1} s^{-1}]	Dynamic viscosity
λ	[W m^{-1} K^{-1}]	Thermal conductivity
ν	[m^2 s^{-1}]	Kinematic viscosity
ν	[-]	Stoichiometric coefficient
$\tilde{\nu}$	[cm^{-1}]	Wavenumber

ρ	[kg m^{-3}]	Density
σ_{ij}	[m]	Collision diameter
τ	[-]	Parameter in the Mathieu equation
τ	[N]	Viscous stress tensor
τ	[-]	Tortuosity
υ	[-]	Vibrational quantum number
φ	[-]	Permeability
Φ	[V]	Electric potential in between the quadrupole rods
Φ_0	[V]	Electric potential applied to the quadrupole rods
ϕ	[-]	Thiele modulus
Ω^*	[-]	Collision integral
ω	[s^{-1}]	Angular frequency of the RF-voltage

Abbreviations

AS	Anti-Stokes
EI	Electron impact ionization
FIB	Focused ion beam
ID	Inner diameter
IR	Infrared
LHHW	Langmuir-Hinshelwood-Hougen-Watson
MS	Mass spectrometer
OD	Outer diameter
R	Rayleigh
RPM	Revolutions per minute
RMSE	Root mean square error
S	Stokes
UHV	Ultra-high vacuum
QMS	Quadrupole mass spectrometer

Subscripts

B	Bulk
$calc$	Calculated
f	Fluid
g	Gas
in	Inlet
p	Particle
rot	Rotational
s	Solid
s	Surface
vib	Vibrational

References

[1] O. Deutschmann, H. Knözinger, K. Kochloefl, T. Turek, Heterogeneous Catalysis and Solid Catalysts, 1. Fundamentals, in: Ullmanns Encycl. Ind. Chem., American Cancer Society, 2011. https://doi.org/10.1002/14356007.a05_313.pub3.

[2] C.H. Bartholomew, R.J. Farrauto, Fundamentals of Industrial Catalytic Processes, 2nd ed., John Wiley & Sons, 2005.

[3] G. Eigenberger, W. Ruppel, Catalytic Fixed-Bed Reactors, in: Ullmanns Encycl. Ind. Chem., American Cancer Society, 2012. https://doi.org/10.1002/14356007.b04_199.pub2.

[4] F. Jüttner, Reaktionskinetik und Diffusion, Z. Für Phys. Chem. 65U (1909) 595–623. https://doi.org/10.1515/zpch-1909-6536.

[5] Y.B. Zeldovich, On the theory of reactions on powders and porous substances, Acta Physicochim URSS. 10 (1939) 583.

[6] G. Damköhler, Influence of diffusion, fluid flow, and heat transport on the yield in chemical reactors, Int Chem Eng. 28 (1988) 132–198.

[7] E.W. Thiele, Relation between Catalytic Activity and Size of Particle, Ind. Eng. Chem. 31 (1939) 916–920. https://doi.org/10.1021/ie50355a027.

[8] D.F. Kamenetzki, Stoff und Wärmeübertragung in der chemischen Kinetik, Springer, Berlin, 1959.

[9] R.E. Schilson, N.R. Amundson, Intraparticle diffusion and conduction in porous catalysts—I: Single reactions, Chem. Eng. Sci. 13 (1961) 226–236. https://doi.org/10.1016/0009-2509(61)80019-5.

[10] R.E. Schilson, N.R. Amundson, Intraparticle diffusion and conduction in porous catalysts—II: Complex reactions, Chem. Eng. Sci. 13 (1961) 237–244. https://doi.org/10.1016/0009-2509(61)80020-1.

[11] R. Aris, The Mathematical Theory of Diffusion and Reaction in Permeable Catalysts: The theory of the steady state, Clarendon Press, 1975.

[12] R. Aris, The Mathematical Theory of Diffusion and Reaction in Permeable Catalysts: Questions of Uniqueness, Stability, and Transient Behaviour, Clarendon Press, 1975.

[13] D. Luss, Steady-state and dynamic behavior of a single catalytic pellet, Chem. React. Theory- Rev. (1977) 191–268.

[14] F.J. Keil, Diffusion and reaction in porous networks, Catal. Today. 53 (1999) 245–258. https://doi.org/10.1016/S0920-5861(99)00119-4.

[15] A.G. Dixon, M. Nijemeisland, E.H. Stitt, Packed Tubular Reactor Modeling and Catalyst Design using Computational Fluid Dynamics, in: G.B. Marin (Ed.), Adv. Chem. Eng., Academic Press, 2006: pp. 307–389. https://doi.org/10.1016/S0065-2377(06)31005-8.

[16] N. Jurtz, M. Kraume, G.D. Wehinger, Advances in fixed-bed reactor modeling using particle-resolved computational fluid dynamics (CFD), Rev. Chem. Eng. 35 (2019) 139–190. https://doi.org/10.1515/revce-2017-0059.

[17] A.G. Dixon, CFD study of effect of inclination angle on transport and reaction in hollow cylinder catalysts, Chem. Eng. Res. Des. 92 (2014) 1279–1295. https://doi.org/10.1016/j.cherd.2013.11.018.

[18] G.D. Wehinger, F. Klippel, M. Kraume, Modeling pore processes for particle-resolved CFD simulations of catalytic fixed-bed reactors, Comput. Chem. Eng. 101 (2017) 11–22. https://doi.org/10.1016/j.compchemeng.2017.02.029.

[19] B. Partopour, A.G. Dixon, An integrated workflow for resolved-particle packed bed models with complex particle shapes, Powder Technol. 322 (2017) 258–272. https://doi.org/10.1016/j.powtec.2017.09.009.

[20] B. Partopour, R.C. Paffenroth, A.G. Dixon, Random Forests for mapping and analysis of microkinetics models, Comput. Chem. Eng. (2018). https://doi.org/10.1016/j.compchemeng.2018.04.019.

[21] B. Partopour, A.G. Dixon, Reduced Microkinetics Model for Computational Fluid Dynamics (CFD) Simulation of the Fixed-Bed Partial Oxidation of Ethylene, Ind. Eng. Chem. Res. 55 (2016) 7296–7306. https://doi.org/10.1021/acs.iecr.6b00526.

[22] B. Partopour, A.G. Dixon, Computationally efficient incorporation of microkinetics into resolved-particle CFD simulations of fixed-bed reactors, Comput. Chem. Eng. 88 (2016) 126–134. https://doi.org/10.1016/j.compchemeng.2016.02.015.

[23] B. Partopour, A. Troupel, A.G. Dixon, Flux-dependent anisotropic pellet diffusivity in particle-resolved CFD simulations of fixed beds, Chem. Eng. Sci. 198 (2019) 224–234. https://doi.org/10.1016/j.ces.2018.10.005.

[24] R. Horn, N.J. Degenstein, K.A. Williams, L.D. Schmidt, Spatial and temporal profiles in millisecond partial oxidation processes, Catal. Lett. 110 (2006) 169–178. https://doi.org/10.1007/s10562-006-0117-8.

[25] W.P. Partridge, J.M.E. Storey, S.A. Lewis, R.W. Smithwick, G.L. DeVault, M.J. Cunningham, N.W. Currier, T.M. Yonushonis, Time-Resolved Measurements of Emission Transients By Mass Spectrometry, SAE Trans. 109 (2000) 2983–2991.

[26] J. Sá, D.L. Abreu Fernandes, F. Aiouache, A. Goguet, C. Hardacre, D. Lundie, W. Naeem, W. P. Partridge, C. Stere, SpaciMS: spatial and temporal operando resolution of reactions within catalytic monoliths, Analyst. 135 (2010) 2260–2272. https://doi.org/10.1039/C0AN00303D.

[27] R. Horn, O. Korup, M. Geske, U. Zavyalova, I. Oprea, R. Schlögl, Reactor for in situ measurements of spatially resolved kinetic data in heterogeneous catalysis, Rev. Sci. Instrum. 81 (2010) 064102. https://doi.org/10.1063/1.3428727.

[28] M. Geske, O. Korup, R. Horn, Resolving kinetics and dynamics of a catalytic reaction inside a fixed bed reactor by combined kinetic and spectroscopic profiling, Catal. Sci. Technol. 3 (2012) 169–175. https://doi.org/10.1039/C2CY20489D.

[29] F. Küster, P. Nikrityuk, M. Junghanns, S. Nolte, A. Tünnermann, R. Ackermann, A. Richter, S. Guhl, B. Meyer, In-situ investigation of single particle gasification in a defined gas flow applying TGA with optical measurements, Fuel. 194 (2017) 544–556. https://doi.org/10.1016/j.fuel.2016.12.069.

[30] L.L. Hegedus, E.E. Petersen, An Improved Single-Pellet Reactor to Study the Interaction of Kinetics with Mass Transfer Effects in Heterogeneous Catalysis, Ind. Eng. Chem. Fundam. 11 (1972) 579–584. https://doi.org/10.1021/i160044a025.

[31] C. Chmelik, M. Liebau, M. Al-Naji, J. Möllmer, D. Enke, R. Gläser, J. Kärger, One-Shot Measurement of Effectiveness Factors of Chemical Conversion in Porous Catalysts, ChemCatChem. 10 (2018) 5602–5609. https://doi.org/10.1002/cctc.201801530.

[32] R.H. Venderbosch, W. Prins, W.P.M. van Swaaij, Platinum catalyzed oxidation of carbon monoxide as a model reaction in mass transfer measurements, Chem. Eng. Sci. 53 (1998) 3355–3366. https://doi.org/10.1016/S0009-2509(98)00151-1.

[33] R.C. Shishu, L.S. Kowalczyk, The Oxidation of Carbon Monoxide on Supported Platinum, Platin. Met. Rev. 18 (1974) 58–64.

[34] O. Deutschmann, H. Knözinger, K. Kochloefl, T. Turek, Heterogeneous Catalysis and Solid Catalysts, 2. Development and Types of Solid Catalysts, in: Ullmanns Encycl. Ind. Chem., American Cancer Society, 2011. https://doi.org/10.1002/14356007.o05_o02.

[35] M. Thiemann, E. Scheibler, K.W. Wiegand, Nitric Acid, Nitrous Acid, and Nitrogen Oxides, in: Ullmanns Encycl. Ind. Chem., Wiley-VCH Verlag GmbH & Co. KGaA, 2000. http://onlinelibrary.wiley.com/doi/10.1002/14356007.a17_293/abstract (accessed January 10, 2017).

[36] H.S. Fogler, Elements of Chemical Reaction Engineering, 3rd ed., Prentice Hall, 2001.

[37] M. Behrens, F. Studt, I. Kasatkin, S. Kühl, M. Hävecker, F. Abild-Pedersen, S. Zander, F. Girgsdies, P. Kurr, B.-L. Kniep, M. Tovar, R.W. Fischer, J.K. Nørskov, R. Schlögl, The Active Site of Methanol Synthesis over Cu/ZnO/Al2O3 Industrial Catalysts, Science. 336 (2012) 893–897. https://doi.org/10.1126/science.1219831.

[38] B.L.M. Hendriksen, M.D. Ackermann, R. van Rijn, D. Stoltz, I. Popa, O. Balmes, A. Resta, D. Wermeille, R. Felici, S. Ferrer, J.W.M. Frenken, The role of steps in

surface catalysis and reaction oscillations, Nat. Chem. 2 (2010) 730–734. https://doi.org/10.1038/nchem.728.

[39] S.B. Vendelbo, C.F. Elkjær, H. Falsig, I. Puspitasari, P. Dona, L. Mele, B. Morana, B.J. Nelissen, R. van Rijn, J.F. Creemer, P.J. Kooyman, S. Helveg, Visualization of oscillatory behaviour of Pt nanoparticles catalysing CO oxidation, Nat. Mater. 13 (2014) 884–890. https://doi.org/10.1038/nmat4033.

[40] Y. Dong, F.J. Keil, O. Korup, F. Rosowski, R. Horn, Effect of the catalyst pore structure on fixed-bed reactor performance of partial oxidation of n-butane: A simulation study, Chem. Eng. Sci. 142 (2016) 299–309. https://doi.org/10.1016/j.ces.2015.12.004.

[41] A. Argönül, F.J. Keil, Ethylene Hydrogenation in Pellets with Different Pore Structures, Measured in a One-Sided Single-Pellet Reactor, Int. J. Chem. React. Eng. 17 (2019). https://doi.org/10.1515/ijcre-2018-0166.

[42] VDI-Wärmeatlas, 11., bearb. und erw. Aufl., Springer Vieweg, 2013.

[43] D.S. Christen, Praxiswissen der chemischen Verfahrenstechnik: Handbuch für Chemiker und Verfahrensingenieure, 2., bearbeitete und ergänzte Auflage, Springer, Heidelberg, 2010.

[44] F. Keil, Diffusion und chemische Reaktionen in der Gas/Feststoff-Katalyse, Springer, 1999.

[45] G.F. Froment, K.B. Bischoff, J.D. Wilde, Chemical Reactor Analysis and Design, 3rd edition, John Wiley & Sons Inc, Hoboken, 2011.

[46] R. Krishna, Problems and pitfalls in the use of the fick formulation for intraparticle diffusion, Chem. Eng. Sci. 48 (1993) 845–861. https://doi.org/10.1016/0009-2509(93)80324-J.

[47] J.O. Hirschfelder, C.F. Curtiss, R.B. Bird, Molecular theory of gases and liquids, Corr. print. with notes added, Wiley, New York, 1964.

[48] M. Baerns, Technische Chemie, 2. erw. Aufl., Wiley-VCH, VTB-358, Weinheim, 2013.

[49] F.J. Keil, Modeling Reactions in Porous Media, in: Model. Simul. Heterog. Catal. React., John Wiley & Sons, Ltd, 2011: pp. 149–186. https://doi.org/10.1002/9783527639878.ch5.

[50] C.E. Salmas, G.P. Androutsopoulos, A Novel Pore Structure Tortuosity Concept Based on Nitrogen Sorption Hysteresis Data, Ind. Eng. Chem. Res. 40 (2001) 721–730. https://doi.org/10.1021/ie000626y.

[51] J. Solsvik, H.A. Jakobsen, A Survey of Multicomponent Mass Diffusion Flux Closures for Porous Pellets: Mass and Molar Forms, Transp. Porous Media. 93 (2012) 99–126. https://doi.org/10.1007/s11242-012-9946-7.

[52] J.B. Butt, Thermal conductivity of porous catalysts, AIChE J. 11 (1965) 106–112. https://doi.org/10.1002/aic.690110123.

[53] P. Harriott, Thermal conductivity of catalyst pellets and other porous particles: Part I: Review of models and published results, Chem. Eng. J. 10 (1975) 65–71. https://doi.org/10.1016/0300-9467(75)88018-X.

[54] R.A. Mischke, J.M. Smith, Thermal conductivity of alumina catalyst pellets, Ind. Eng. Chem. Fundam. 1 (1962) 288–292.

[55] B. Sosna, Y. Dong, L. Chromow, O. Korup, R. Horn, Effective Axial Thermal Conductivity in Catalyst Packings from High Resolution Temperature Profiles, Chem. Ing. Tech. 88 (2016) 1676–1683. https://doi.org/10.1002/cite.201600062.

[56] D. Luss, Uniqueness and multiplicity criteria for porous catalytic pellets and packed bed reactors with uniform intra-particle temperature, in: Chem. React. Eng. Proc. 4th Int. Eur. Symp., Heidelberg, 1976: pp. 280–289.

[57] C. Mcgreavy, J.M. Thornton, Generalised criteria for the stability of catalytic reactors, Can. J. Chem. Eng. 48 (1970) 187–191. https://doi.org/10.1002/cjce.5450480216.

[58] D. Luss, Sufficient conditions for uniqueness of the steady state solutions in distributed parameter systems, Chem. Eng. Sci. 23 (1968) 1249–1255. https://doi.org/10.1016/0009-2509(68)89034-7.

[59] J. Solsvik, H.A. Jakobsen, Modeling of multicomponent mass diffusion in porous spherical pellets: Application to steam methane reforming and methanol synthesis, Chem. Eng. Sci. 66 (2011) 1986–2000. https://doi.org/10.1016/j.ces.2011.01.060.

[60] H.-J. Freund, G. Meijer, M. Scheffler, R. Schlögl, M. Wolf, Die CO-Oxidation als Modellreaktion für heterogene Prozesse, Angew. Chem. 123 (2011) 10242–10275. https://doi.org/10.1002/ange.201101378.

[61] B.C. Sales, J.E. Turner, M.B. Maple, Oscillatory oxidation of CO over Pt, Pd and Ir catalysts: Theory, Surf. Sci. 114 (1982) 381–394. https://doi.org/10.1016/0039-6028(82)90692-6.

[62] D.L. Trimm, Z.I. Önsan, Onboard Fuel Conversion for Hydrogen-Fuel-Cell-Driven Vehicles, Catal. Rev. 43 (2001) 31–84. https://doi.org/10.1081/CR-100104386.

[63] X. Xie, Y. Li, Z.-Q. Liu, M. Haruta, W. Shen, Low-temperature oxidation of CO catalysed by Co_3O_4 nanorods, Nature. 458 (2009) 746–749. https://doi.org/10.1038/nature07877.

[64] D. Chan, S. Tischer, J. Heck, C. Diehm, O. Deutschmann, Correlation between catalytic activity and catalytic surface area of a Pt/Al2O3 DOC: An experimental and microkinetic modeling study, Appl. Catal. B Environ. 156–157 (2014) 153–165. https://doi.org/10.1016/j.apcatb.2014.03.009.

[65] A.D. Allian, K. Takanabe, K.L. Fujdala, X. Hao, T.J. Truex, J. Cai, C. Buda, M. Neurock, E. Iglesia, Chemisorption of CO and Mechanism of CO Oxidation on Supported Platinum Nanoclusters, J. Am. Chem. Soc. 133 (2011) 4498–4517. https://doi.org/10.1021/ja110073u.

[66] S.E. Voltz, C.R. Morgan, D. Liederman, S.M. Jacob, Kinetic Study of Carbon Monoxide and Propylene Oxidation on Platinum Catalysts, Ind. Eng. Chem. Prod. Res. Dev. 12 (1973) 294–301. https://doi.org/10.1021/i360048a006.

[67] L.L. Hegedus, S.H. Oh, K. Baron, Multiple steady states in an isothermal, integral reactor: The catalytic oxidation of carbon monoxide over platinum-alumina, AIChE J. 23 (1977) 632–642. https://doi.org/10.1002/aic.690230503.

[68] F.J. Gracia, L. Bollmann, E.E. Wolf, J.T. Miller, A.J. Kropf, In situ FTIR, EXAFS, and activity studies of the effect of crystallite size on silica-supported Pt oxidation catalysts, J. Catal. 220 (2003) 382–391. https://doi.org/10.1016/S0021-9517(03)00296-3.

[69] J.A. Anderson, Infrared study of the oxidation of carbon monoxide over Pt/Al2O3, J. Chem. Soc. Faraday Trans. 88 (1992) 1197–1201. https://doi.org/10.1039/FT9928801197.

[70] F. Gao, D.W. Goodman, Reaction Kinetics and Polarization Modulation Infrared Reflection Absorption Spectroscopy Investigations of CO Oxidation over Planar Pt-Group Model Catalysts, Langmuir. 26 (2010) 16540–16551. https://doi.org/10.1021/la1014626.

[71] J. Singh, M. Tromp, O.V. Safonova, P. Glatzel, J.A. van Bokhoven, In situ XAS with high-energy resolution: The changing structure of platinum during the oxidation of carbon monoxide, Catal. Today. 145 (2009) 300–306. https://doi.org/10.1016/j.cattod.2008.11.019.

[72] D.M. Nicholas, Y.T. Shah, Carbon Monoxide Oxidation over a Platinum-Porous Fiber Glass Supported Catalyst, Prod. RD. 15 (1976) 35–40. https://doi.org/10.1021/i360057a006.

[73] B. Subramaniam, A. Varma, Reaction kinetics on a commercial three-way catalyst: the carbon monoxide-nitrogen monoxide-oxygen-water system, Ind. Eng. Chem. Prod. Res. Dev. 24 (1985) 512–516.

[74] H. Beusch, P. Fieguth, E. Wicke, Thermisch und kinetisch verursachte Instabilitäten im Reaktionsverhalten einzelner Katalysatorkörner, Chem. Ing. Tech. 44 (1972) 445–451. https://doi.org/10.1002/cite.330440702.

[75] G. Ertl, P.R. Norton, J. Rüstig, Kinetic Oscillations in the Platinum-Catalyzed Oxidation of Co, Phys. Rev. Lett. 49 (1982) 177–180. https://doi.org/10.1103/PhysRevLett.49.177.

[76] M. Eiswirth, G. Ertl, Kinetic oscillations in the catalytic CO oxidation on a Pt(110) surface, Surf. Sci. 177 (1986) 90–100. https://doi.org/10.1016/0039-6028(86)90259-1.

[77] J. Kapicka, M. Marek, Oscillations on individual catalytic pellets in a packed bed: CO oxidation on Pt/Al2O3, J. Catal. 119:2 (1989). https://doi.org/10.1016/0021-9517(89)90178-4.

[78] R. Jensen, T. Andersen, A. Nierhoff, T. Pedersen, O. Hansen, S. Dahl, I. Chorkendorff, Self-sustained carbon monoxide oxidation oscillations on size-selected platinum nanoparticles at atmospheric pressure, Phys. Chem. Chem. Phys. 15 (2013) 2698–2702. https://doi.org/10.1039/C2CP43684A.

[79] J. Singh, M. Nachtegaal, E.M.C. Alayon, J. Stötzel, J.A. van Bokhoven, Dynamic Structure Changes of a Heterogeneous Catalyst within a Reactor: Oscillations

in CO Oxidation over a Supported Platinum Catalyst, ChemCatChem. 2 (2010) 653–657. https://doi.org/10.1002/cctc.201000061.

[80] V. Janardhanan, O. Deutschmann, Computational Fluid Dynamics of Catalytic Reactors, in: O. Deutschmann (Ed.), Model. Simul. Heterog. Catal. React. Mol. Process Tech. Syst., Wiley-VCH, 2011: pp. 251–282. https://doi.org/10.1002/9783527639878.ch8 (accessed August 27, 2019).

[81] L.A. Belfiore, Derivation of the Mass Transfer Equation, in: Transp. Phenom. Chem. React. Des., John Wiley & Sons, Ltd, 2003: pp. 253–263. https://doi.org/10.1002/0471471623.ch9.

[82] R.J. Kee, M.E. Coltrin, P. Glarborg, Molecular Transport, in: Chem. React. Flow, John Wiley & Sons, Inc., 2003: pp. 487–539. http://onlinelibrary.wiley.com/doi/10.1002/0471461296.ch12/summary (accessed September 14, 2016).

[83] N. Yao, Focused Ion Beam Systems: Basics and Applications, Reissue, Cambridge University Press, 2011.

[84] M. Linscheid, Mass Spectrometry, in: Handb. Anal. Tech., John Wiley & Sons, Ltd, 2001: pp. 579–626. https://doi.org/10.1002/9783527618323.ch20.

[85] Hiden Analytical Ldt., EPIC and IDP Analysers; Operator's Manual, (1998).

[86] J.H. Gross, Prinzipien der Ionisation und Ionendissoziation, in: J.H. Gross (Ed.), Massenspektrom. Ein Lehrb., Springer Berlin Heidelberg, Berlin, Heidelberg, 2013: pp. 23–74. https://doi.org/10.1007/978-3-8274-2981-0_2.

[87] C. Dass, Mass Analysis and Ion Detection, in: Fundam. Contemp. Mass Spectrom., John Wiley & Sons, Ltd, 2006: pp. 67–117. https://doi.org/10.1002/9780470118498.ch3.

[88] J.H. Gross, Massenspektrometer, in: J.H. Gross (Ed.), Massenspektrom. Ein Lehrb., Springer Berlin Heidelberg, Berlin, Heidelberg, 2013: pp. 129–244. https://doi.org/10.1007/978-3-8274-2981-0_4.

[89] J.E. Campana, Elementary theory of the quadrupole mass filter, Int. J. Mass Spectrom. Ion Phys. 33 (1980) 101–117. https://doi.org/10.1016/0020-7381(80)80042-8.

[90] C.V. Raman, K.S. Krishnan, A New Type of Secondary Radiation, Nature. 121 (1928) 501–502. https://doi.org/10.1038/121501c0.

[91] P.W. Atkins, J. de Paula, Atkins: Physikalische Chemie, 5., Wiley-VCH, Weinheim, 2013.

[92] G. Leyendecker, J. Doppelbauer, D. Bäuerle, P. Geittner, H. Lydtin, Raman diagnostics of CVD systems: Determination of local temperatures, Appl. Phys. A. 30 (1983) 237–243. https://doi.org/10.1007/BF00614773.

[93] G. Herzberg, Molecular Spectra and Molecular Structure -I. Spectra of Diatomic Molecules, D. Van Nostrand Company Inc., 1963. http://archive.org/details/molecularspectra032774mbp (accessed August 20, 2018).

[94] G. Herzberg, Molecular Spectra and Molecular Structure - II. Infrared and Raman Spectra of Polyatomic Molecules, D. Van Nostrand Company Inc., 1962. http://archive.org/details/in.ernet.dli.2015.84850 (accessed September 25, 2019).

[95] I.V. Hertel, C.-P. Schulz, Zweiatomige Moleküle, in: At. Molekü Opt. Phys. 2, Springer, Berlin, Heidelberg, 2010: pp. 1–88. https://doi.org/10.1007/978-3-642-11973-6_1.

[96] N.M. Laurendeau, Temperature measurements by light-scattering methods, Prog. Energy Combust. Sci. 14 (1988) 147–170. https://doi.org/10.1016/0360-1285(88)90002-0.

[97] Nabaltec AG, Technisches Datenblatt - Nabalox, (n.d.). https://nabaltec.de/fileadmin/user_upload/03_produkte/03-2_aluminiumoxid/nabaltec_tds_nabalox_neue-generation.pdf (accessed August 7, 2019).

[98] H.A.-G. El-Hofy, Fundamentals of Machining Processes: Conventional and Nonconventional Processes, Second Edition, CRC Press, 2013.

[99] M.J. Madou, Fundamentals of Microfabrication and Nanotechnology, Third Edition, Volume Two: Manufacturing Techniques for Microfabrication and Nanotechnology, 3rd edition, CRC Press, Boca Raton, FL, 2011.

[100] K. Jousten, ed., Wutz Handbuch Vakuumtechnik, 11th ed., Vieweg+Teubner Verlag, 2012. //www.springer.com/de/book/9783834817457 (accessed November 29, 2018).

[101] A.D. Pandey, R. Güttel, M. Leoni, F. Schüth, C. Weidenthaler, Influence of the Microstructure of Gold−Zirconia Yolk−Shell Catalysts on the CO Oxidation Activity, J. Phys. Chem. C. 114 (2010) 19386–19394. https://doi.org/10.1021/jp106436h.

[102] M. Hermans, J. Gottmann, F. Riedel, Selective, Laser-Induced Etching of Fused Silica at High Scan-Speeds Using KOH., J. Laser MicroNanoengineering. 9 (2014).

[103] N.J. Everall, Confocal Raman Microscopy: Performance, Pitfalls, and Best Practice: Invited Lecture at the Symposium “50 Years of SAS: Looking to the Future with Vibrational Spectroscopy” at Pittcon 2008, New Orleans, Louisiana, Appl. Spectrosc. 63 (2009) 245A-262A. https://doi.org/10.1366/000370209789379196.

[104] R. Tabaksblat, R.J. Meier, B.J. Kip, Confocal Raman Microspectroscopy: Theory and Application to Thin Polymer Samples, Appl. Spectrosc. 46 (1992) 60–68. https://doi.org/10.1366/0003702924444434.

[105] M.C. Drake, G.M. Rosenblatt, Rotational Raman scattering from premixed and diffusion flames, Combust. Flame. 33 (1978) 179–196. https://doi.org/10.1016/0010-2180(78)90059-7.

[106] I.B. Gornushkin, P.E. Eagan, A.B. Novikov, B.W. Smith, J.D. Winefordner, Automatic Correction of Continuum Background in Laser-Induced Breakdown and Raman Spectrometry, Appl. Spectrosc. 57 (2003) 197–207. https://doi.org/10.1366/000370203321535123.

[107] B. Sosna, O. Korup, R. Horn, Probing local diffusion and reaction in a porous catalyst pellet, J. Catal. 381 (2020) 285–294. https://doi.org/10.1016/j.jcat.2019.11.005.
[108] P. Linstrom, NIST Chemistry WebBook, NIST Standard Reference Database 69, (1997). https://doi.org/10.18434/T4D303.
[109] M. Hettel, C. Antinori, O. Deutschmann, CFD Evaluation of In Situ Probe Techniques for Catalytic Honeycomb Monoliths, Emiss. Control Sci. Technol. 2 (2016) 188–203. https://doi.org/10.1007/s40825-016-0043-1.
[110] J. Singh, E.M.C. Alayon, M. Tromp, O.V. Safonova, P. Glatzel, M. Nachtegaal, R. Frahm, J.A. van Bokhoven, Generating Highly Active Partially Oxidized Platinum during Oxidation of Carbon Monoxide over Pt/Al2O3: In Situ, Time-Resolved, and High-Energy-Resolution X-Ray Absorption Spectroscopy, Angew. Chem. Int. Ed. 47 (2008) 9260–9264. https://doi.org/10.1002/anie.200803427.
[111] A. Jess, P. Wasserscheid, Chemical Technology: An Integral Textbook, 1., Wiley-VCH, Weinheim, 2013.
[112] P.H. Oosthuizen, V. Mansingh, Free and Forced Convection Heat Transfer from Short Inclined Circular Cylinders, Chem. Eng. Commun. 42 (1986) 333–348. https://doi.org/10.1080/00986448608911749.
[113] L. Vornehm, Einfluss der Anströmrichtung auf den Wärmeübergang, Z VDI. 80 (1936) 702–703.
[114] V. Gnielinski, G6 Querumströmte einzelne Rohre, Drähte und Profilzylinder, in: VDI-Wärmeatlas, Springer Berlin Heidelberg, Berlin, Heidelberg, 2013: pp. 817–818. https://doi.org/10.1007/978-3-642-19981-3_47.
[115] H.D. Baehr, Convective heat and mass transfer. Single phase flow, in: Heat Mass Transf., Springer Berlin Heidelberg, 2006: pp. 253–403. http://link.springer.com/chapter/10.1007/3-540-29527-5_3 (accessed April 26, 2015).
[116] F.S. Mirhashemi, S.H. Hashemabadi, S. Noroozi, CFD simulation and experimental validation for wall effects on heat transfer of finite cylindrical catalyst, Int. Commun. Heat Mass Transf. 38 (2011) 1148–1155. https://doi.org/10.1016/j.icheatmasstransfer.2011.05.001.
[117] W. Keil, E. Wicke, Über die kinetischen Instabilitäten bei der CO-Oxidation an Platin-Katalysatoren, Berichte Bunsenges. Für Phys. Chem. 84 (1980) 377–383. https://doi.org/10.1002/bbpc.19800840417.
[118] P.T. Fanson, W.N. Delgass, J. Lauterbach, Island Formation during Kinetic Rate Oscillations in the Oxidation of CO over Pt/SiO2: A Transient Fourier Transform Infrared Spectrometry Study, J. Catal. 204 (2001) 35–52. https://doi.org/10.1006/jcat.2001.3369.
[119] H. Yoshida, K. Matsuura, Y. Kuwauchi, H. Kohno, S. Shimada, M. Haruta, S. Takeda, Temperature-Dependent Change in Shape of Platinum Nanoparticles Supported on CeO2 during Catalytic Reactions, Appl. Phys. Express. 4 (2011) 065001. https://doi.org/10.1143/APEX.4.065001.

[120] E.K. Dann, E.K. Gibson, C.R.A. Catlow, V. Celorrio, P. Collier, T. Eralp, M. Amboage, C. Hardacre, C. Stere, A. Kroner, A. Raj, S. Rogers, A. Goguet, P.P. Wells, Combined spatially resolved operando spectroscopy: New insights into kinetic oscillations of CO oxidation on Pd/γ-Al2O3, J. Catal. 373 (2019) 201–208. https://doi.org/10.1016/j.jcat.2019.03.037.

[121] G. Mestl, In situ Raman spectroscopy — a valuable tool to understand operating catalysts, J. Mol. Catal. Chem. 158 (2000) 45–65. https://doi.org/10.1016/S1381-1169(00)00042-X.

[122] DIN EN 60584-3:2008-08, Thermopaare_- Teil_3: Thermoleitungen und Ausgleichsleitungen_- Grenzabweichungen und Kennzeichnungssystem (IEC_60584-3:2007); Deutsche Fassung EN_60584-3:2008, Beuth Verlag GmbH, n.d. https://doi.org/10.31030/1444153.

[123] H. Schwarz, Gas-Phase Methane Oxidation Investigated by Laser-Induced Fluorescence, Species Profile Measurements and Kinetic Reactor Simulations, PhD Thesis, Technischen Universität Berlin, 2013.

[124] W.G. Breiland, P. Ho, In situ laser measurements of silicon CVD, in: Proc. Ninth Int. Conf. Chem. Vap. Depos., The Electrochemical Society, Pennington, 1984: pp. 44–59.

[125] Catalysts | Haldor Topsoe, (n.d.). https://www.topsoe.com/products/catalysts (accessed October 9, 2019).

List of figures

List of tables